Ludwig Maximilians Universität München

Faculty of Physics

Wake Identification and Characterization of a Full Scale Wind Energy Converter in Complex Terrain with Scanning Doppler Wind Lidar Systems

---

Identifikation und Charakterisierung des Nachlaufs einer Windenergieanlage im komplexen Gelände mit scannenden Doppler Wind Lidar Systemen

December 11, 2017

Author: Stephan Kigle

Master of Science

Professor: Prof. Dr. Bernhard Mayer
Supervisor: Dr. Norman Wildmann

Abstract

As the resource wind is increasingly exploited to produce electricity, wind energy converter (WEC) deployment expands to more complex terrain such as hilltops or mountain ridges. In that context it is crucial to understand the interaction between the atmospheric boundary layer (ABL) flow and the WEC in order to predict downstream flow characteristics. In the context of the Perdigão 2017 experiment, the German Aerospace Center performed full-scale wake measurements on a single WEC of type Enercon E82 with three Leosphere Windcube 200S long-range scanning Lidar systems.
The experimental setup covers two parallel ridges 1.4 km apart, separated by a 200 m deep valley. The ridges are oriented in NW-SE direction, perpendicular to the main wind direction, which is SW. Two of the three scanning Lidar systems are positioned downstream of the WEC in line with the main wind direction to span a vertical plane, perpendicular to the ridges, with range-height indicator (RHI) scans. This allows to investigate wake events with single or dual-doppler Lidar techniques. The third Lidar system, which is positioned along the WEC ridge, is used to measure the wake position outside the above mentioned measurement plane.
Wake events in three different ABL regimes (neutral, stable and convective) are evaluated with respect to wake position, dispersion, propagation and the wind-speed deficit. It is found that wake position and propagation are strongly influenced by the atmospheric stability, forcing the wake to deviate from hub height, migrating to higher levels for convective regimes. For stable ABL conditions the wake descends into the valley and is clearly detectable up to at least nine rotor diameters downstream of the WEC, in some cases. Furthermore, the coplanar scanning strategy allows to calculate the two-dimensional wind vector in the vertical scanning plane, indicating that vertical wind components with up to $2\,\mathrm{ms}^{-1}$ play an important role in the interaction between ABL flow and WEC. With the help of the third Lidar system on the WEC ridge, wake meandering can be quantified. This work will provide a thorough analysis of three exemplary measurement days.

Contents

List of Abbreviations

ABL Atmospheric Boundary Layer 7
CBL Convective Boundary Layer 7
CFD Computational Fluid Dynamic 19
CNR Carrier to Noise Ratio 37
CS Coplanar Scan 31
CT Complex Trajectory 23
DBS Doppler-Beam-Swing 13
DIAL Differential-Absorption Lidar 20
DLR German Aerospace Center 5
DNS Direct Numerical Simulation 19
DTU Technical University of Denmark 24
EAWA European Agency of Wind Energy 5
EOL Earth Observing Laboratory 48
EULAG Eulerian/semi-LAgrangian Geophysical 28
FA Free Atmosphere 7
FFT Fast-Fourier Transformation 25
FWHM Full Width Half Maximum 23
IEA International Energy Agency 1
ISFS Integrated Surface Flux System 46
LES Large Eddie Simulation 19
Lidar LIght Detection And Ranging 14
LL Locking Loop 22
LLJ Low Level Jet 53
LO Local Oscillator 22
LOS Line Of Sight 23
MLE Maximum Likelihood Estimate 25

List of Figures

List of Tables

Chapter 1

Introduction

1.1 The Energy Problem

Since the beginning of the Industrial Revolution, in the year 1760, mankind steadily refined production and exploitation of energy from natural resources. Had it mainly been the exploitation of somatic and animal energy before this turning point in history, the invention of the steam engine with its possibility to convert chemical energy into usable forms of energy, accelerated industrial growth, mobility and the use of private energy applications. Today, humans are enjoying an unseen level of prosperity and mobility based on and upheld by an energy industry running on fossil fuels.

In 2015, according to the International Energy Agency (IEA), the world primary energy supply totaled 13 647 Mtoe. Fossil fuels, in decreasing order oil, coal and natural gas, accounted for 81.4 % of the total share. In second position, contributing with a share of 9.7 %, were biofueles and waste, followed by nuclear energy (4.9 %) and hydro energy (2.5 %). Energy from renewable sources, like wind, solar thermal, photovoltaic and geothermal energy, only accounted for as little as 1.5 % of global primary energy supply (IEA, 2017a).

This dependence on energy supply and therefore energy production on fossil fuels was of no big concern, as oil, gas and coal were plentifully available during the last decades, guaranteeing a cheap and shear inexhaustible amount of available energy. But the golden ages are already long gone.

In these days society experiences the uncertainty of possible energy shortages in the near future, as known fossil fuel reserves are rapidly used up. The term 'peak oil', as the point in time where there will be a steady decrease in oil production, due to the shortage of new production possibilities, is already well-established in the

science community and the exact date when it will occur is heavily debated (Santos, 2011). Not only is the exhaustion of fossil fuels a threat to energy security in the years to come, but it is also a threat to the climate, as carbon emissions, together with the emission of other greenhouse gases, are greatly contributing to man-made climate change (Pachauri et al., 2014). First indications of global warming, due to carbon emissions, were already discussed in 1896 by Svante Arrhenius in his article: *'On the Influence of Carbonic Acid in the Air upon the Temperature of the Ground'* (Arrhenius, 1896).
The awareness for problems caused by carbon emissions and a fossil fuel based energy system has been growing during the last years and political action is undertaken to counteract the trend of global warming. The Paris Agreement, signed in December 2015, strives to keep the level of global warming well below 2 °C until the end of this century and, if possible, limit it to 1.5 °C. Therefore, a list of measures was passed, including the reduction of carbon emissions by fossil fuels and a change of the energy system towards renewable energy sources, finally leading to a carbon neutral world during the second half of this century (UNFCCC, 2016). In order to achieve these goals, big investments into the sector of renewable energies will be needed.
Wind energy as the fourth biggest renewable energy source in 2015, after biomass and waste, hydro and geothermal energy (IEA, 2017b), will play an increasingly important role in the near future to sustain this process.

1.2 Wind Energy - a Solution?

1.2.1 Global Wind Energy

To grasp the importance of wind energy when changing the energy supply from fossil fuels to renewable energy sources, the theoretical energy potential available for wind energy production has to be considered in a first step. In Fig. 1.1 the 2006 averaged annual wind power potential for onshore wind energy production as estimated by Lu et al. (2009) can be seen. A unique distribution of available wind potential can be identified, as the resource wind is not homogeneously distributed over the earth's surface. Especially the mid-latitude, continental areas to the south and the north of the equator are well suited to harvest wind energy.
When excluding water covered, forested and urban areas, as well as constantly snow or ice covered regions and additionally assuming that a world wide turbine array, consisting of 2.5 MW turbines, would only operate at 20 % of their rated capacity,

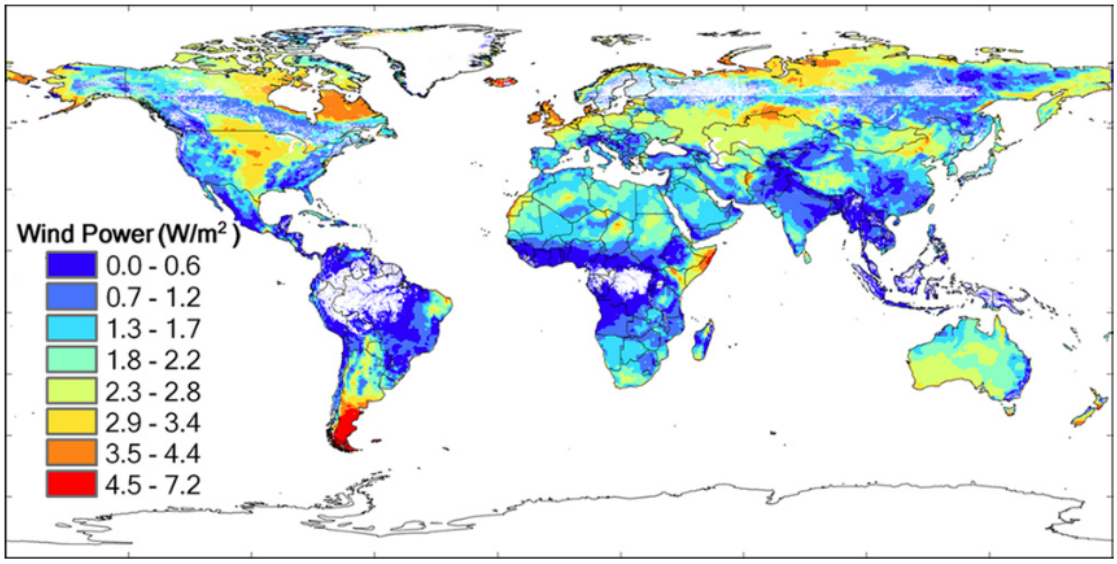

Figure 1.1 – *2006 annual average prospective onshore wind power, in* Wm^{-2}*, as presented in Lu et al. (2009). Spacial restrictions on the implementation to harvest wind resources are taken into consideration discounting limitations on possible capacity factors.*

Lu et al. (2009) estimates that the electricity production from the available wind potential could exceed the 2008 global electricity demand by more than 40 times. These numbers would be even higher when taking offshore potential into account, too. Nevertheless, only a small fraction of the available potential is used to date. In 2015 only 3.4 % of the worlds total domestic electricity generation had wind as their source.

However small this fraction might seem, the installation of facilities to produce and the production of electricity form wind energy is steadily growing throughout the last years. In 2005 only 104 TWh of electricity were produced, when in 2015 this number had already grown to 838 TWh, with an installed capacity of 414 GW(IEA, 2017a).

The IEA predicts that electricity production from onshore wind energy will nearly double in the period 2015 until 2020. This means that wind energy expansion is on track to produce the necessary 2400 TWh of electricity in 2025 to meet the 2 °C target. Offshore wind energy production, on the contrary, will need further investments to keep up with the goal to produce 225 TWh of electricity in 2025 (IEA, 2017c).

The positive development during the last years and in the years to come, is a clear indication that wind energy will play an increasingly important role in order to secure the world's energy supply. Technical improvements, bigger turbines, and

expansion to more complex terrain, as well as better life time analyses to increase cost efficiency are key for further exploitation of the resource wind.

1.2.2 Wind Energy in Germany

Germany as one of the signing members of the Paris Agreement is willing to contribute to reduce worldwide greenhouse gas emissions. Therefore, the Federal Ministry for the Environment, Nature and Conservation, Building and Nuclear Safety forwarded a Climate Protection Plan 2050 with the goal to reduce 80 % to 95 % of greenhouse gas emissions until 2050, in comparison to emission levels in 1990 (BMUB, 2016).
One major sector that needs to be renewed according to the Climate Protection Plan 2050 is the energy producing sector, where a shift towards a de-carbonized industry needs to be implemented.
In 2016, renewable energies already contributed 31.7 % to the total German electricity consumption. The major share came from wind energy (13.3 %) with a total production of 78.6 TWh of electricity. This amount of energy is produced by an installed capacity of 49 545 MW (BMWi, 2017).
During the last years the wind energy sector in Germany is steadily growing, not only onshore but also offshore. This trend is likely to be continued in the future to further contribute to a transition towards a carbon-free energy production in Germany. The potential of installed capacity for further energy production from wind energy, onshore only, is estimated to be as high as 189 GW producing 390 TWh of electricity (Bofinger et al., 2011), which accounts 65 % of German electricity in 2010.
However, wind energy development is still undergoing further technical improvements, not only in turbine design and hight, but also in wind park layout and rotor materials. Some of the problems and challenges wind energy is still facing will be explained in the following chapter.

1.3 Wind Energy and its Challenges

The challenges wind energy is confronted with range from societal over economic to technical aspects. Aesthetic as well as environmental concerns often reduce public acceptance as well as the political will to install wind parks (Bruns and Ohlhorst, 2011). The intermittency of electricity production causes additional problems in net integration and energy storage. And even though wind energy has been around

for quite some time already and has matured over the last decades, there is still some possibility to increase efficiency of Wind Energy Converters (WECs) and wind parks. Turbine efficiency, to convert kinetic wind energy into electricity, is usually around 40 %, which is about 20 % less than the theoretical limit described by Betz (Guerrero-Lemus and Martínez-Duart, 2012).
The European Agency of Wind Energy (EAWA) has worked out the challenges that wind energy will have to overcome in the future and van Kuik et al. (2016) summarized them in 11 topics. Among these one finds two topics that are of special interest to the research goals of this thesis: *'wind and turbulence'* and *'reliability and uncertainty modeling'*.
As the atmospheric flow can mathematically be considered a fluid dynamics problem, it is necessary to describe the chaotic motion of the turbulent flow when trying to model its structure. Even smallest deviations between model and reality can lead to heavy impacts on the model solution, as errors grow exponentially over time. Predictions of incoming turbulent wind fields therefore heavily rely on a coupling between observations and predictions. Even though computational possibilities are rapidly advancing, deeper understanding of the underlying turbulent structures and chaotic motion is necessary to better predict turbine operating conditions, including mechanical loads and electricity production.
Further complications are generated by the fact that turbines are increasingly built in complex terrain and offshore. However, it is not yet clear how to model and parametrize inflow conditions and wake effects in these regions (van Kuik et al. (2016)).
The Perdigão 2017 experiment, during which the atmospheric flow over two parallel mountain ridges was observed by a multitude of measurement instruments, is supposed to contribute to solutions and offer deeper insight into some of the challenges stated above. The observational data acquired in this exceptional experiment will be used to validate computational models and further investigate turbulent wind flow patterns in complex terrain. The German Aerospace Center (DLR) took part in this unique effort and focuses on the investigation of the wake, produced by a single WEC situated in complex terrain. With this investigation the DLR will contribute to a better understanding of wake characteristics.
Taking topography and meteorological conditions into account will ultimately lead to improvements in wind farm design, the validation of computational models and will improve the physical knowledge of wake creation and propagation in different atmospheric conditions.

1.4 Outline

The goal of this thesis is to contribute to overcome some of the challenges wind energy is facing. For this purpose, it provides a complete overview over: the physical and atmospheric aspects important to wind energy and basic operating principles of a WEC (Chapt. 2); the measuring devices to remotely observe turbulent wind structures (Chapt. 3); the preparation and realization of the measurement campaign in Perdigão, Portugal (Chapt. 4 and Chapt. 5); the wake detection methodology (Chapt. 7); the wake characteristics of a single WEC in complex terrain (Chapt. 8) and the sources of error and their influence on the measurements (Chapt. 9). The results will then, ultimately, be summarized in Chapt. 10.

Chapter 2

Theory

2.1 Wind as Part of the Atmosphere

2.1.1 The Atmospheric Boundary Layer

The earth's atmosphere can be divided in various layers with distinct properties, one of them being the troposphere, reaching from ground level to a height of about 11 km. Its contact zone with the earth's surface is called the Atmospheric Boundary Layer (ABL). Or to be more precise, the ABL can be defined *'as that part of the troposphere that is directly influenced by the presence of the earth's surface, and responds to surface forcing with a timescale of about an hour or less'* (Stull, 2012). The ABL serves the connection between the earth's surface and the overlaying Free Atmosphere (FA) and transfers alterations induced by changes of surface properties into the FA. Forcings on the ABL include heat fluxes, drag forces as well as terrain specific alterations. Consequently, its extension can vary from a couple of hundreds of meters to several kilometers depending on the surface conditions. The ABL, in comparison to the FA, exhibits less momentum but higher degrees of turbulence and additionally differs in other atmospheric variables such as heat, moisture, aerosols and pollutant content. Depending on the generation of turbulent kinetic energy by either friction or heat, Stull (2012) distinguishes between three different types of ABLs:

- a Neutral Boundary Layer (NBL),
- a Convective Boundary Layer (CBL),
- a Stable Boundary Layer (SBL).

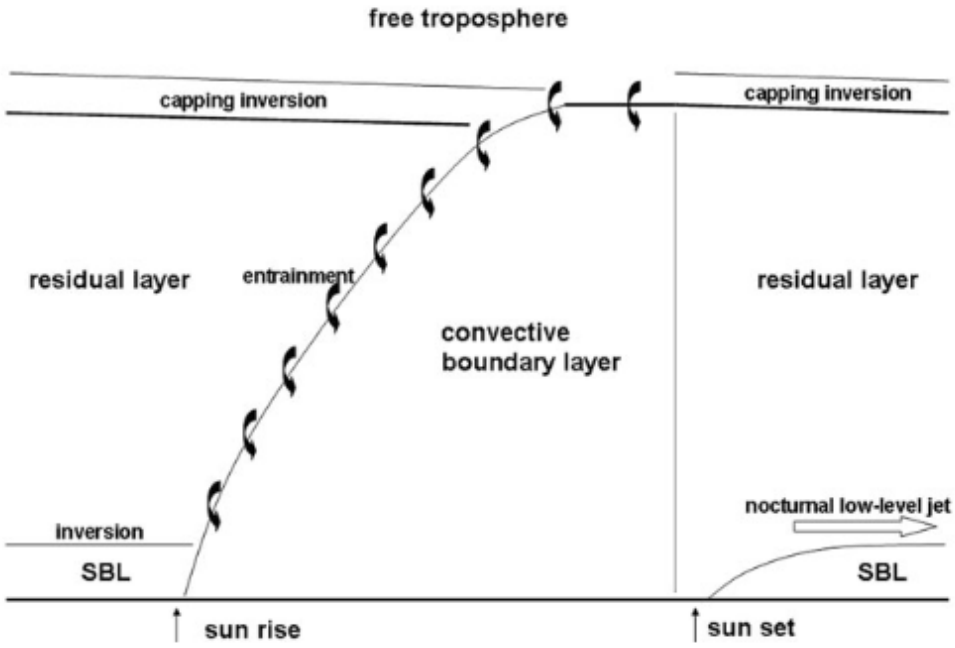

Figure 2.1 – *Diurnal cycle of the ABL as in Emeis (2010).*

In a NBL the generation of turbulent kinetic energy is dominated by shear processes at the surface and the heat flux between the ABL and the earth's surface is almost inexistent. On the other hand, a CBL is dominated by the generation of turbulent kinetic energy due to the heat flux into the atmosphere. A CBL forms when the ABL is heated from beneath. And, as a last case, a SBL forms when heat is withdrawn from the ABL, so to say cooled from beneath. Due to the strong dependence of the earth's surface heat budget on the incident solar radiation in continental mid latitude locations, the forcing exerted onto the ABL undergoes a diurnal cycle that can be seen in Fig. 2.1.
During daytime, the incident solar radiation is absorbed by the ground, which increases the heat budget. This leads to the heating of near ground air masses that will rise due to their lower density in comparison to cold air masses. Turbulent kinetic energy is therefore added to the ABL and a well mixed or CBL is formed. Once solar radiation decreases during the evening, the heat budget of the surface diminishes and the heat flux reverses. Cooling of the lower air masses kicks in and a stable stratification evolves. On top of the SBL at night time, a Residual Layer (RL) is left. This RL is a zone containing well mixed air masses, that are isolated from the surface by the SBL and exhibit properties of a well mixed ABL during day-time. The stratification of the SBL suppresses turbulence generation as vertical motion and shear forces are reduced, leading to a calmer air flow during

night times. However, a phenomena called nocturnal jet can form at the boundary between SBL and RL with wind velocities greater than the geostrophic mean wind speed.
According to Emeis (2010), the equations of motion in the NBL read as follows:

$$\frac{1}{\rho}\frac{\partial p}{\partial x} + fv + \frac{\partial}{\partial z}(K_z\frac{\partial u}{\partial z}) = 0; \tag{2.1}$$

$$\frac{1}{\rho}\frac{\partial p}{\partial y} - fu + \frac{\partial}{\partial z}(K_z\frac{\partial v}{\partial z}) = 0; \tag{2.2}$$

where ρ is the density of the air mass, p is the atmospheric pressure, f is the Coriolis parameter and K_z is the turbulent vertical mixing coefficient. u and v are the horizontal velocities in easterly and northerly direction, respectively. It can be seen that the forces from large scale pressure gradients are in equilibrium with the Coriolis forces and the dissipative frictional forces.
Depending on the influence of each of the three terms in Eq.2.1 and 2.2 one can divide the flow in the NBL into two areas: the Prandtl Layer and the Ekman Layer. The Prandtl Layer describes the part of the ABL where the influence of the Coriolis force is negligible and turbulent vertical fluxes of humidity, heat and momentum do not vary by more than 10 % from the values at ground level (Emeis, 2010). For a constant vertical momentum flux and a mean flow in easterly direction, the equations of motion (Eq. 2.1 and 2.2) simplify to:

$$K_z\frac{\partial u}{\partial z} = const = u_*^2. \tag{2.3}$$

Solving Eq. 2.3 leads to the well known logarithmic velocity profile as a function of z and the roughness length z_0, reading

$$u(z) = \frac{u_*}{\kappa}ln(\frac{z}{z_0}). \tag{2.4}$$

$K_z = lu_*$, where $l = \kappa z$ is the mixing length ($\kappa = 0.4$ is the van Kármán constant) and u_* represents the friction velocity.
Subsequent to the Prandtl layer follows the so called Ekman layer. Considering that the vertical mixing coefficient K_z will not increase with heights above the Prandtl layer anymore, Eq. 2.1 and 2.2 can be solved to:

$$u(z) = u_g[1 - e^{-\gamma z}cos(\gamma z)]; \tag{2.5}$$

$$v(z) = u_g e^{-\gamma z}sin(\gamma z); \tag{2.6}$$

with $\gamma = \sqrt{f/(2K_z)}$ and u_g being the geostrophic wind speed in easterly direction. Equations 2.5 and 2.6 describe a change in wind direction with a change of height, the so called Ekman spiral.
The transition between the Prandtl and the Ekman layer is smooth and needs to be taken into account when describing the whole motion in the ABL.
The vertical structure derived for the NBL, can also be found in the SBL and the CBL. For these cases, however, the vertical velocity profile needs to be corrected by a correction function as proposed by Paulson (1970) and Högström (1988) to account for motions induced by the increasing or decreasing heat budget.
The simple velocity profile described above represents the NBL over flat terrain. When taking a look at the ABL over more complex terrain, such as hills or mountains, further considerations need to be taken into account.
Hills and mountains present inhomogeneities to the flow, inducing large distortions into the ABL. Local thermal activities add to the complexity of ABL flow in these regions, as slope winds, valley and mountain winds as well as larger wind systems affecting the surroundings can evolve.
The most elusive of these phenomena are the slope winds, as they can change within minutes as a reaction to changes in the heat flux from the mountain slopes. The spacial extension of these flows heavily depends on the thermal forcing and can vary from meters to kilometers contributing to a circular flow across the valley transect. During daytime, when incident solar radiation onto the slope reaches a maximum, upward winds are dominant, whereas downward winds prevail during night times.
Valley or mountain winds and the winds blowing over the surrounding planes are of a larger spacial scale than the slope winds. These wind systems develop due to differences in the thermal heating efficiency caused by either the spacial extension of the heated area in case of the valley and mountain winds or the height difference in case of the plain winds. For further details please refer to Emeis (2010).

2.1.2 Turbulence

When speaking about ABL flow, generally known as wind, it is often not accounted for the fact that wind can be divided into three main components that together make up a complex air flow. The flow in general is composed of mean wind, waves and turbulence. The temporal as well as the spacial properties of each component differ from the others. Horizontal fluxes of atmospheric properties are mainly dominated by the mean wind, i.e. advection, whereas fluxes in vertical direction are

governed by the turbulent motion of air. The relatively high amount of turbulence that can be found in the ABL, caused by the interaction between the air masses and the surface, is a distinct feature that separates the ABL from other parts of the atmosphere, as turbulence decays with increasing heights. Waves differ in their transportation abilities in comparison to the two previously mentioned components, as they are mainly transporting energy and momentum and only inefficiently transport other atmospheric properties, such as humidity or pollutants, for example.

The ABL flow as a superposition of the different motions of air allows us to distinguish between properties correlated to each of the phenomena. The ABL flow can therefore be split into a mean and a turbulent part.

One can picture turbulent motion as the overlap of so called eddies, which can be considered irregular whirls of motion. The spacial extension of these eddies can reach from the heights of the ABL to very small structures, in the range of a few millimeters. The diversity of energy and size carried by the eddies can be characterized by the turbulent spectrum of the atmosphere. Large eddies that develop as a direct consequence of convection or frictional forcing are the most energetic ones and then decay into smaller eddies carrying less energy, until they finally dissipate due to the effects of molecular viscosity.

For the adjustment of the atmosphere to external forcing, such as radiative heating, for example, the turbulent motion is the most effective process. In comparison to the molecular diffusivity, which is another process that allows the atmosphere to respond to external forcing, turbulent motion is several orders of magnitude more efficient.

As the mean flow is distorted by topography and obstacles in the flow passage, turbulent flow effects can evolve. Objects located in the flow bring eddies into existence that decay with distance in downstream direction. A turbulent wake evolves (Tampieri, 2017). This phenomenon will be discussed in more detail in Chapt. 2.2.

In oder to measure the atmosphere's turbulent structures, one would need to resolve atmospheric parameters at several points in space at one certain point in time. However, it is very costly and often impossible to measure the whole atmosphere instantaneously at different spatially separated locations. To still be able to analyze the turbulent motion, one is often limited to a single measurement point, sampled over a long period of time. From these long term measurements it is possible to derive the eddies and their properties under certain circumstances.

The hypothesis of frozen turbulence, as suggested by Taylor (1938), can be used, when it is supposed that eddies only change their properties slightly while passing the measurement sensor. This frozen eddy hypothesis is therefore only valid if the turbulence intensity is small in comparison to mean wind direction. Then, the spacial magnitude of the passing eddy can be reproduced by taking the main wind direction and the time needed for the passage into account (Stull, 2012).
For observations that are time averaged, one has to consider that turbulent structures of time scales smaller than the averaging time cannot be resolved. This means that for a given phenomenon to be observed the sampling frequency needs to be sufficiently small. On the other hand, averaging allows to erase fluctuations on time scales irrelevant to the observation, which can help to identify persisting flow features.
Similar considerations can be taken into account for spatial resolution, when measuring turbulent flow. The spatial resolution needs to be sufficiently small to resolve the phenomena that is being investigated.

2.1.3 Wind Measurement Methods

Figure 2.2 – *Meteorological mast with two sonic anemometers deployed during the Perdigão 2017 experiment.*

To measure wind speed and direction in the ABL, one can distinguish between two main branches of measurement techniques - in-situ and remote-sensing.
In-situ measurements are point measurements at a certain location and therefore

limited in their ability to resolve the wind properties over large areas or height ranges. A variety of instruments can be used to do in-situ measurements with anemometers being the most common type to measure the wind speed.
The layout of anemometers differ widely in sophistication, ranging from simple mechanical anemometers, like cup or propeller anemometers that transform the kinetic wind energy into rotational motion, to laser anemometers. Sonic anemometers use a sound signal that is transmitted between an emitter and a receiver. The difference in travel time along the measuring path in both directions depends on the wind speed. Different geometric arrangements of multiple emitter and receiver pairs then allow to calculate the three-dimensional wind vector, as well as wind direction and the absolute wind velocity.
To be able to monitor wind speeds at different locations and heights in a certain measurement area, anemometers are normally mounted on meteorological masts in combination with further instruments to assess, for example, temperature, humidity or radiation.
Another method to measure wind speeds in the ABL, is to measure the wind speed with pressure or hot wire probes. These probes can be lifted into the atmosphere by a Tethered Lifting System (TLS), for example, to measure height profiles of the wind velocity. The TLS additionally offers the advantage to measure longer time intervals at certain heights of interest, without being permanently restricted to one height, as are the sonic anemometers.
To overcome the spacial limitations of in-situ measurements, remote-sensing instruments play a crucial role in mapping the wind speed and direction over larger areas. These instruments use different measurement principles, most of them being of an active type, which means that they radiate either electromagnetic or acoustic waves into the atmosphere to then analyze the backscattered signal.
SOund Detection and Ranging (SODAR) systems emit acoustic waves into the atmosphere that are backscattered on disruptions of the refraction index of the atmosphere, which are caused by density fluctuations that ultimately originate in temperature differences. The fluctuations are traveling with mean wind speed and therefore vertical wind profiles can be retrieved with the Doppler-Beam-Swing (DBS) method. More sophisticated Radio-Acoustic Sounding Systems (RASS) are emitting acoustic waves and electromagnetic waves at the same time, which also allows to measure temperature.
Emitting electromagnetic waves only, are RAdio Detection And Ranging (Radar) systems. The waves of rather large wave lengths are backscattered at humidity

fluctuations throughout the atmosphere. With the DBS method a vertical profile of the three-dimensional wind vector can be calculated. However, Radar wind-profilers are limited in their ability to resolve the ABL as the first measurement point normally is at a height of about one km, which is, in most cases, higher than the top of the ABL.
Another remote-sensing instrument that uses the emission of electromagnetic waves to measure the wind speed, is the Doppler Wind LIght Detection And Ranging (Lidar) system. These systems operate on wave length in the micrometer scope. Lidar systems can be divided into profiling Lidar systems, only relaying on the DBS or Velocity Azimuth Display (VAD) technique, and scanning Lidar systems. Scanning Lidar systems posses the ability to direct their laser beam over a wide range of azimuth and elevation angles, enabling them to measure the radial velocity in a specific direction (Emeis, 2010). The scanning Doppler Wind Lidar system will be described in more detail in Chapt. 3, as this type of measurement system was used during the measurement campaign described in Chapt. 5.

2.2 The WEC Wake

The interaction between a WEC and the atmospheric flow has been studied extensively during the last decades. However, wind turbine layout and aerodynamics are quite complicated and a detailed illustration covering all aspects is beyond the scope of this thesis. The following chapters will, accordingly, only outline the most basic principles of the power extraction and associated wake generation.

2.2.1 Wind - Turbine Interaction

In Chapt. 2.1.1 the equations of motion for an ABL flow were already introduced and the vertical velocity profile derived. Now, to describe the interaction between the atmospheric flow and a WEC, these considerations will be built upon.
A WEC represents an object in the flow path, distorting the flow and hence causing fluid properties to change in downstream direction. These flow variations are referred to as a wake.
While passing the wind turbine, kinetic energy is extracted from the flow and converted into rotational energy, which then can be used to generate electricity, using a generator. This extraction of kinetic energy leads to a change of momentum carried by the flow, meaning that the downwind wind speed is smaller than upstream. In the following, a theoretical estimate on how much power a WEC can extract from

the atmospheric flow, similar to the one presented by Molly (1978), is given.

The kinetic energy E_{kin} for any mass m with velocity $\mathbf{v}$ is defined as

$$E_{\text{kin}} = \frac{1}{2} m \mathbf{v}^2. \tag{2.7}$$

It follows that the power P contained in an air mass in constant motion equals

$$P = \frac{\partial E_{\text{kin}}}{\partial t} = \frac{1}{2} \dot{m} \mathbf{v}^2. \tag{2.8}$$

The air mass $\dot{m}$ that is transported through a given cross section during a certain time interval can be expressed as

$$\dot{m} = \frac{\partial m}{\partial t} = \frac{\partial (\rho V)}{\partial t} = \rho A \frac{\partial x}{\partial t} = \rho A \mathbf{v}, \tag{2.9}$$

with $\rho = 1.2041\,\text{kgm}^{-3}$ being the air density and A the area of the cross section. $\mathbf{v}$ designates the wind velocity.
While passing the WEC, mass must be conserved, as one considers the air to be an incompressible fluid. The mass conservation equation reads:

$$\dot{m}_\infty = \rho A_\infty \mathbf{v}_\infty = \rho A_{\text{wake}} \mathbf{v}_{\text{wake}} = \dot{m}_{\text{wake}}, \tag{2.10}$$

the index '∞' denoting the air flow properties upstream the WEC, whereas the index 'wake' denotes the air flow properties downstream the WEC.
It is now possible to calculate the power P_{ex} that can be extracted from the flow by subtracting the downstream power P_{wake} from the upstream power P_∞ using Eq. 2.10:

$$P_{\text{ex}} = P_\infty - P_{\text{wake}} = \frac{1}{2} \dot{m} (\mathbf{v}_\infty^2 - \mathbf{v}_{\text{wake}}^2), \tag{2.11}$$
$$\text{with} \quad \dot{m} = \rho A_\infty \mathbf{v}_\infty.$$

Mathematically, Eq. 2.11 would lead to the result that maximum power could be extracted when v_{wake} equals zero. Practically, this would lead to a stop of the air flow through the rotor plane when considering Eq. 2.10.
To resolve this discrepancy, it is necessary to take a closer look at the physical forces acting on the wind turbine. The force exerted onto the WEC by the bypassing air per time unit is

$$F = \dot{m} (\mathbf{v}_\infty - \mathbf{v}_{\text{wake}}), \tag{2.12}$$

according to the conservation of momentum.
The WEC, in order to compensate this force, has to work against the air flow with the power

$$P_{\text{mec}} = \dot{m}(\mathbf{v}_\infty - \mathbf{v}_{\text{wake}})\mathbf{v}_t, \tag{2.13}$$

where $\mathbf{v}_t$ denotes the wind velocity in the rotor plane.
Equalizing Eq. 2.13 and 2.11 yields $\mathbf{v}_t = 1/2 \cdot (\mathbf{v}_\infty + \mathbf{v}_{\text{wake}})$, which is exactly the mean of the wind speed upstream and downstream the WEC.
We can now calculate the power that can be extracted from the air flow by substituting the mass flow in Eq. 2.11 with the mass flow m_t at the turbine cross section, which is $\dot{m}_t = \rho A_t \mathbf{v}_t$:

$$P_{\text{ex}} = \frac{1}{4}\rho A_t(\mathbf{v}_\infty^2 - \mathbf{v}_{\text{wake}}^2)(\mathbf{v}_\infty + \mathbf{v}_{\text{wake}}). \tag{2.14}$$

The fraction of power that can be extracted from the undisturbed air flow can now be defined as the power coefficient c_p, which is:

$$c_p = \frac{P}{P_0} = \frac{\frac{1}{4}\rho A_t(\mathbf{v}_\infty^2 - \mathbf{v}_{\text{wake}}^2)(\mathbf{v}_\infty + \mathbf{v}_{\text{wake}})}{\frac{1}{2}\rho A_t \mathbf{v}_\infty^3} = \frac{1}{2}(1-\zeta^2)(1+\zeta), \tag{2.15}$$

with $\zeta = \mathbf{v}_{\text{wake}}/\mathbf{v}_\infty$. Maximum power can be extracted, when the wind speed ratio is $\mathbf{v}_{\text{wake}} = 1/3 \cdot \mathbf{v}_\infty$. Hence, the maximum power coefficient is:

$$c_p = \frac{P}{P_0} = \frac{16}{27} \approx 0.593. \tag{2.16}$$

This ideal power coefficient is known as the Betz factor which can be seen as the theoretical limit for the maximum power extraction from a free air flow (Molly, 1978).
In practice, the Betz limit has not been overcome by any turbine design proposed so far and efficiencies of operating turbines fall short in comparison, as until now turbine design was entirely ignored in the analysis.
Nowadays, most commercially used turbine designs posses a rotor consisting of three blades mounted on a horizontal axis. Blade design uses aerodynamic properties to generate lift, which is transfered into rotational motion. In order to conserve rotational momentum, air parcels passing the rotor plane will be accelerated into the opposite direction, gaining a velocity component tangential to the rotation plane. This rotational motion is conserved while the parcels are propagating downstream

with the wake (Burton et al., 2011).
Complex effects, like tip and root vortexes will not be discussed here, as they are not relevant for this study, but are explained in more detail in Burton et al. (2011). Nevertheless, a closer look at the coarse wake structure while it propagates downstream is presented in the following chapter.

2.2.2 Wake Models and Measurements

To describe the wake propagation downstream a WEC qualitatively, several models of different complexity can be used. The first approach was proposed by Niels Otto Jensen in 1983 - the so called NO Jensen or Jensen-Park Model. Jensen (1983) assumes that the wind speed deficit depends upon the thrust coefficient c_t, the rotor diameter D, the terrain influence, which is represented through the wake decay constant k, and the distance x behind the WEC. Furthermore, the free flow wind speed $\mathbf{v}_\infty$ needs to be known, to calculate the wake velocity $\mathbf{v}_{\text{wake}}$:

$$\mathbf{v}_{\text{wake}} = \mathbf{v}_\infty \cdot \left[1 - \left(1 - \sqrt{1 - c_t}\right)\left(\frac{D}{D + 2kx}\right)^2\right] \tag{2.17}$$

$$\text{with,} \quad k = \frac{1}{2}\left[ln\left(\frac{h_{\text{hub}}}{z_0}\right)\right]^{-1}.$$

The terrain influence parameter k depends upon the roughness length z_0 of the surrounding terrain and the turbine hub height h_{hub}. The Jensen-Park model describes the wake propagation for distances greater than 2 D behind the WEC, as the complex dynamics and turbulent structure directly behind the WEC cannot be reproduced by this simple model.
Jensen (1983) expects the wake expansion to be linearly dependent on the wake decay constant k, leading to a wake width w_{wake} as a function of downwind distance x:

$$w_{\text{wake}} = D + 2kx. \tag{2.18}$$

More recently, a more elaborated model to describe the wake parameters was suggested by Frandsen et al. (2006), based on similarity principles. Frandsen et al. (2006) finds that the wake velocity can be described as:

$$\mathbf{v}_{\text{wake}} = \mathbf{v}_\infty \cdot \left[\frac{1}{2} \pm \frac{1}{2}\sqrt{1 - \left(2\frac{A_0}{A_{\text{wake}}}c_t\right)}\right]. \tag{2.19}$$

$A_0 = \pi(D/2)^2$ is the surface spanned by the rotating blades of the WEC, whereas the wake surface A_{wake} can be calculated with

$$A_{\text{wake}} = \beta A_0 \quad \text{with} \quad \beta = \frac{1}{2}\left(\frac{1+\sqrt{1-c_t}}{\sqrt{1-c_t}}\right). \tag{2.20}$$

Equation 2.19 has two solutions, the positive solution being valid for values of $\left(1-\sqrt{1-c_t}\right) \leq 0.5$ and the negative solution for values of $\left(1-\sqrt{1-c_t}\right) > 0.5$. The wake expansion calculates as:

$$w_{\text{wake}} = D \cdot \sqrt{\left(\beta + \alpha\frac{x}{D}\right)}, \tag{2.21}$$

where α is a constant that needs to be determined experimentally. An initial estimate can be done using the wake decay constant k from the Jensen-Park model:

$$\alpha = \beta\left[(1+2k\frac{x}{D})^2 - 1\right]\frac{D}{x}. \tag{2.22}$$

In the work of Renkema (2007) α is found to be 0.7. In Chapt. 8 both hypotheses for α will be compared to the measurement results. The two models presented above, are widely used for wind park planning and design. Despite the fact that the two wake models are not able to accurately represent the wake structure in the near wake region smaller than two rotor diameters, they furthermore have the shortcoming that they take the wind speed deficit to be constant over the whole wake width at a certain downwind distance. This abrupt step between the undisturbed wind field and the wake region, though, is very unrealistic.
Ainslie (1988) therefore proposes a model that resolves the wake structure orthogonal to the downstream propagation path assuming a Gaussian shape. The wake width is given by

$$w_{\text{wake}} = \sqrt{\left(\frac{3.56 \cdot c_t}{8 \cdot \text{VD}(1 - 0.5 \cdot \text{VD})}\right)\frac{D}{2}}, \tag{2.23}$$

and the vertical profile can be described as a function of the vertical distance from the wake center line d_r:

$$f(d_r) = 1 - \text{VD} \cdot \exp\left[-\left(\sqrt{3.56}\, d_r/b\right)^2\right]. \tag{2.24}$$

The velocity deficit VD in Eq. 2.23 and 2.24 is estimated to be:

$$\text{VD} = c_t - 0.05 - \left[(16 \cdot c_t - 0.5)\frac{I_0}{1000}\right], \tag{2.25}$$

where I_0 is the ambient turbulent intensity. Finally, it is possible to retrieve the wake velocity $\mathbf{v}_{\text{wake}}$ from the velocity deficit VD, as it is defined as:

$$\text{VD} = \left(1 - \frac{\mathbf{v}_{\text{wake}}}{\mathbf{v}_{\infty}}\right). \tag{2.26}$$

In the ongoing work to better resolve the wake structure and the interaction with the ABL in more detail, non analytical Computational Fluid Dynamic (CFD) models, like Large Eddie Simulations (LESs) or Direct Numerical Simulations (DNSs), are used. Recent work was done by Englberger and Dörnbrack (2017), Schröttle et al. (2016), Politis et al. (2012), Wu and Porté-Agel (2012) or Troldborg et al. (2007).

Although model outputs offer valuable results to describe the wake structure, their predictions need to be verified with experiments. Wind tunnel experiments, as conducted by Iungo et al. (2013a), Zhang et al. (2012) and Chamorro and Porté-Agel (2010), do have the advantage that inflow conditions can be controlled, but wind tunnel experiments lack the ability to reproduce a realistic flow field as, due to the downscaling, realistic Reynolds numbers are difficult to achieve. Vermeer et al. (2003) still attests a comparability between wind tunnel experiments and areal WEC-air-flow interaction, as long as appropriate airfoil sections are chosen. Nevertheless, it is inevitable to do full scale field experiments on operating WECs. With modern remote sensing techniques the wind field behind a WEC can be investigated. New insights on the interaction between the ABL flow and a full scale WEC were gathered during the last years, by deploying, for example, scanning Lidar systems, as done by Aitken et al. (2014), Iungo et al. (2013b), Iungo and Porté-Agel (2014), Käsler et al. (2010), Kumer et al. (2015), Rhodes and Lundquist (2013), Smalikho et al. (2013) and Trujillo et al. (2011), or mobile Radar systems, as done by Hirth et al. (2012).

Chapter 3

Lidar

3.1 Lidar - a Remote-Sensing Technology

Lidar possesses the capability to remotely measure almost any atmospheric property, by the means of the properties of laser light. Lidar is able to measure atmospheric properties that cannot be detected by Radar. With its higher sensitivity to aerosols and better spacial resolution, Lidar can perfectly complement Radar measurements, if not substitute them in some cases.
A Lidar system basically consists of a light emitter and a light receiver. Short laser pulses of specific wave length, depending on the properties of the atmospheric parameter of interest, are emitted into the atmosphere. Backscattered photons from the atmosphere are collected by a telescope and analyzed by an optical detection system, which then forwards them to a data acquisition unit, where the signal is processed. From this backscattered signal conclusions on the atmospheric status and properties can be drawn.
A wide range of different Lidar methods are available to measure distinct atmospheric properties. Differential-Absorption Lidar (DIAL), for example, is able to detect ozone and industrial emissions as well as water vapor, when the laser wave length is chosen accordingly. Furthermore, temperature measurements, cloud detection and wind speed measurements can be performed with different Lidar methods. A thorough overview of the existing Lidar methods and specific techniques can be found in Weitkamp (2006).
In this work, a scanning pulsed coherent Doppler wind Lidar system with heterodyne detection was used to measure the wind speed of the atmosphere. The following section provides the theoretical basis for this kind of Lidar method.

3.2 Coherent Doppler Wind Lidar

Pulsed coherent Doppler wind Lidar systems emit short laser pulses with highly stable frequency into the atmosphere. There, the light pulses are reflected by molecules and particles. The backscattered signal from the atmosphere, as in any other Lidar system, can be expressed by the Lidar equation

$$P(R) = KG(R)\beta(R)T(R). \tag{3.1}$$

The power $P(R)$ detected by the Lidar system for any distance R therefore depends upon two system inherent parameters, K and $G(R)$, which respectively are the performance of the Lidar system and the range dependent measurement geometry, and two parameters dependent on atmospheric conditions. $\beta(R)$ designates the backscatter coefficient at distance R, a measure for the atmospheric ability to backscatter light into the incident direction, whereas $T(R)$ denotes the transmission, which is responsible for signal losses.
From the incoming signal, the velocity of the measured air volume can be calculated due to the laser pulses' relative frequency shift. This phenomenon, called the optical Doppler effect, is well known and velocities can easily be calculated given that the group velocity of the emitted light pulse is known in the corresponding medium.
The optical Doppler effect describes the frequency shift of a electro-magnetic wave, caused by an object moving relative to the receiver. This frequency shift Δf, in comparison to the original frequency f, is proportional to the object's velocity $\mathbf{v}$ divided by the group velocity c,

$$\frac{\Delta f}{f} \sim \frac{\mathbf{v}}{c}. \tag{3.2}$$

The velocity of light in air is well-known and given that the emitted laser frequency f_0 is stable, the measured frequency f 'emitted' by a moving air mass is

$$f = f_0 \left(1 + \frac{\mathbf{v}}{c}\right). \tag{3.3}$$

The illumination of the measurement volume by the laser pulse, however, causes a modification of Eq. 3.3, as the light is traveling through the air towards the measurement volume where it is reflected and afterwards travels back to the receiver. The measured frequency at the detector consequently will be:

$$f = \left[f_0 \left(1 + 2 \cdot \frac{\mathbf{v}}{c}\right)\right]. \tag{3.4}$$

As particles as well as molecules are traveling with the measured air mass, it is necessary to distinguish between their contributions to the backscattered signal. The velocity distributions for each of the components is quite distinct. Molecules do have a large velocity distribution due to thermal random motion, which complicates the detection of a frequency shift, as wind speed, in comparison to the thermal motion is small and only slightly influences the velocity distribution. On the other hand, particles traveling with the mean wind, do have a smaller velocity distribution and therefore a clear shift in the frequency can be detected.
It is therefore important to choose the laser wavelength according to the expected backscatter signal. The molecular signal is proportional to λ^{-4} (Rayleigh Scattering), whereas the signal from aerosols is proportional to the range of λ^{-2} to λ^{1} (Mie Scattering). As a result, the aerosol to molecular background backscatter ratio gets more favorable for larger wavelength and Lidar systems designed to operate in the ABL relaying on the aerosol backscatter component, work with wavelengths in the µm range.
The aerosol density in the atmosphere decreases with height, making the lower atmosphere and explicitly the ABL a perfect region for high-resolution Lidar applications.
To detect the frequency shift, caused by the Doppler effect, in the incoming laser beam, detection needs to be very sensitive. Heterodyne detection, in comparison to direct detection, uses a second laser source, instead of passing the incoming beam through several narrow-band optical filters, providing the necessary accuracy.
The setup of a heterodyne detection system can be seen in Fig. 3.1. The system consists of a pulsed Laser Transmitter (TE), a Local Oscillator (LO), a Locking Loop (LL), two heterodyne detectors (D1, D2), as well as an optical instrument.
A short Gaussian shaped pulse is emitted into the atmosphere. The outgoing signal as well as the incoming frequency shifted pulse are mixed with the local oscillator from where it is transmitted to the heterodyne detector D1 or D2 respectively. The local oscillator and the pulsed laser transmitter are connected by a locking loop and do have a small difference in wave length. This difference is important to detect the sign of the frequency shift in the incoming signal.
When mixing the frequency shifted incoming laser pulse with the local oscillator pulse, the resulting signal contains the sum $f_{\mathrm{LO}} + (f_0 + \Delta f)$ as well as the difference $f_{\mathrm{LO}} - (f_0 + \Delta f)$ of the two mixed signals. The superposition therefore consists of a high frequency part and a low frequency part. The high frequency part cannot be detected as the high frequency cutoff is well below the superposition of the

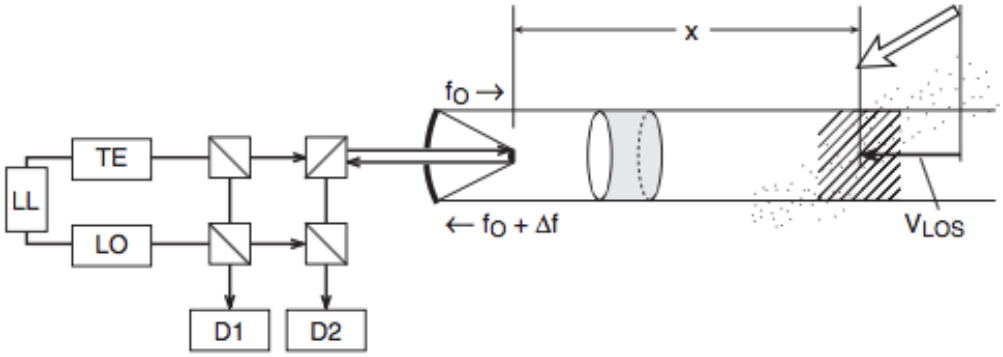

Figure 3.1 – *Setup of a heterodyne detection system for a pulsed Doppler Lidar system. LL - Locking Loop, TE - Pulsed Laser Transmitter, D1,D2 - Heterodyne Detectors. From Weitkamp (2006).*

local oscillator frequency and incoming frequency. The low frequency component, however, can be detected with good accuracy. As a result, Δf can be determined and v_{LOS} can be calculated with Eq. 3.4. v_{LOS} is the measured air volume's velocity in Line Of Sight (LOS) direction as only this velocity component contributes to the detected Doppler shift (Weitkamp (2006)).
In the next section the Windcube 200S from Leosphere, which was used during the measurement campaign described in Chapt. 5, will be introduced.

3.3 The Windcube 200S

The Windcube 200S is a scanning Doppler wind Lidar system with a coherent class IV pulsed laser source and fiber optics, working at a wavelength of $\lambda = 1543\,\mathrm{nm}$, using a heterodyne detection system. The 3D hemispherical scanner head allows for distinct scan patterns - from simple LOS measurements, over Range-Height Indicator (RHI), as well as Plan-Position Indicator (PPI) scans, to Complex Trajectory (CT) scans. The most important hardware parameters are listed in Tab. 3.1.
Three different Full Width Half Maximum (FWHM) pulse width, 100 ns, 200 ns and 400 ns, can be chosen for different physical resolutions in beam direction. The Pulse Repetition Frequency (PRF) is 40 kHz, 20 kHz or 10 kHz, depending on the corresponding pulse width.
The measurement volume is defined by the pulse width, the telescope aperture and the broadening of the laser beam on its way through the atmosphere. In LOS direction the measurement volume length can approximately be calculated to

$$x_{MV} = \frac{c\tau}{2}, \tag{3.5}$$

where τ is the pulse length (FWHM) and c is the speed of light. The effective physical resolution, however, is more difficult to evaluate and the interested reader is referred to Banakh and Smalikho (2013).
The Windcube 200S comes with a software to process and analyze the backscattered signal from the atmosphere. A second software package that allows for synchronization between Lidar systems, called WindScanner, was obtained from the Technical University of Denmark (DTU), to be able to perform multi Lidar measurements in order to resolve the three-dimensional wind vector (Vasiljević et al., 2016).

Scanner	3D hemispherical scanner head
Telescope Aperture	8 cm
Laser Class	1M
Wavelength	1543 nm
PRF	40 kHz, 20 kHz, 10 kHz
Pulse Energy	25 µJ, 50 µJ, 100 µJ
Pulse Width (FWHM)	100 ns, 200 ns, 400 ns
Physical Resolution	25 m, 50 m, 75 m 100 m
Range in ABL	6000 m
Sampling Rate	250 MHz
v_{LOS} Error	< 0.5 m/s
v_{LOS} Range	-30 m/s to 30 m/s

Table 3.1 – *Windcube 200S Specifications*

3.4 Data Analysis

The Windcube 200S processes the backscattered signal so that the LOS velocity can be read out. Therefore, the signal of the outgoing pulse as well as of the incoming backscattered light is detected and recorded.
Figure 3.2 shows one such signal recorded by the Windcube 200S. Though the signal is recorded over time, every sample step corresponds to a distance. With the sample frequency $f_{\text{sample}} = 250\,\text{MHz}$, the corresponding distance $x_{\text{sample}} = {}^{c}/_{(2 \cdot f_{\text{sample}})}$ to one sample step can be calculated to $x_{\text{sample}} = 0.6\,\text{m}$.
To be able to analyze the frequency shift of the backscattered light, the recorded

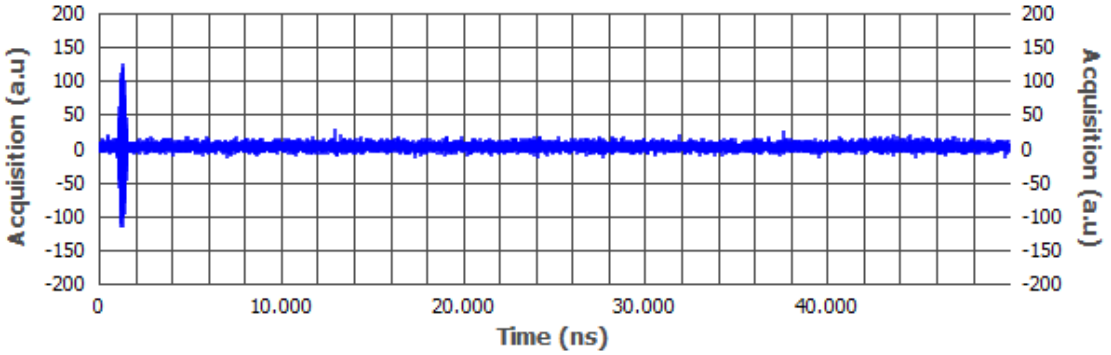

Figure 3.2 – *Recorded signal by the Leosphere Windcube 200S for one outgoing laser pulse. The first strong signal corresponds to the outgoing pulse, whereas the signal afterwards comes from the backscattered laser light from the atmosphere. The sampling rate to record the signal is* 250 MHz.

signal needs to be transfered into the frequency domain. This is done by a Fast-Fourier Transformation (FFT).

To perform the FFT, an interval of samples, called range gate, is selected. The range gate is placed in such a way that the range gate center corresponds to the distance to be analyzed. Depending on the chosen pulse length and the number of samples used to define the range gate, the physical resolution is defined (Banakh and Smalikho, 2013).

20 000 accumulated signals, on which the FFT is performed, are used to reduce the noise underneath a certain threshold. In a next step a Maximum Likelihood Estimate (MLE) to detect the frequency maximum is applied to the resulting frequency domain, finally determining the frequency of the backscattered pulse. This procedure sets a lower limit of 50 ms to the acquisition time for one LOS measurement. In a final step v_{LOS} can be calculated with Eq. 3.4.

The method described above can be applied at various range gate distances simultaneously allowing velocity retrieval at multiple distances along one LOS. It is worth noting that a displayed resolution, with a range gate separation smaller than the physical resolution, can be achieved by overlapping FFT intervals, the minimum being a range gate separation of 1 m. However, physical information is then shared between neighboring range gates and measurement values are not statistically independent.

3.5 Other Doppler Wind Lidar Systems

Currently, there are several scanning Doppler wind Lidar systems on the market that are able to measure the wind speed in the ABL comparable to the Windcube 200S. However, these systems differ in core parameters and are offering advantages and disadvantages. In the following, a rough overview over some of the existing systems and their core abilities is given.

A Lidar system also deployed at the measurement campaign described in Chapt. 5, is the Halo Photonics Stream Line. The Stream Line is a scanning pulsed Doppler Lidar system. Its scanning capability covers a hemisphere and complex trajectories can be scanned. This Lidar system is operating at a wave length of 1.5 µm, as is the Windcube 200S. Then again, pulse length (160 ns), sampling rate (50 MHz) as well as the PRF (15 kHz) differ from the Windcube 200s settings. Physical resolution of the Stream Line is about 48 m, nearly matching the 50 m resolution of Windcube 200S.

The Stream Line Lidar system matches the parameters of the Windcube 200S (middle resolution) quite well. Nevertheless, there are substantial differences in the system's capabilities. The Windcube 200S offers a wider range of settings to adapt the physical resolution and the maximum range and is therefore able to better adapt to measurement requirements. In contrast, the Windcube 200S is heavier (230 kg), which complicates deployment in the field. This is one of the main advantages of the Stream Line. The rather light instrument (80 kg) can easily be carried by four men and therefore deployment is easy, which allows installation in rough and exposed terrain (Päschke et al., 2015).

Another system commercially available is the WindTracer produced by Lockheed Martin. This Lidar system differs, not only in dimensions, but also in the laser type from the two systems described above. The WindTracer is operating at a wavelength of 1617 nm with a pulse energy of 2.5 mJ. The typical range is about 18 km and can go as far as 33 km in ideal conditions. Based on the pulsed Doppler technology, a physical resolution similar to the minimum spacial resolution of the Windcube 200s (100 m) is given.

Similar to the Windcube 200s and the Stream Line, the WindTracer is able to do hemispherical scanning and the PRF of this system is 750 Hz.

In comparison to the two systems described above, the WindTracer is the most powerful instrument to map wind velocities over greater distances. This capability, however, comes with a clear downside of system dimensions. The WindTracer is, with a size of 1.97 m × 2.44 m × 3.29 m, the larges of the three instruments and also

the heaviest. A weight of 2600 kg complicates field deployment and deployment flexibility (LockheedMartin, 2017).
As above can be seen, every system posses advantages and downsides and deployment therefore should be adapted according to the research goals.

Chapter 4

Virtual Lidar as a Campaign Planning Tool

To properly plan a measurement campaign with Lidar systems to investigate a turbulent wind field, it is necessary to know which physical characteristics can be resolved as well as the degree of accuracy inherent to certain measurement procedures.
Therefore, Stawiarski (2014) and Bingöl et al. (2008) developed the concept of employing virtual Lidar systems. The idea is to model the measurement procedure of a Lidar system, to understand how detailed a wind field can be analyzed with certain scanning scenarios and to be able to plan specific measurement strategies.
To gain insight into the accuracy of the Windcube 200S and its ability to resolve the wake structure and the wake properties produced by a WEC, a virtual Lidar system, emulating the physical core parameters of the Windcube 200S, was implemented and tested on a simulated turbulent wind field featuring a WEC, as described in Schröttle et al. (2016). This LES using the Eulerian/semi-LAgrangian Geophysical (EULAG) fluid solver, is able to reproduce the main properties of turbulent wind fields and WEC wake.
In comparison to the real campaign site in Perdigão, simplifications were made in respect to topography and roughness of the terrain in the simulation run. A neutral plain wall boundary layer was used, instead of a double ridge, to simulate the wake effects.
The simulation was initiated with neutral stratification and a mean wind speed of $10\,\mathrm{ms}^{-1}$ on a cubic grid with the length of 2047 grid points in main wind direction (x-Axis), 192 grid points in horizontal elongation (y-Axis) and 300 grid points in the vertical axis (z-Axis), with a physical spacing of 2 m each. The WEC was

located at position $x = 2046\,\mathrm{m}$, $y = 191\,\mathrm{m}$ with a hub hight of $z = 150\,\mathrm{m}$. The rotor diameter was $D = 100\,\mathrm{m}$.
For the analysis twelve snap shots of the simulated wind field were taken every two and a half minutes to assemble a simulated time span of 27.5 min.
In the following, the main features of the implementation for a virtual Lidar system to sample the Windcube 200S and the methodology applied to analyze coplanar dual Lidar measurements will be outlined and results from sensitivity studies presented.

4.1 Implementation

The implementation of the virtual Lidar system mainly follows the methodology outlined by Stawiarski (2014). In a first step a scanning scenario needs to be defined. This means that scanning angles as well as range gate positions need to be specified and expressed in the coordinate system of the LES simulation. In a next step, the data from the LES simulation is linearly interpolated onto the Lidar beam. Considering the theoretical assumptions made by Frehlich et al. (1998), that the radial velocity measured by a pulsed Doppler Lidar system is given by the integral over the actual radial velocity multiplied by a weighting function, we can calculate the LOS velocity v_{RGC} at the range gate center the following way:

$$v_{\mathrm{RGC}}(x_0) = \int_{-\infty}^{\infty} v_{\mathrm{LOS}}(x) W_{\Delta \mathrm{x}}(x - x_0) dx. \tag{4.1}$$

The weighting function $W_{\Delta x}$ is defined as:

$$W_{\Delta \mathrm{x}}(y) = \frac{1}{\Delta x} \int_{-\Delta x/2}^{\Delta x/2} I_n(y - x) dx, \tag{4.2}$$

with x_0 being the range gate center and x denoting the distance from x_0. Δx is the range gate length and I_n the normalized Gaussian pulse envelope.
In a closer analysis it can be seen that the shape of the weighting function only depends upon the relation between pulse length and range gate length. The weighting function is a superposition of the box shaped indicator function of the range gate length and the Gaussian pulse envelope. Examples for the shape of the weighting function, $W_{\Delta \mathrm{x}}$, to simulate the different physical resolutions of the Leosphere Windcube 200S, can be seen in Fig. 4.1. It is important to note, that the spatial resolution of a Lidar system is limited by the Gaussian pulse. This means that no point measurements can be done, as pulse length and frequency

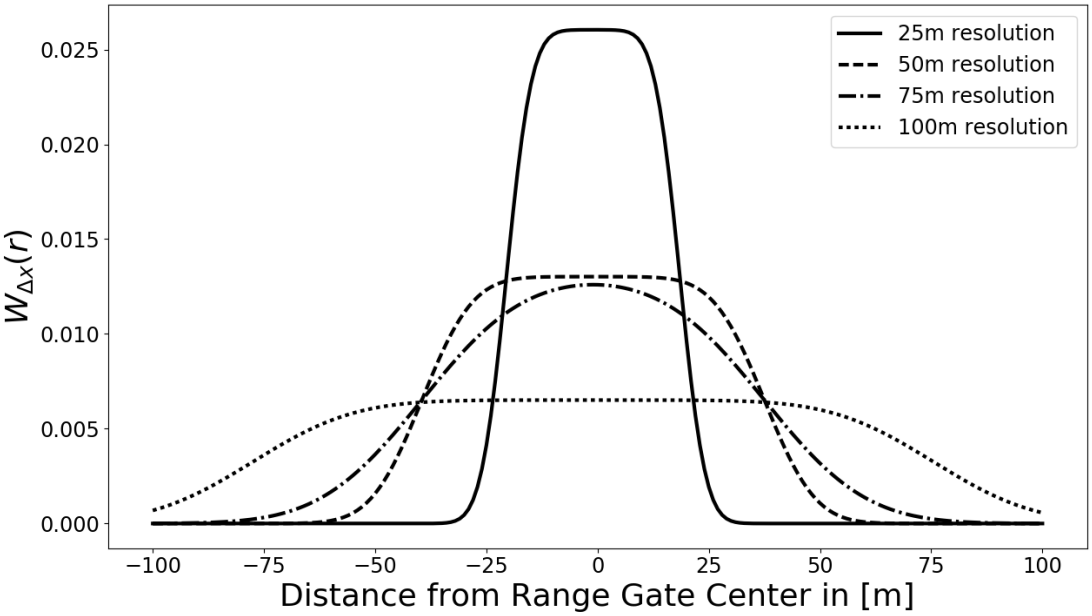

Figure 4.1 – *Weighting functions to simulate the* v_{LOS} *measurement for the physical resolutions of the Windcube 200S for its different pulse widths.* 25 m *resolution (solid,* 100 ns*, 64 FFT points),* 50 m *resolution (dashed,* 200 ns*, 128 FFT points),* 75 m *resolution (dash-dotted,* 400 ns*, 128 FFT points) and* 100 m *resolution (dotted,* 400 ns*, 256 FFT points). The range gate center is situated at* $x = 0$*.*

accuracy are inversely proportional. To maintain a stable frequency, necessary to detect small frequency alterations by the Doppler effect, the pulse length cannot be made infinitely small.
Equation 4.1 then gives v_{LOS} as detected by the virtual Lidar system. In a last step, the measurements are interpolated back onto a Cartesian coordinate system, to be able to compare the Measured Wind Field (MWF) to the Original LES Wind Field (OWF).

4.2 Coplanar Scanning Methodology

The methodology for data retrieval from the simulated turbulent wind field was constructed to sample the data retrieval routines for real dual Lidar measurements as they were planned to be executed in the field campaign described in Chapt. 5. Nevertheless, simplifications had to be taken into account, as limitations imposed by the time evolution of the simulation and calculation expenses hindered a more realistic approach to reproduce Lidar measurements.
Sensitivity studies, to analyze the influence of different scan parameters on the

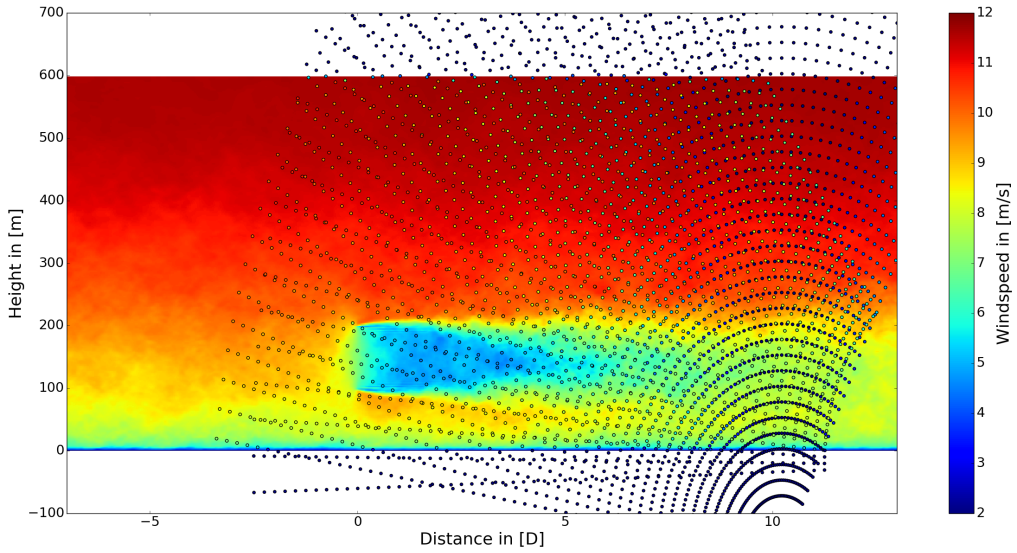

Figure 4.2 – *Visualization of the averaged v_{LOS}, measured by a coplanar scan with two virtual Lidar systems (every circle corresponds to one range gate), plotted against the averaged 'original' turbulent LES wind field featuring a wind turbine, situated at $x = 0\,\mathrm{D}$ and $z = 150\,\mathrm{m}$.*

ability to resolve WEC wake characteristics, were undertaken for a Coplanar Scan (CS) scenario, using a pre-elaborated planning tool. The evaluation was done by comparing the measured wake structure to the 'original' LES wake structure.
A CS consists of the simultaneous measurement of two Lidar systems that are aligned with the wind turbine and the main wind direction. The two Lidar instruments perform RHI scans to cut the turbine wake, as can be seen in Fig. 4.2. From the two RHI scans a vertical intersect through the wake structure can be calculated by interpolation and solving the system of linear equations to derive the two-dimensional wind vector in x and z direction:

$$\begin{pmatrix} cos(\varphi_1) & sin(\varphi_1) \\ cos(\varphi_2) & sin(\varphi_2) \end{pmatrix} \cdot \begin{pmatrix} u \\ w \end{pmatrix} = \begin{pmatrix} v_{\mathrm{LOS}_1} \\ v_{\mathrm{LOS}_2} \end{pmatrix}. \tag{4.3}$$

φ_1 and φ_2 in Eq. 4.3 denote the elevation angle of Lidar system one and two, respectively. u is the horizontal wind component and w the vertical one.
The further methodology to evaluate CSs, in order to retrieve wake parameters, will only concentrate on the horizontal wind component in x direction, as the wake structure in this component is more pronounced.
In the following, a method similar to the one proposed by Trujillo et al. (2011) and Aitken et al. (2014) will be introduced to analyze the wake parameters of interest: the wake center position, the velocity deficit and the vertical wake width.

The detrended vertical wake profile, at a certain downstream position, can be modeled as either a Gaussian, for the far wake, or a double Gaussian profile, for the near wake, as proposed by Ainslie (1988):

$$\text{Model}_1: \; u(z) = A \cdot e^{\left(-\frac{(z-b)^2}{2\sigma^2}\right)}; \tag{4.4}$$

$$\text{Model}_2: \; u(z) = A \cdot \left[e^{\left(-\frac{(z-b_{\text{upper}})^2}{2\sigma^2}\right)} + e^{\left(-\frac{(z-b_{\text{lower}})^2}{2\sigma^2}\right)}\right]. \tag{4.5}$$

The parameter A in Eq. 4.4 and 4.5, denotes the amplitude, while the parameters $b, b_{\text{upper}}, b_{\text{lower}}$ designate the position of the maximum of the Gauss profiles and the parameter σ describes the Gaussian standard deviation, which controls the width of the Gaussian function.
Both models are fitted, by a least square method, to the vertical wind profiles every 10 m. A simple statistics F-test with a p-value of 0.05 is applied to choose, whether the more complex, double Gaussian, or the simple, single Gaussian, model fits the vertical velocity profile more adequately. The threshold 0.05 is chosen, as the simpler model would always be rejected in benefit of the more complex model, for p-values smaller than 0.05 (Kleinbaum et al., 2013).
It is now possible to retrieve the wake characteristics based on the fitted parameters A, b or $b_{\text{upper}}, b_{\text{lower}}$ and σ. The wake center position can be defined as:

$$z_{\text{wake}} = b \quad \text{or} \quad z_{\text{wake}} = \frac{b_{\text{upper}} + b_{\text{lower}}}{2}; \tag{4.6}$$

The velocity deficit VD, defined as in Eq. 2.26, can now be rewritten to:

$$\text{VD} = (1 - \frac{u_{\text{wake}}}{u_\infty}) = \frac{A}{u_\infty}; \tag{4.7}$$

and the wake width w_{wake} can be defined, similar to Aitken et al. (2014), as the 95 % confidence interval of the Gaussian profile:

$$w_{\text{wake}} = 4 \cdot \sigma; \tag{4.8}$$

w_{wake} for the double Gaussian profile can be defined as:

$$w_{\text{wake}} = (b_{\text{upper}} - b_{\text{lower}}) + 4 \cdot \sigma. \tag{4.9}$$

4.3 Sensitivity Studies

With the methodology described in the previous section, it is possible to compare the velocity deficit, the vertical wake width as well as the wake center position between the MWF and the OWF, which enables an investigation of the influence of the most important scan parameters. Lidar systems were positioned at ($x = 1022\,\mathrm{m}, z = -172\,\mathrm{m}$) and ($x = 1425\,\mathrm{m}, z = -27\,\mathrm{m}$) downstream the WEC, so that they would reproduce the scanning geometry of the field campaign described in Chapt. 5.
There are three main scan parameters that can be changed at the Windcube 200S: the laser pulse length together with the FFT window and therefore the physical resolution; the rotational velocity of the scanner head in combination with the accumulation time and therefore the angular resolution and the range gate spacing, which is the distance between two measurement points.
Sensitivity experiments to distinguish between the effects on the wake resolution of the three scan parameters were designed for both Lidar instruments scanning the OWF with an RHI scan in the following way:

- measurement series with constant range gate spacing of 25 m and variation of angular resolution; $\Delta\varphi \in [0.1°, 0.3°, 0.5°, 1.0°, 2.0°, 3.0°]$
- measurement series with a fixed angular resolution of 0.5° and variation of range gate spacing; $\Delta x_R \in [2\,\mathrm{m}, 5\,\mathrm{m}, 10\,\mathrm{m}, 25\,\mathrm{m}]$

These two measurement series were run for two different physical resolutions of 25 m and 50 m. Linear interpolation of the two RHI scans was done onto a 10 m times 10 m regular grid on which the linear system of equations (Eq. 4.3) was solved to deduce the wind components u and w.
It has to be noted that the measurement of the OWF snap shots excludes the time evolution of a turbulent wind field during the scan period. This fact will, in comparison to a more realistic scenario, where the wind field is evolving with time during the scan period, lead to small deviations from a real wind field. However, errors are supposed to be small, as the time for one scan (typically 30 s to 2 min) is significantly smaller than the time for the whole measurement period, which is 27.5 min.
For each setting, the MWFs were averaged over the whole simulation period, in

order to reduce statistical effects and to increase statistical stationarity (Iungo and Porté-Agel (2014)). The resulting field is then merged into horizontal bins of 10 m to obtain vertical wind profiles $u(z)$, ranging from 10 m to 300 m above the ground. For each bin the two wake models (Eq. 4.4 and 4.5) are fitted to the detrended wind flow behind the wind turbine. Initial guesses for the wake parameters to fit the Gaussian and the double Gaussian wake model are: $A = \max(u(z))$, $b = h_{\text{hub}}$, $b_{\text{upper}} = h_{\text{hub}} + 20\,\text{m}$, $b_{\text{lower}} = h_{\text{hub}} - 20\,\text{m}$ and $\sigma = \sigma(u(z))$.
To detrend the downwind velocity profiles, the ambient wind flow was modeled as a logarithmic profile,

$$u_\infty(z) = \frac{u_*}{\kappa} ln\left(\frac{z}{z_0}\right), \tag{4.10}$$

where u_* is the shear velocity, κ the Van-Kármán constant, z the hight and z_0 the surface roughness. Equation 4.10 was fitted to the undisturbed wind field 2 D $\pm$ 0.5 D in front of the wind turbine, similar to the distance used by Käsler (2011). The fitting approach to model the ambient wind flow was chosen to represent an estimation of the vertical wind profile as would be done in the case of a field campaign (Aitken et al. (2014)).
The method to access the wake parameters explained above was also applied to the averaged OWF.
The wake parameters' absolute errors were finally averaged over the horizontal extension up to 10 D behind the WEC in mean wind direction and plotted against the different scan parameters.

4.4 Results

Angular variation

Figure 4.4 displays the absolute velocity deficit error, the absolute wake width error as well as the absolute wake center position error plotted against the angular resolution. In all three plots a clear increase of the absolute error with a decrease in angular resolution can be seen for both physical resolutions of 50 m and 25 m. This increase can be explained by the fact that the spatial distribution of measurement points is decreasing for lower angular resolutions. Therefore, distances between two measurement points are increasing, leading to scarcer velocity information and therefore to higher errors. No wake structure at all could be detected by the evaluation method for angular resolutions lower than 5°.

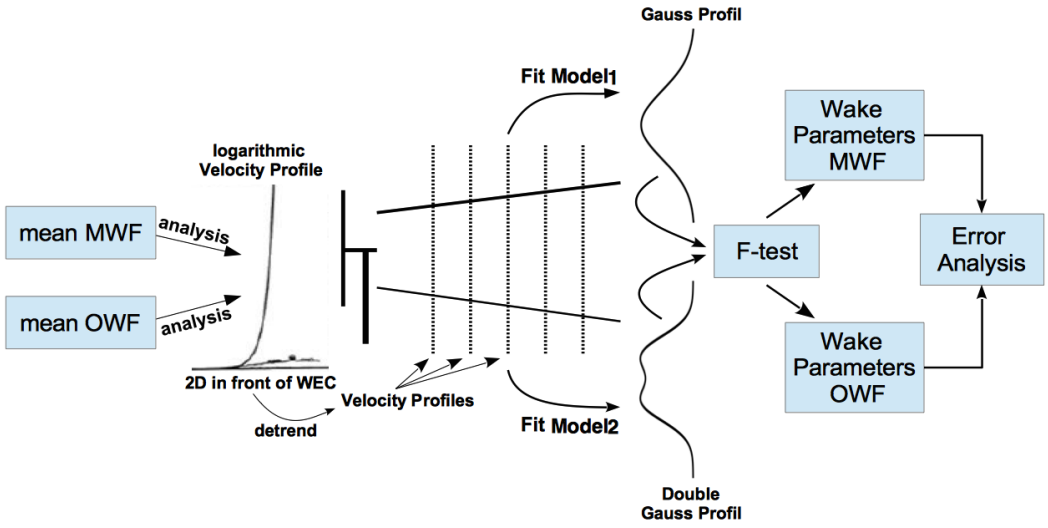

Figure 4.3 – *Diagram to visualize the analysis steps for the virtual Lidar measurements in the LES wind field in order to realize the sensitivity experiments explained in Chapt. 4.3.*

However, the decrease in absolute error with an increase in angular resolution is not linear, but seems to be of a somewhat logarithmic behavior. Biggest gains in accuracy for higher angular resolutions can be seen for the velocity deficit and the wake width, whereas the error for wake position only decreases marginally for angular resolutions below 2°. Nevertheless, a lower limit for improvement in resolving the wake properties seems to be established for the two other parameters as well. It seems that an angular resolution greater than 0.5° only yields small improvements in resolving wake properties, if at all.

Taking a closer look at the absolute error for the two different physical resolutions, it can be found that differences are small. The biggest difference between the two resolutions can be found for the velocity deficit error, as a higher physical resolution in this case is able to better reproduce velocity peaks. The two other evaluated error sets hardly differ at all.

One result that is startling at first sight, is the slightly greater error for a higher physical resolution at lower angular resolutions considering the wake width. For a higher angular resolutions on the contrary, the higher physical resolution leads to better results. This behaviour can be explained with the fact that for lower angular resolutions, measurement points are spaced more widely in x direction, which leads to gaps bigger than the 25 m of physical resolution. In these cases the 50 m resolution can provide velocity information over a wider spatial range, leading to smaller errors in comparison.

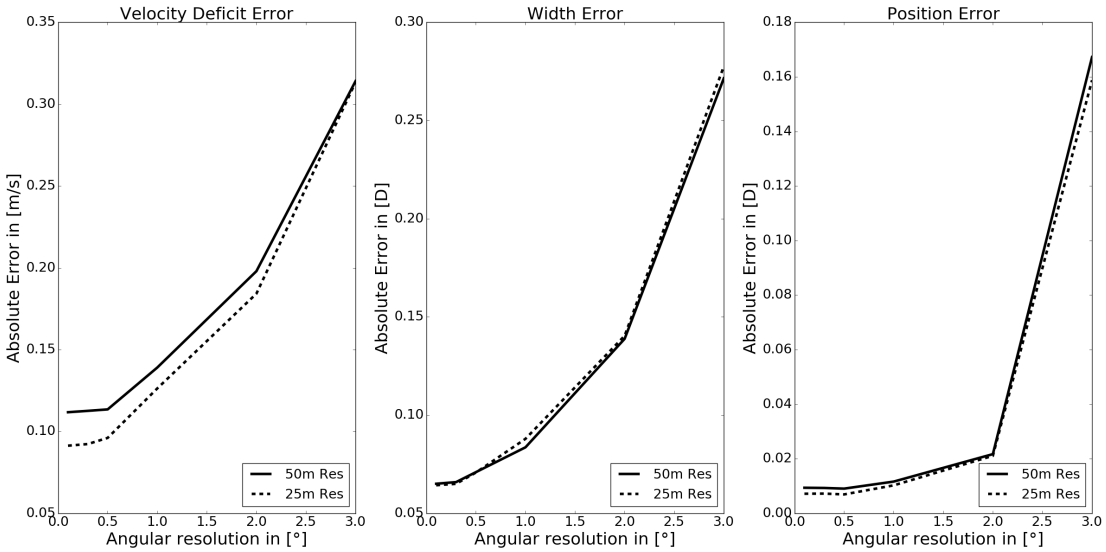

Figure 4.4 – *Absolute error plots for the velocity deficit (left), the wake width (middle) and the wake center position (right) in dependence on the angular resolution for the CS scenario.*

Range gate spacing

The results from the sensitivity experiments in respect to a change in range gate spacing, show similar results to the ones done for the angular resolution. The absolute error increases for all wake parameters with greater range gate spacings. However, the magnitude of response to a variation of the range gate spacing is about 10 times smaller than the response to a variation in angular resolution and absolute errors are two orders of magnitude smaller than for the angular resolution (see Fig. I.1). This is due to the fact that the physical resolution of 25 m and 50 m cannot be compensated by smaller range gate spacings. The overlap of FFT points is used to achieve a range gate spacing smaller than the physical resolution. Measurement results for neighboring points with a spacing smaller than the physical resolution are therefore not statistically independent from each other.
The influence of the physical resolution on the errors is very small.

Conclusion

A first conclusion on the investigation of wake parameters with Lidar can be drawn from the results above. It is important to adequately choose the measurement parameters in order to measure the wake. It can be seen that there are basically two limitations to the measurement of the wake structure. The first limitation is the physical resolution of the Lidar itself. However, if measurement strategies are

not properly matched to the physical resolution of the Lidar, uncertainties and errors are increasing and hinder better wake measurements.
It could be shown that the most sensitive scan parameter is the angular resolution. Higher angular resolutions significantly reduce errors in the wake detection. Nevertheless, a compromise between the time necessary for one scan and the angular resolution has to be found. Results point into the direction that angular resolutions below 0.5° do not provide significantly better wake characterization.
The physical resolution of the Lidar instrument is of minor importance when evaluating the wake structure in comparison to the angular resolution. But for high angular resolutions some accuracy can be gained when determining the velocity deficit if the higher physical resolution is used. On the other hand, the loss in signal strength for higher physical resolutions will cause errors in the data acquisition as the Carrier to Noise Ratio (CNR) is reduced. The increase in accuracy for the higher physical resolution is therefore only worth the reduction of the CNR, when the atmospheric backscatter properties are good. To conduct a more complete planning to optimize scanning scenarios, the simulation to emulate the Windcube 200S would have to be expanded to feature the atmospheric scattering properties, as well as a solution of the Lidar equation (Eq. 3.1).
In respect to range gate spacing it was found that a spacing equal to the physical resolution of the Lidar system is sufficient to resolve the wake structure. Gains for smaller distances are negligible.
From the sensitivity studies above, valuable information could be generated to better plan the measurement campaign, proving that virtual Lidar instruments can help to set scan parameters to resolve desired flow structures.

Chapter 5

Measurement Campaign of a WEC in complex Terrain

In the context of the New European Wind Atlas (NEWA) project, the measurement campaign in Perdigão, Portugal is the largest of several experiments, with the purpose to validate mesoscale meteorological models for better wind assessment throughout Europe and Turkey.
The NEWA seeks to be an openly accessible wind atlas providing necessary information for WEC installation, such as local wind resources, extreme winds, turbulence and wind shear. A total of seven field experiments are supposed to provide measurement data to assess these parameters. Good data sets in the heights interesting for energy production between 40 m and 300 m above ground level, are scarce. To fill this knowledge gap, complex measurement strategies are employed, combining in-situ measurements from meteorological masts with remote sensing techniques. Common to all the projects contributing to the NEWA, is the use of long range Doppler wind Lidar systems.
The seven validation experiments take place in a timespan of roughly two and a half years, beginning in late 2015 until mid 2018. To this day, six of the seven contributing experiments have already been carried out with the last experiment in Aliaz being currently executed (Mann et al., 2017).
This thesis however, only focuses on the Perdigão 2017 experiment, in the context of which the data, analyzed in Chapt. 7 and Chapt.8, was obtained. Being the largest of the NEWA experiments, various research groups from different institutions were involved in the project not only from Europe, but also the USA. Contributing institutions are: Technical University of Denmark, University of Porto, University of Notre Dame, University of Colorado (Boulder), University of Oklahoma, Univer-

sity of California (Berkeley), U.S. Army Research Laboratory, National Center for Atmospheric Research, German Aerospace Center, Instituto Português do Mar e da Atmosphera.
Together these groups deployed during the intensive operation period from the 1st of May until the 15th of June 2017, an instrument zoo of over 180 different measurement instruments (meteorological mast equipment not counted) to characterize the atmospheric flow over a parallel double ridge in order to create a data base of unprecedented detail, in spatial as well as temporal resolution. An overview of the measurement site in Perdigão and some of the instruments deployed can be found in Fig. 5.1 and Tab. II.1.
The DLR contributed to the project with three scanning Doppler wind Lidar systems of type Windcube 200S from Leosphere, described in Chapt. 3.3, as well as a microwave radiometer and several microphones. The main focus of the DLR research group is on the interaction between the atmospheric flow and the WEC, situated on one of the two ridges. The research goals are:

- the observation of coherent flow structures and their quantification up- and downwind of the wind turbine;
- the dependency of flow structures on atmospheric conditions;
- the interaction between inflow and turbine wake and its dependency on thermal stability.

5.1 The Terrain

The experimental site was located in the Serra de Perdigão, Portugal, approximately 165 km north-east and 177 km south-east air-line distance to Lisbon and Porto, respectively, in the district of Vila Velha de Ródão. Bordered in the north by the Serra de Estrela, the highest mountain ridge in Portugal with 1991 m, and Spain in the east, this rural region features two nearly parallel mountain ridges. The area covered by the experiment is about 8 km × 8 km, covering the two ridges and the valley in its middle, as well as part of the surrounding terrain. The ridges are orientated in a NW-SE direction standing approximately 1.4 km apart. They exhibit an angle of 37° to the north in a counterclockwise direction. The SW ridge (481 m), where the wind turbine is situated in the middle of the test field, is slightly higher than the NE ridge (454 m). The valley between the ridges is 296 m above see level. The two ridges are surrounded by rolling terrain, interspersed with lower

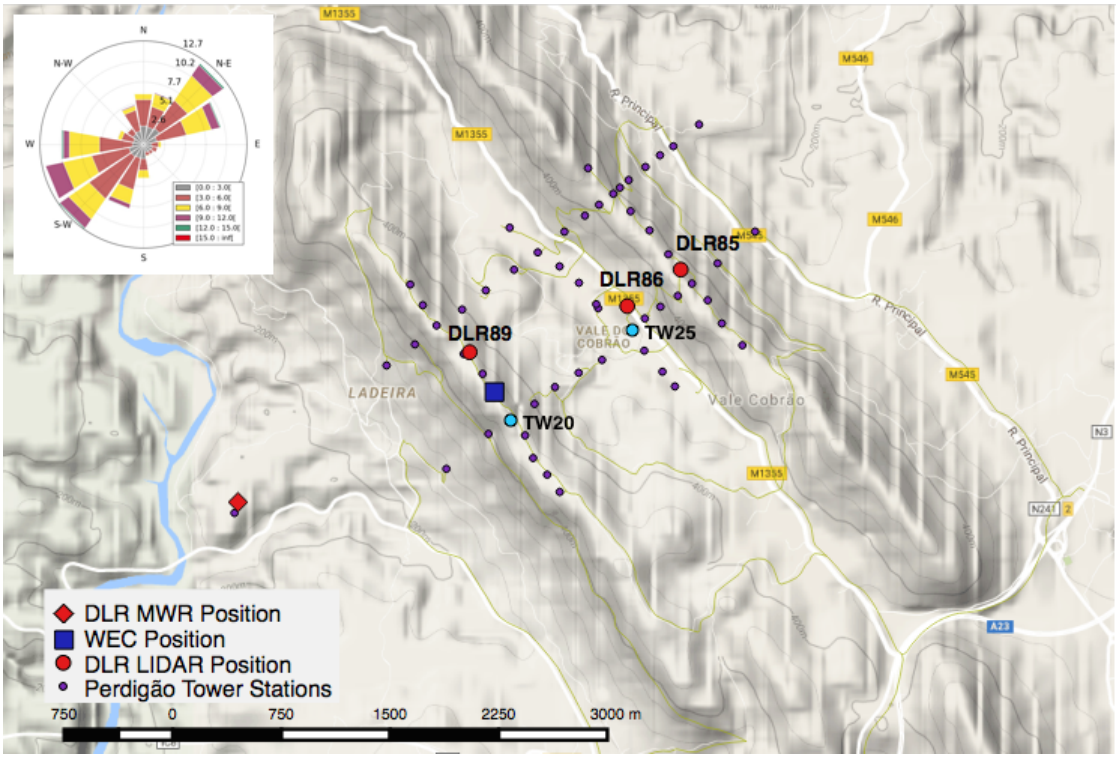

Figure 5.1 – *Overview over the Perdigão experimental site. The red dots denote the three DLR Lidar systems' positions. The blue square denotes the WEC position and the red square denotes the MWR position. TW20 and TW25 are marked as turquoise dots. To give a better overview of the total instrumentation on site, further tower positions are displayed as violet dots. A complete list of instruments deployed on site can be found in Tab. II.1.*

laying riverbeds.

Vegetation in the region is dominated by eucalyptus woods and olive tree plantations, together with herbs and bushes at the ground level. Urbanization is non existent, except for a little village consisting of ten houses at the valley bottom.

The main wind direction is SW or NE with an average wind speed of $6\,\mathrm{ms}^{-1}$, orientated perpendicular to the ridge from either side (see wind rose in Fig. 5.1). Maximum wind speeds with velocities up to $20\,\mathrm{ms}^{-1}$ were detected during a test phase (Mann et al., 2016). This makes the experimental site nearly ideal, as it can be seen as a quasi two-dimensional structure, reducing the complexity for modeling purposes, but nevertheless complex enough to exhibit distinct phenomena idiosyncratic to the setting.

Rodrigues et al. (2016) describes some of the phenomena found in an earlier campaign at the same site in 2015. The vertical transect across the two ridges shows distinct flow patterns, such as the speed up of the wind velocity during

daytime over the second ridge, as well as horizontally-repetitive standing wave patterns during early morning hours that are following the topography with half of its wave length. Closer analysis shows that wind at lower levels is deviated through the valley structure. In the case reported, with a south-westerly mean wind direction, wind between the two ridges was deflected towards the north-west exit.
These observations imply a highly three-dimensional flow over the ridges with a variety of flow patterns, depending on wind direction and atmospheric stratification, that might influence the interaction between the inflow and the WEC as well as its wake structure.

5.2 The WEC

Rotor Diameter	82 m
Rated Power	2000 kW
Hub Height	78 m
Rated Wind-Speed	13 ms^{-1}
Cut-In Wind Speed	2 ms^{-1}
Cut-Out Wind Speed	28 ms^{-1} to 34 ms^{-1}
Rotational Speed	6 rpm to 18 rpm

Table 5.1 – *Technical data of the Enercon E-82 E2/*2000 kW *wind turbine installed in Perdigão, Portugal.*

The WEC of type Enercon E-82 E2 is situated on the SW ridge at latitude 39°42′25.9″N and longitude 7°44′41.4″W. Its tower base will be the center of the coordinate system used throughout the rest of this work.
The E-82 E2 with a rated power of 2000 kW is a horizontal axis wind turbine with three rotor blades turning clockwise. Turbine hub height is at $h_{\mathrm{hub}} = 78\,\mathrm{m}$ and the rotor diameter is $D = 82\,\mathrm{m}$. The hub is able to successively follow the main wind direction and the blades can be individually pitched depending upon wind conditions.
The WEC cut-in and cut-out wind speed is $2\,\mathrm{ms}^{-1}$ and $28\,\mathrm{ms}^{-1}$ to $34\,\mathrm{ms}^{-1}$, respectively, reaching the maximum power output at a rated wind speed of $13\,\mathrm{ms}^{-1}$ (see Tab. 5.1). A specialty of Enercon WECs is the gearless power transmission chain to convert the energy extracted from the wind into electricity (Enercon, 2017).

5.3 The Setup

The three Lidar systems operated by the DLR, called DLR85, DLR86 and DLR89, were positioned as can be seen in Fig. 5.1. These positions were chosen to span a right handed coordinate system perpendicular to the ridges, so that for the main wind direction DLR85 and DLR86 were aligned with the WEC, DLR86 being situated in the valley, whereas DLR85 was positioned on the second mountain ridge. DLR89 on the other hand, was positioned along the WEC ridge, perpendicular to the main wind direction. However, Lidar systems' positions deviated slightly from an exact alignment with a coordinate system perpendicular to the ridges. The misalignment was caused by site specific restrictions, such as trees or lumps of rocks blocking the line of sight or hindering the access with heavy machines to deploy the Lidar systems. A sketch of the Lidar systems' positions in respect to an ideal, perpendicular coordinate system in respect to the ridges can be seen in Fig. 5.2. The x-axis is oriented to the north-east, the y-axis is pointed along the south-west ridge in north-west direction and the z-axis is denoting the vertical direction. The coordinate system's origin is the base of the WEC, which is positioned at $\mathbf{x}_{\mathrm{WEC}} = (0, 0, 0)$. It can be seen that DLR85 and DLR86 where both positioned slightly to the right of the x-axis including an angle of $\varepsilon_{DLR85} = 3.72°$ and $\varepsilon_{DLR86} = 4.17°$, respectively. DLR89 has an angle of $\varepsilon_{DLR89} = 4.94°$ with the y-axis.

To determine the deviations, the exact positions of the Lidar systems were measured with a Leica MultiStation MS50. The evaluated GPS coordinates were then transfered into the Portuguese coordinate system PT-TM06 (Tab. II.2) in which the deviation angles ε were calculated. Positions, in the turbine coordinate system, are listed in Tab. 5.2.

To be able to adjust scan patterns and scan directions, all Lidar systems needed to be leveled and aligned to North.

North was aligned with the indication of a field compass in a first step. To exactly identify the actual offset of the systems orientation towards north and the tilt in the horizontal plain, several meteorological masts where mapped through hard target scans. This method, called CNR mapping, allows an exact calculation of azimuth and elevation offsets.

Each Lidar system was calibrated against at least four meteorological masts. With a prior laser survey of mast positions and heights and the measured GPS positions of the Lidar systems, theoretical mast positions were determined and evaluated against the CNR mapping results. The final offsets were calculated as the mean

Lidar	X in [m]	Y in [m]	Z in [m]	ε in [°]	d in [m]
DLR85	1411.67	-91.71	-25.86	3.7172	1414.65
DLR86	1000.91	-73.01	-160.88	4.1717	1003.57
DLR89	25.62	296.35	-3.90	4.9411	297.46
WEC	0	0	0	-	-

Table 5.2 – *Lidar systems' positions in the WEC coordinate system*

of the individual differences between theoretical and measured values. Offsets for each Lidar system throughout the campaign are listed in Tab. II.4 and the initial offsets for every system and their standard deviation in Tab. II.3.

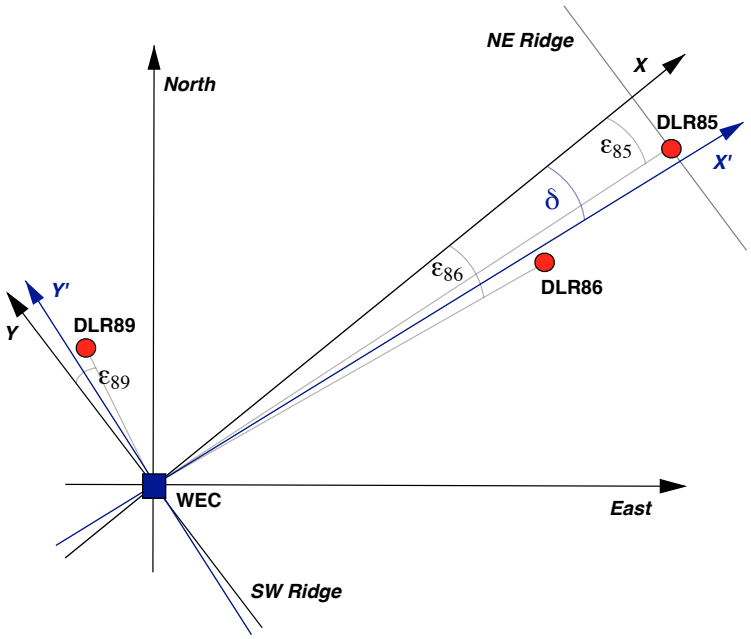

Figure 5.2 – *Sketch of Lidar systems' positions in the North/East GPS coordinate system and the ridge coordinate system.*

5.4 Measurement Scenarios

With the positioning described in Chapt. 5.3, various measurement scenarios to characterize the air flow over the two parallel ridges and the valley, as well as the flow interaction with the WEC, could be executed. Single line of sight measurements as well as complex trajectory scans with synchronized measurements, to resolve the three-dimensional wind vector at specific points, were performed.
The most common measurement scenario performed was a CS through the valley

transect, cutting the turbine wake vertically. This scan pattern consists of two parallel RHI scans performed by DLR85 and DLR86. Both systems scanned with an azimuth angle of $\theta = 236.9°$. The azimuth was chosen so that the wind turbine would be centered between the two parallel vertical planes spanned by the RHI scans. DLR85 is slightly measuring to the right of the WEC, whereas the laser beam of DLR86 is passing the WEC on the left hand side. This means that the RHI planes spanned by the laser beams of DLR85 and DLR86 are heaving offsets of 4.51 m and −4.76 m in y direction in respect to the WEC center. The advantage of this set up is that the beam path is not blocked by the WEC tower, allowing to investigate the inflow on the other side of the WEC, too.
Throughout the rest of this work a coordinate system aligned with the coplanar scan direction of $\theta = 236.9°$ and therefore tilted by $\delta = 3.9°$ to the perpendicular coordinate system displayed in Fig. 5.2 will be used. The WEC is still situated at its origin and the x'-axis is pointing towards the north-east and the y'-axis is pointing towards the north-west. Wind speeds will be referred to as u,v and w accordingly, where w is the vertical wind speed along the z-axis. In this coordinate system the offsets of DLR85 and DLR86 in respect to the x'-axis will be neglected and the two systems are considered to be in line with the wind turbine. Therefore, coplanar wind speed calculations on the x'- and z-axis are done as if DLR85 and DLR86 are measuring in one plane and in line with the WEC. This is why the symmetric bypass of the WEC on either side is key, as both sides of the wake will be represented equally in the combined measurement. Positions used for the coplanar transect therefore are $\mathbf{x}_{\mathrm{DLR85}} = (1414, 0, -25.86)$ and $\mathbf{x}_{\mathrm{DLR86}} = (1003.57, 0, -160.88)$.

Scan parameters for DLR85 and DLR86 were adapted throughout the campaign in order to adapt to atmospheric backscatter conditions as well as phenomena expected to be measured. The pulse length was chose to be 100 ns for good atmospheric backscatter conditions and 200 ns for days with a lower backscatter signal. DLR85 measured within the range limits of 50 m and 3000 m and a range gate spacing between 10 m and 50 m. The minimum elevation angle was set to −8° and the maximum elevation angle to 100°. The azimuth angle was kept constant despite minor adjustments due to offset corrections.
DLR86 measured within the range of 50 m and 1400 m with a range gate spacing between 10 m and 25 m. The minimum elevation angle was 6° and the maximum elevation angle was 160°. The azimuth angle was held constant despite minor variations due to offset adjustments.

The angular resolution for DLR85 and DLR86 was chosen to be either 0.5° or 1° according to the results presented in Chapt. 4.4.
DLR89 performed either RHI scans or complex trajectory scans depending on the wind direction and flow phenomena expected. RHI scans are performed to cut the turbine wake at distances $d_1 = 95.77\,\mathrm{m} \approx 1\,\mathrm{D}$, $d_2 = 156.29\,\mathrm{m} \approx 2\,\mathrm{D}$ and $d_3 = 228.71\,\mathrm{m} \approx 3\,\mathrm{D}$. The complex trajectory scan, on the other hand, scans a straight line at turbine hub height across the valley cutting the CS plane. DLR89 therefore allows to characterize the wake position as well as the wind component in y' direction, meaning that the three-dimensional wind vector at the points intersecting with the CS plane can be calculated.
DLR89 measured in a range of 50 m to 990 m with a range gate spacing of 10 m. The minimum elevation angle was chosen to be $-2°$ and the maximum elevation angle was 50°. The angular resolution was 0.5° and the pulse width was chosen to be either 100 ns or 200 ns, depending on atmospheric conditions.
The parameters for the synchronized triple Doppler measurements will not be discussed here, as these measurements will not be part of the following data analysis. However, it is worth explaining the measurement strategy briefly, as it is a new approach to dynamically adjust the measurement points in order to increase the yield of good wake measurements. To be able to react to a change of the main wind direction, an adjustment of measurement point positions is done every 30 minutes. Measurement points are reallocated to the lee of the WEC according to changes in the main wind direction. The advantage to follow the wake propagation dynamically is therefore gained.

Chapter 6

Data

The dataset produced during the Perdigão 2017 field experiment is unique in its scope and of immense complexity. In the following chapter the two sub-datasets, which were collected to characterize the turbine wake, recorded by the three DLR Lidar systems and the Integrated Surface Flux System (ISFS), will be explained in detail.

6.1 Lidar Data

The three Leosphere Windcube 200S Lidar systems started operation on the 30th of April 2017 at 16:00 UTC and were shut down on the 16th of June 2017 at 10:00 UTC, totaling 1123 hours of measurement time. The data recorded added up to the order of one terabyte. Throughout this period, scanning scenarios were varied depending upon atmospheric conditions and phenomena expected to be measured, leading to minor gaps in the data acquisition of few minutes, by reason of the upload and restart of the systems. Apart from these minor time spans without data acquisition, several thunderstorms causing electricity grid break down, were another reason for data outages of several hours. After the campaign, acquired data was categorized by scanning scenario and the quality of recorded data. An availability for RHI measurements with good data quality, relevant for this thesis, of 78 % was calculated for DLR86 and DLR89. DLR85 on the other hand, only possesses an availability of 36 %. The big difference in availability between the individual systems was due to technical failure of the the DLR85's acquisition board. The malfunction led to a significant decrease in the CNR, generating compromised data, as the MLE method was not able to accurately determine the incoming pulse frequency and therefore the LOS velocity. After an unsuccessful try to fix this

technical issue in the field, with the support of the Leosphere customers' service, a position switch of the Lidar systems DLR85 and DLR89 was undertaken on the 3rd of June to optimize the measurements for the coplanar RHI scan scenario throughout the rest of the campaign. With this new setup DLR85 could further provide reasonable measurement results for the wake cut scenario, as the distance to the region of interest was reduced. For the sake of readability and because chosen analysis intervals are not affected by the position switch, the systems and their positions will be referred to as described in Chapt. 5.3.
To fit the scope of this work, the vast amount of measurement hours had to be narrowed down to an analyzable amount of time, within which the requisitions to measure wake structures were given. Therefore, three periods of four hours with clearly distinct ABL conditions and hourly main wind direction deviating no further than ± 15° from perpendicular inflow conditions were selected. Good availability for all three systems was presupposed. These requirements were met

- on the 9th of Mai 2017 in the time from 11:00 to 15:00 UTC for CBL conditions,
- on the 13th of Mai 2017 in the time from 10:00 to 14:00 UTC for NBL conditions,
- on the 22th of Mai 2017 in the time from 03:00 to 07:00 UTC for SBL conditions.

The scan parameters for each period are listed in Tab. 6.1.
For the selected periods, the raw data stored as text files on each Lidar system was converted into NetCDF format for a better work flow. In the same step, a quality control was applied to filter bad data. Data with a CNR smaller than −25 dB and greater than −5 dB was excluded from the analysis.

ABL	pulse length	FFT	physical resolution	angular speed	acc. time	angular resolution
convective	100 ns	64	25 m	1 °C/s	500 ms	0.5°
neutral	100 ns	64	25 m	1 °C/s	500 ms	0.5°
stable	100 ns	64	25 m	2 °C/s	500 ms	1°

Table 6.1 – *Lidar systems' scan parameters.*

6.2 Integrated Surface Flux System Data

The dataset acquired by the multiple meteorological masts was recorded by the American National Center for Atmospheric Research (NCAR) and is stored in the Earth Observing Laboratory (EOL) data archive (NCAR/EOL, 2017). This extensive dataset covers all measurements coming from all the sensors mounted on the 54 meteorological masts. For the purpose of this work, focus was set on various sonic anemometers mounted on meteorological masts TW20 and TW25 to determine wind speed and wind direction. Furthermore, temperature and pressure sensors to calculate the ABL conditions were also used, as will be described in Chapt. 7.1. The NCAR/EOL Preliminary 5 minute ISFS data features all measured data in the non tilt corrected instrument coordinates system, meaning that deviations from horizontal alignment and alignment to North are not automatically corrected. To calculate absolute wind speed and wind directions, the tilt angles that were determined by a laser survey, executed by the DTU, need to be taken into account. For the transformation between the sonic coordinate system and the meteorological coordinate system to calculate the wind direction in respect to true North the EOL convention is used:

$$\phi = tan^{-1}(\frac{-u_{\text{sonic}}}{-v_{\text{sonic}}}) + \Delta_\theta. \tag{6.1}$$

A positive u_{sonic} denotes the sonic wind component blowing towards East and v_{sonic} designates the sonic wind component blowing towards North, for a sonic anemometer positioned without any tilt towards North. Δ_θ denotes the azimuthal deviation of v_{sonic} in respect to true North.
The ISFS dataset provides the five minutes mean of high frequency measurements, limiting the temporal resolution of analysis to this time span.

6.3 Data Discussion

The mentioned datasets used to identify and characterize the interaction between ABL flow and the WEC impose certain limitations to the evaluation of the data. The most obvious infliction is caused by the temporal resolution of the ISFS data and the inability to resolve turbulent structures on timescales smaller than five minutes. Even though the timescale of the duration for one RHI sweep sets a lower limit to the temporal resolution of the flow field, further information coming from the ISFS dataset, like wind direction or absolute wind speed, necessary to interpret

the Lidar data, is not yet available, but will be made available one year after the campaign.
As a result it was decided to evaluate the ABL flow with a temporal resolution of five minutes. Furthermore, a five minute interval offers the advantage to conserve large scale flow phenomena while disposing small scale fluctuations of turbulent motion unimportant to the analysis.
As will be seen in Chapt. 7.1, only the absolute temperature can be calculated to make a statement about the ABL stratification. Nevertheless, this approximation should be sufficient to clearly distinguish between a SBL, CBL and NBL.
A crucial limitation to the evaluation of the data results from the fact that to date, when this work was finished, no Supervisory Control And Data Acquisition (SCADA) data from the WEC was available. This means that the exact position of the WEC hub could not be taken into account. Therefore, a work around strategy, which will be explained in Chapt. 8, had to be used to select periods of time when the WEC hub aligned parallel to the measurement plane of the CS. Missing out on the SCADA data is, however, very unfortunate as deviations of the wake propagation due to misalignment of the turbine hub to the main wind direction could not be detected. From visual inspection, the author got the feeling that the wind turbine hub tracking system was delayed in comparison to the change of the main wind direction. Hence, the analysis might exclude valuable time intervals as these situations could not be addressed upon objective criteria. Furthermore, effects like wake meandering caused by the misalignment of the turbine hub and the main wind direction had to be discarded from analysis, too.
Due to the missing SCADA data one had to suppose that the turbine hub is always aligned with the main wind direction in order to be able to select periods of time worthwhile investigating.

Chapter 7

Identification of WEC Wake in Complex Terrain

This chapter serves to show how WEC wake in complex terrain can be detected and describes the wake tracking algorithm used to follow the wake propagation in a turbulent ABL flow in detail. In a first step, however, the atmospheric stability in the time intervals mentioned above is identified. Then, as proof of concept, it is shown that a wake structure can be measured with the setup and the measurement strategy described in Chapt. 5.3. Then the main flow properties for each of the three selected ABL conditions are analyzed.

7.1 ABL stability Analysis

In order to calculate the ABL stability in the three measurement periods, the potential temperature is calculated. Data for this analysis is obtained from the meteorological tower TW20, which is situated on the wind turbine ridge (see Fig. 5.1). This meteorological mast is located about 210 m to the south-est of the WEC. Temperature sensors are deployed at 10 m, 20 m, 40 m, 78 m and 100 m above ground level covering the whole atmosphere up to hub height and above. For the three analysis periods, potential temperature profiles are calculated for every 30 min on behalf of the 5 min data.
According to Stull (2012) the potential temperature θ_T is defined as:

$$\theta_T \cong T + \frac{g}{C_p} z, \tag{7.1}$$

where T is the measured air temperature, $g/C_p = 0.0098\,\mathrm{K/m}$ the negative of

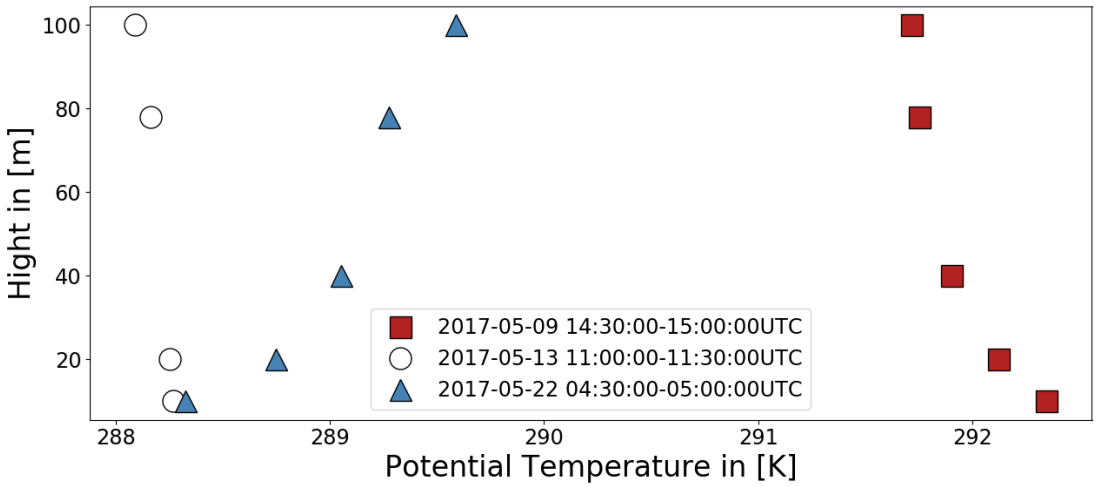

Figure 7.1 – *Exemplary potential temperature profiles from the three analysis periods. It can be see that θ_T increases with height for the measurement period on the 22nd of May, indicating a SBL. For the 13th of May, θ_T is nearly constant over the measurement range, indicating a NBL. The measurement temperatures on the 9th of May, on the other hand, are decreasing with height, indicating a CBL.*

the adiabatic lapse rate, with g being the gravitational acceleration and C_p the specific heat at constant pressure for air. z is the height above ground.
Figure 7.1 shows exemplary temperature profiles for each of the three measurement intervals. It can be seen that on the 9th of Mai θ_T decreases with height, indicating a CBL. On the 13th of Mai profiles are more vertical than the ones on the 9th of Mai and θ_T is nearly constant with height. This indicates a NBL, as the ABL is well mixed and no temperature gradients can be detected. However, a slight decrease of θ_T with height can be seen, causing the ABL not to be perfectly neutral. Contrary to this, the 22nd of Mai shows a positive laps rate of the potential temperature. The temperature gradient is positive, which means that air masses at greater heights are warmer than the ones at ground level leading to a very stable stratification of the ABL.

7.2 ABL Flow Field Over Complex Terrain

The ABL flow field for the three different stability cases are quite distinct and worth a detailed analysis to get a general understanding of the flow and its features. Therefore, the vector field for exemplary time intervals for each of the three cases is calculated.

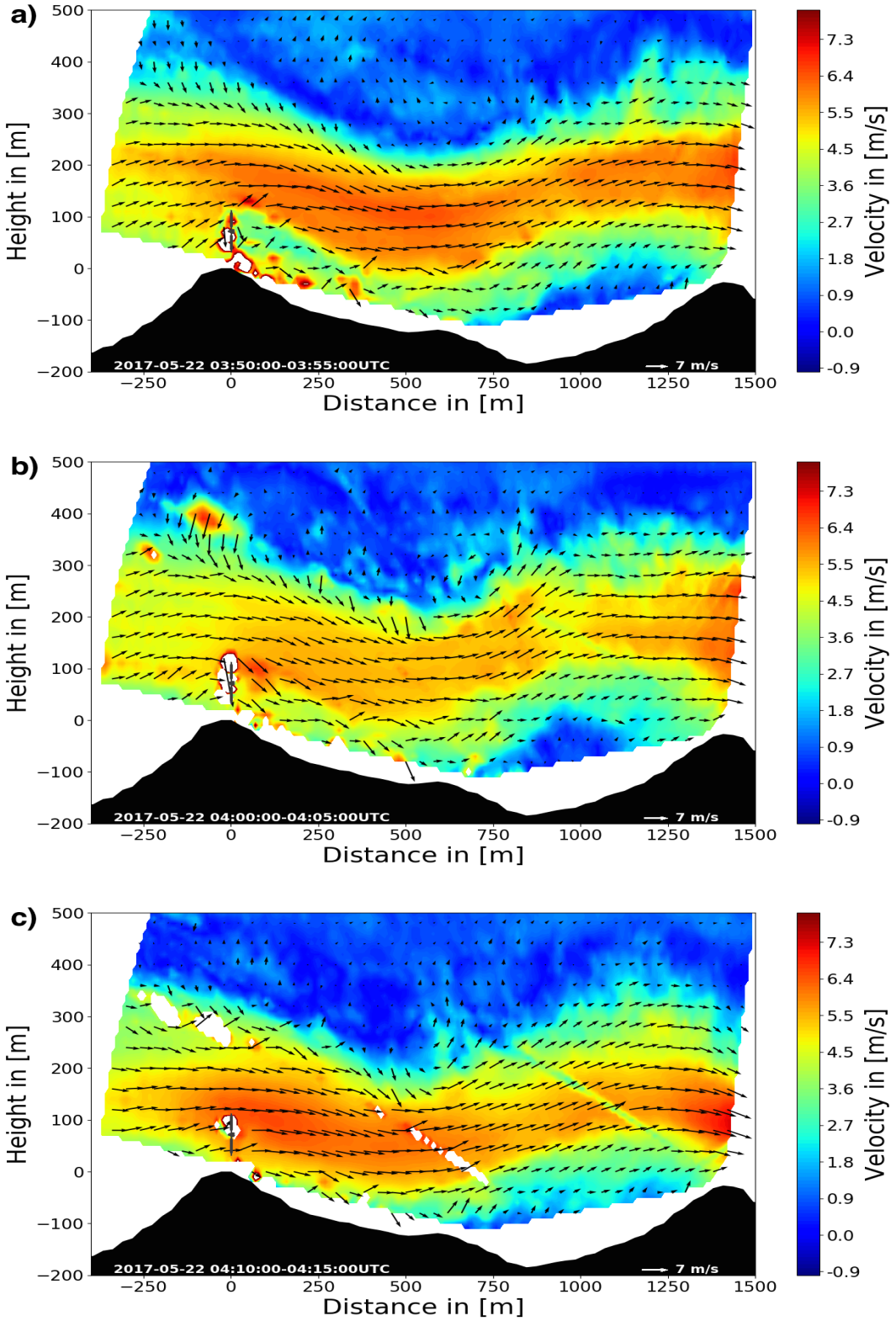

Figure 7.2 – *SBL flow field during the shut down of the WEC at 04:00 UTC on the 22nd of Mai 2017. The color scale decodes absolute velocity and the arrows denote the flow direction. The interaction between the WEC and the ABL can clearly be seen when the WEC is extracting energy (a). This interaction is decreasing (b) and finally vanishing (c), once the WEC is shut down.*

During the analysis period for the SBL condition, the fortunate incidence that the WEC was shut down during 04:00 and 05:00 UTC, allows to compare the undisturbed flow field with the flow field where an interaction between ABL flow and WEC is taking place, which offers the opportunity to proof the measurement strategy.
Figure 7.2 shows the vector field before, while and after the wind turbine is shut down. A clear wake structure with lower wind speeds and more turbulent flow in the lee of the WEC can be seen in the first frame. At this time step the WEC is still running and extracts energy from the atmospheric flow. Once the WEC is shut down (second frame), the flow field needs some time to adjust to the new conditions. It is still possible to identify remains of the turbulence generated by the interaction of the rotating WEC blades with the flow, while the wind speed deficit is decreasing. Finally (third frame), the flow recovers from the wake effects and a homogeneous flow field evolves. The time evolution of the flow field in Fig. 7.2 clearly shows that a wake structure can be detected with the measurement strategy described above.
The vanishing wake behind the WEC is only one of the interesting features that can be observed during the SBL flow case.
Furthermore, layers of distinct wind speeds can be detected. A tube like feature with increased wind speeds, in comparison to the wind field above, with a vertical extension of 300 m can be witnessed above the ridges. The maximum wind speed is located at about 200 m above ground level. Banta et al. (2004) measured comparable flow features at the Great Salt Lake basin situated in central Utah with a Doppler Lidar system and classified them as Low Level Jets (LLJs). Even though the terrain complexity differs, one finds that height above ground, as well as vertical extension of the two studies are comparable. A LLJ detected with the 2 µm Doppler Lidar system by Käsler (2011) is less pronounced in vertical broadness, but maximum wind speed is located in the rotor plane of a WEC. All three cases locate jet occurrences in heights relevant to wind energy production, because the enhanced velocities are favorable for electricity generation. But higher vertical shear and an increase of turbulence in the SBL between the LLJ maximum and the surface, as found by Banta et al. (2006) and Banta et al. (2003) causes higher loads to the rotor. It is interesting to see that the LLJ follows the terrain and a wave structure with a wave length of the distance between the two mountain ridges evolves. Similar flow features have already been reported by Rodrigues et al. (2016).

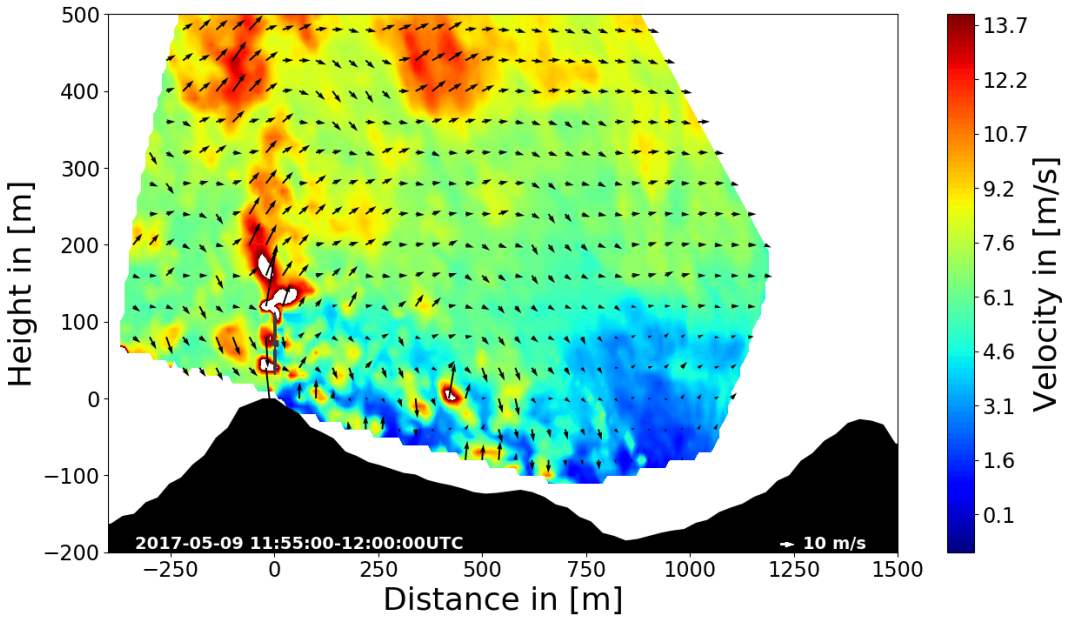

Figure 7.3 – *Exemplary measurement from 11:55 to 12:00 UTC for the CBL case on the 9th of Mai 2017. The color scale decodes absolute velocity and the arrows denote the flow direction.*

Another interesting flow feature that can be detected in the second picture of Fig. 7.2 is an area of recirculation, situated at the second wave peak at a height of about 300 m and 700 m downstream of the WEC.

An exemplary flow case during the convective measurement period, can be seen in Fig. 7.3. In comparison to the stable case, the flow is not horizontally stratified anymore. The mean velocity of 6 ms^{-1} is comparable to the wind speed maximum of the LLJ seen during the stable measurement period. All the same, it is very difficult to identify the wake structure that is lifted upwards behind the WEC. The overall turbulent structure of the flow and the flow separation, caused by the south-west ridge, complicates a clear identification of a wake structure (Barthelmie et al., 2003). We can identify regions of up- and downdraft and see that upward movements are associated to higher wind speeds. These larger structures moving upwards are caused by the incident solar radiation causing air packages to heat up and finally lift from the ground.

Figure 7.4 shows the velocity field for the neutral flow case. A more homogeneous wind speed distribution than in the cases before can be recognized. We are able to identify a region of lower wind speed behind the WEC, which is the wake. But, as

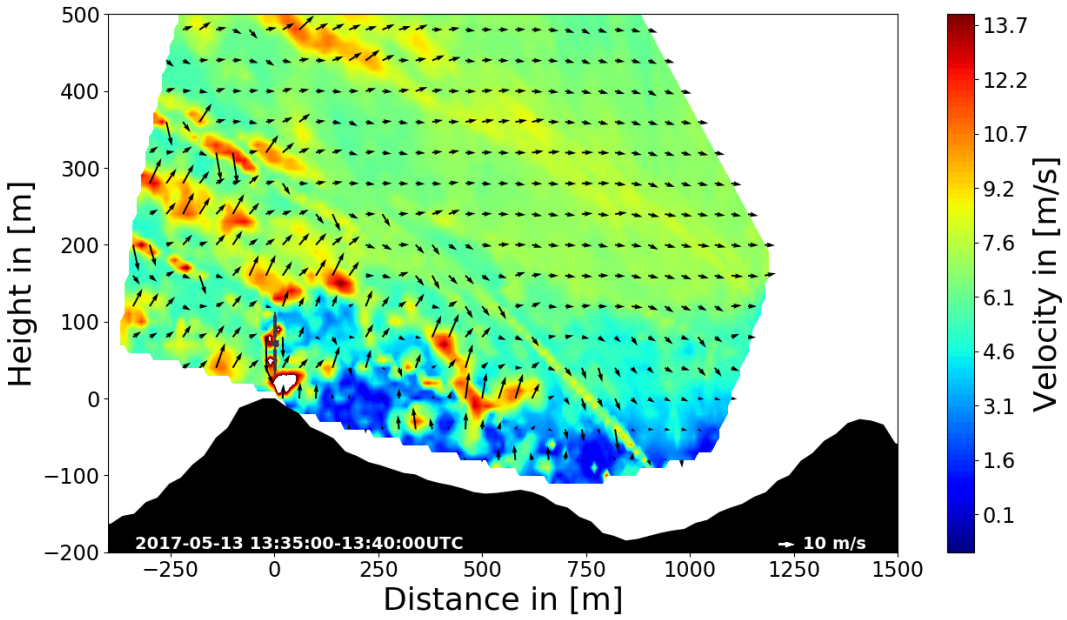

Figure 7.4 – *Exemplary measurement from 13:35 to 13:40 UTC for the NBL case on the 13th of Mai 2017. The color scale decodes absolute velocity and the arrows denote the flow direction.*

in the convective case, the flow separation caused by the ridge complicates an easy distinction between wake effects caused by the WEC and the mountain ridge.

7.3 Wake-tracking Algorithm

As could be seen seen in the chapter above, ABL flow in complex terrain can exhibit very complex flow structures. This complexity makes it very difficult to distinguish between flow phenomena induced by the terrain and flow features caused by the interaction between the ABL flow and the WEC. To detect the wake structure, an approach, inspired by Hirth and Schroeder (2013), to follow the wake center was therefore decided on. This strategy will later on drastically decrease the complexity to apply the methodology for the CS scenario, already introduced in Chapt. 4.2, and improve fitting results. Hence, an algorithm to automatically track the wake propagation in the CS plane had to be developed. To do so, one builds upon the assumption that the wake propagates downstream smoothly. To be more precise, the wind speed deficit decays gradually and continuously in a way so that abrupt variations in wind speed at the wake center can be excluded and an increase of velocity further downstream the WEC can be presumed. For this analysis the horizontal wind speed component u was used, as already proposed in Chapt. 4.2.

In a first step, five minute intervals in the dataset with main wind direction not deviating further than ±10° from the CS plane were selected. This pre-selection is done to exclude cases where the wake is outside the CS plane, as one expects a propagation with the main wind direction. To account for the possibility that the turbine hub's azimuthal position lags behind or turns in advance to the selected time interval, scans right before and after the originally identified interval are also considered.
For all these cases a wake tracking algorithm is applied to follow the wake propagation in an iterative approach by using a center of gravity method.

Center of Gravity Method

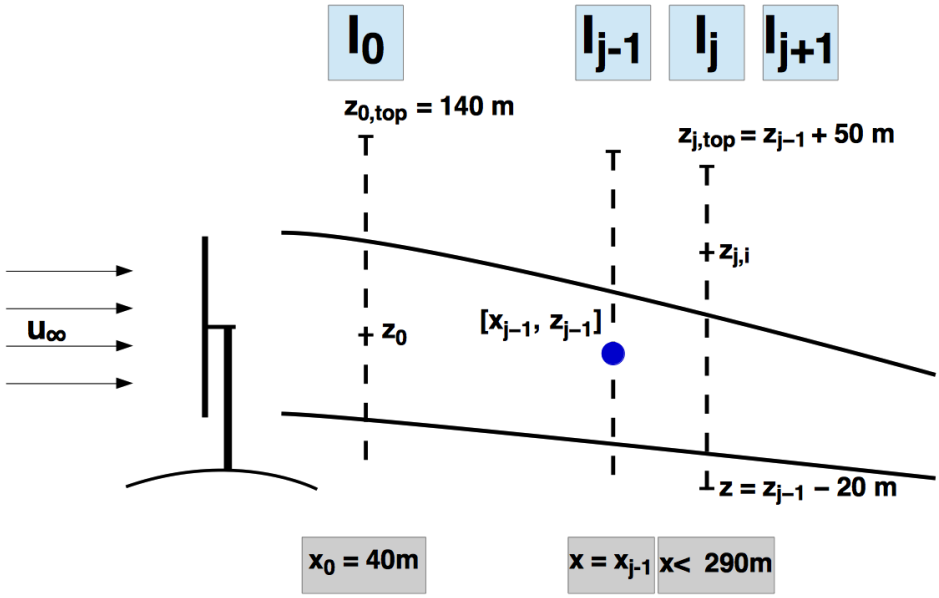

Figure 7.5 – *Sketch to visualize the wake tracking variables. I_0 is the first velocity interval used to determine the initial point to start the iteration to detect the wake propagation. I_{j-1},Ij and I_{j+1} represent three consecutive velocity intervals. The blue dot in I_{j-1} shows the already determined position $[x_{j-1}, z_{j-1}]$ of the wake gravity center for the iteration step $j-1$, which is used to define I_j in order to calculate the wake gravity center $[x_j, z_j]$ (compare to Fig. 7.6). I_{j+1} will then be determined in the following iteration step.*

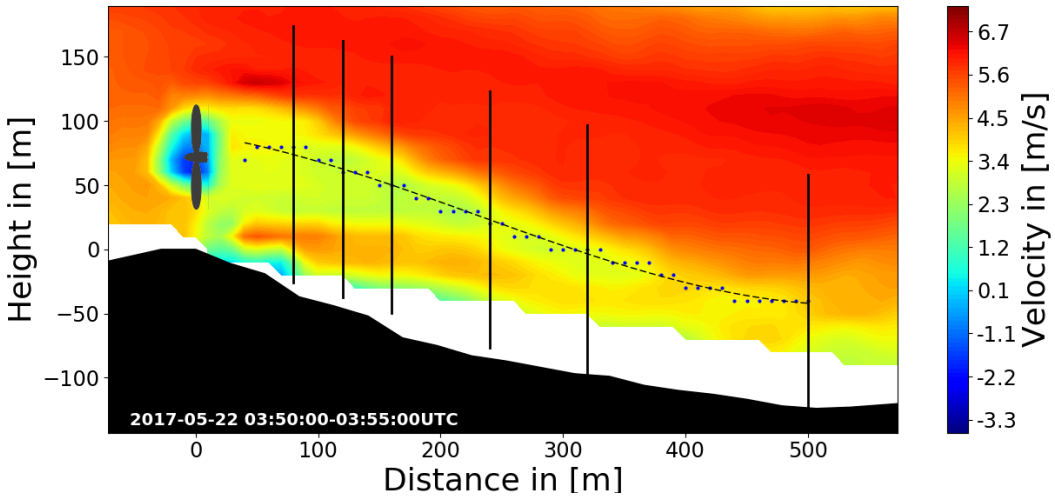

Figure 7.6 – *Exemplary wake case for a SBL on the 22nd of May 2017 at 03:50 until 03:55 UTC, to demonstrate the wake tracking algorithm. The blue dots show the position of the evaluated wake gravity centers as found with the center of gravity method. The dashed, horizontal black line illustrates the wake center line fitted with a cubic function. The black, vertical lines present five exemplary vertical transects at* 80 m*,* 120 m*,* 160 m*,* 240 m*,* 320 m *and* 500 m *behind the WEC.*

It is supposed that in the selected time intervals a wake structure can be detected and the wake gravity center height z_0 at a distance $x_0 = 40\,\mathrm{m}$ downstream the WEC as the initial point for the iterative procedure is determined. The distance of $40\,\mathrm{m} \approx 0.5\,\mathrm{D}$ is chosen as the closest distance to the WEC, as data points closer to the WEC are often corrupted by hard target reflections of the laser beam at the rotor blades.

The velocity of the undisturbed incoming flow field in front of the WEC u_∞, which one needs to determine the velocity deficit and which will be used for the center of gravity method, is defined by the Lidar measurements to be the average over 30 m centered around hub height $h_{\mathrm{hub}} = 78\,\mathrm{m}$, at a distance of $160\,\mathrm{m} \approx 2\,\mathrm{D}$ in front of the WEC, in accordance with Käsler (2011).

It is now possible to calculate the wake gravity center position z_0 for the vertical interval I_0, positioned at x_0, stretching from $z = 40\,\mathrm{m}$ to $z_{0,\mathrm{top}} = 140\,\mathrm{m}$, basically covering the whole rotor extension, in the following way:

$$z_0 = z_{0,\mathrm{top}} - \frac{1}{u_{0,\mathrm{tot}}} \sum_{i=1}^{n} d_{0\mathrm{i}} u_{0\mathrm{i,diff}}, \quad \text{with} \quad u_{0,\mathrm{tot}} = \sum_{i=1}^{n} u_{0\mathrm{i,diff}}, \quad n = 1, .., 10. \tag{7.2}$$

$u_{0\mathrm{i,diff}} = u_\infty - u_{0\mathrm{i}}$ designates the velocity difference between the undisturbed flow and the velocity behind the WEC at height $z_{0\mathrm{i}}$. $d_{0\mathrm{i}} = z_{0,\mathrm{top}} - z_{0\mathrm{i}}$ is the distance between the grid point positioned at $z_{0\mathrm{i}}$ and the top of the vertical transect $z_{0,\mathrm{top}}$. The index 'i' denotes the individual grid point positioned on the vertical interval. From the starting point $[x_0, z_0]$ one moves, for each iteration j, to the point $[x_j, z_j] = [x_{\mathrm{j}-1} + 10\,\mathrm{m}, z_{\mathrm{j}-1}]$. The vertical interval I_j, at position x_j, is then defined to stretch from $z_{\mathrm{j,top}} = z_{\mathrm{j}-1} + 50\,\mathrm{m}$ to $z = z_{\mathrm{j}-1} - 20\,\mathrm{m}$ for $x_j \leqslant 290\,\mathrm{m}$. For $x_j > 290\,\mathrm{m}$, I_j stretches from $z_{\mathrm{j,top}} = z_{\mathrm{j}-1} + 50\,\mathrm{m}$ to $z = z_{\mathrm{j}-1} - 10\,\mathrm{m}$. Equation 7.2 now reads:

$$\begin{aligned} z_j &= z_{\mathrm{j,top}} - \frac{1}{u_{\mathrm{j,tot}}} \sum_{i=1}^{n} d_{\mathrm{ji}} u_{\mathrm{ji,diff}}, \\ \text{with} \quad u_{\mathrm{j,tot}} &= \sum_{i=1}^{n} u_{\mathrm{ji,diff}}, \quad \begin{cases} n = 1, .., 7, & \text{if } x_j \leqslant 290\,\mathrm{m} \\ n = 1, .., 6, & \text{if } x_j > 290\,\mathrm{m}. \end{cases} \end{aligned} \tag{7.3}$$

Equation 7.3 yields a new wake gravity center height z_j, so that it is possible to move, from the newly determined wake gravity center $[x_j, z_j]$, to the next iteration step $j+1$. A sketch to visualize the wake tracking algorithm variables can be found in Fig. 7.5.

The unsymmetrical height distribution in order to evaluate the center of gravity for the vertical interval I_j for $j > 0$, is needed because of the slipstream induced by the mountain ridge. Velocities in the ridge's lee are always smaller than the free mean velocity of the flow field, causing errors in the center of gravity estimations when included into the weighting method, causing the wake gravity center to be detected at lower heights. It is therefore necessary to carefully limit the possibility that measurement points which are not part of the wake structure are taken into account when calculating the wake gravity center.

One can justify the antisymmetric distribution when looking at typical wake cases studied in this thesis. Typically, wake structures subducting into the valley are descending slowly, whereas wake cases rising above turbine hub height ascend rapidly. A more sensitive weighting method towards lower heights is therefore still able to follow wake propagation without jeopardizing the center of gravity estimation. Figure 7.6 shows one such case for the SBL. The detected wake gravity center points for each iteration step are displayed as small blue dots in the velocity deficit behind the WEC.

In order to only include measurement points that are associated to the wake structure into the center of gravity method, negative velocity differences, $u_{\mathrm{ji,diff}} < 0$,

are excluded as these values indicate a greater flow velocity downstream the WEC than upstream, therefore not being part of the wake structure.

Exit Conditions

The iteration continues until the following exit conditions are met:

- VD $< 10\,\%$
- for $x_j > 290\,\mathrm{m}$: if $u_{\mathrm{mean}} < u_{\mathrm{min}}$

Once the velocity deficit, as defined in Eq. 2.26, is smaller than $10\,\%$ iteration is aborted. This criteria is ranked the strongest to initiate abortion. As long as the VD is greater than $10\,\%$ it is additionally checked for distances greater than $290\,\mathrm{m}$ if the average velocity u_{mean} over $30\,\mathrm{m}$, centered around the wake gravity center, is greater than the minimum wake gravity center velocity u_{min} in the first $290\,\mathrm{m}$. This abortion criteria needs to be taken into account, to guarantee that the algorithm is following a flow structure that is dissipating and therefore decreasing in its velocity deficit.

Wake Profile Fitting

As a next step, a straight line is fitted through the wake gravity center points $[x_j, z_j]$ for wake cases shorter than $290\,\mathrm{m}$ and a cubic function for wake cases stretching further than $290\,\mathrm{m}$ (see dashed line in Fig. 7.6). With this approach it is possible to smooth out the iterative steps in order to account for the continuous evolution of the wake structure. Around this wake gravity center line vertical transects T_j with a height of $200\,\mathrm{m}$ are defined, onto which the velocities are interpolated linearly for every meter. Horizontal spacing between the transects is $10\,\mathrm{m}$. In Fig. 7.6, five such vertical transects are illustrated for demonstration purposes as black vertical lines. The cross sections T_j, giving the vertical velocity profile through the wake, are then further evaluated with the fitting procedure already introduced in Chapt. 4.2. Figure 7.7 shows the vertical velocity profiles from the exemplary transects of Fig. 7.6 that are positioned at $80\,\mathrm{m}$, $120\,\mathrm{m}$, $160\,\mathrm{m}$, $320\,\mathrm{m}$ and $500\,\mathrm{m}$ downstream the WEC. It can clearly be seen that the wind speed deficit in the near wake region exhibits a double Gauss structure that merges into a single Gaussian deficit profile with distance. The markedness of the velocity deficit vanishes the further one moves away from the WEC until nearly no deficit can be detected at

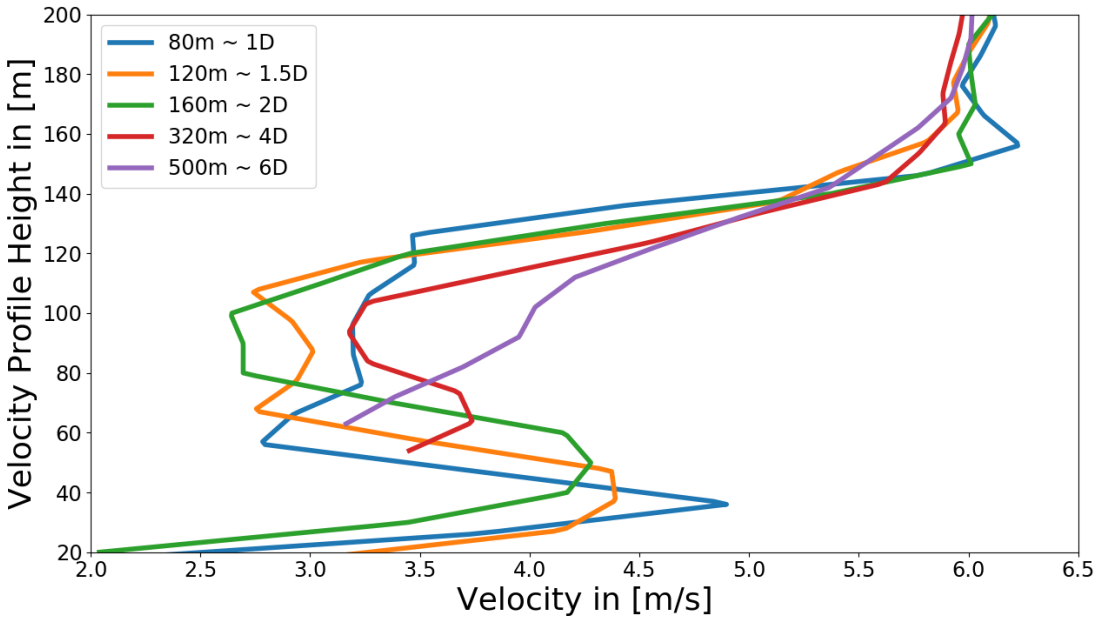

Figure 7.7 – *Five exemplary vertical velocity profiles, at* 80 m *(blue),* 120 m *(orange),* 160 m *(green),* 320 m *(red) and* 500 m *(purple), are plotted to show the evolution of the velocity deficit while moving away from the WEC. Positions of the transects can be seen in Fig. 7.6.*

500 m downstream the WEC anymore.

To fit the Gaussian models, introduced in Chapt. 4, however, an adjustment had to be done, as an undisturbed wind profile could not be subtracted from the vertical profiles due to the complex inflow. A detrended velocity profile is consequently not available. Model_1 (Eq. 4.4) and Model_2 (Eq. 4.5) were therefore adjusted, so that they feature a superposition of a logarithmic wind profile with a Gaussian or double Gaussian function, respectively:

$$\text{Model}_1^{'}: \; u(z) = A_{\log} ln(b_{\log} z + c) - A \cdot e^{\left(-\frac{(z-b_{\text{gauss}})^2}{2\sigma^2}\right)} + d; \tag{7.4}$$

$$\text{Model}_2^{'}: \; u(z) = A_{\log} ln(b_{\log} z + c) - A[e^{\left(-\frac{(z-b_{\text{upper}})^2}{2\sigma^2}\right)} + e^{\left(-\frac{(z-b_{\text{lower}})^2}{2\sigma^2}\right)}] + d. \tag{7.5}$$

Figure 7.8 shows the fits of $\text{Model}_1^{'}$ and $\text{Model}_2^{'}$ to the vertical velocity profile at 120 m behind the WEC for the wake case displayed in Fig. 7.6. The original, interpolated vertical profile can also be seen in blue. It is clear that in this case $\text{Model}_2^{'}$ fits the wake structure better, as the double Gaussian velocity deficit is still very pronounced.

Additionally, a third model, namely a logarithmic model, is introduced into the methodology, in order to detect the end of the wake structure in case the exit

conditions mentioned before would fail:

$$\text{Model}_3 : \; u(z) = A_{\log} \cdot ln(b_{\log} z + c) \tag{7.6}$$

These three new models are then used to carry out the missing steps in order to determine the wake parameters for each vertical wind profile T_j.
Model_3 is used as a further control parameter to ensure that the wake finding algorithm stops when no further wake can be detected, even though the exit conditions introduced before are not met. Restrictions to guarantee certain physical wake properties to the two Gaussian models are applied:

- fits with wake widths smaller than 30 m and greater than two rotor diameters (164 m) are excluded;
- propagation continuity is controlled by checking if the wake center from one analysis step to the next 'jumps' more than 20 m up or down.

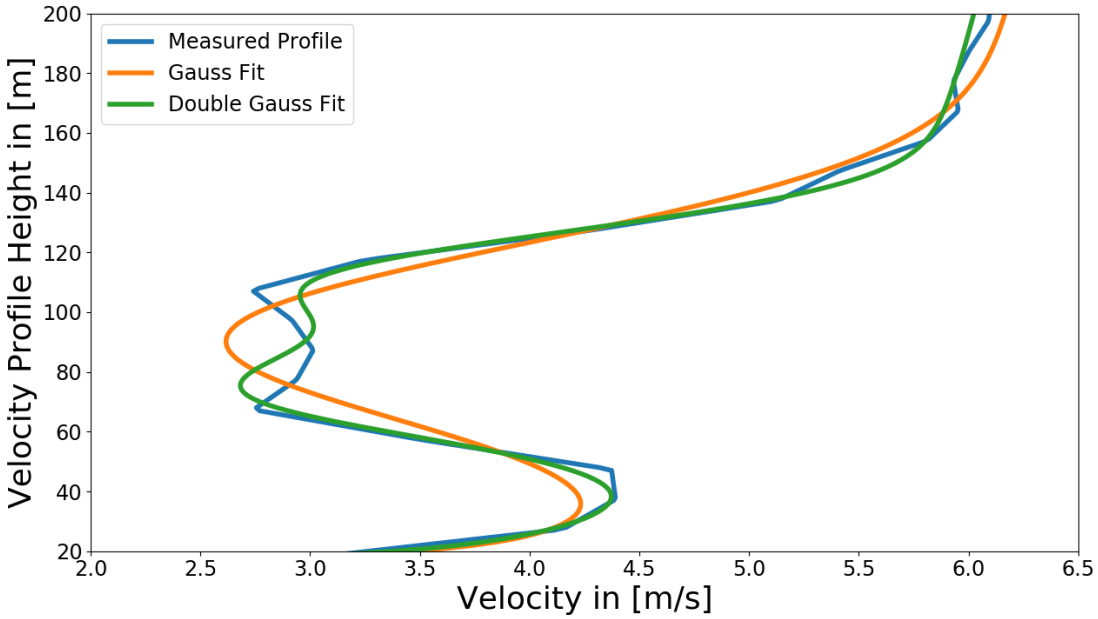

Figure 7.8 – *The velocity profile at* 120 m *behind the WEC (blue) is fitted with the two models presented for the superposition of a Gaussian (orange) or a double Gaussian (green) function with a logarithmic velocity profile, respectively. The velocity profile at* 120 m *is taken from the wake case illustrated in Fig. 7.6.*

If these requirements are not met for the model selected by means of the F-Test, the less complex model is chosen. If the physical criteria is still not met and the best model to fit the vertical profile is Model_3 or no fit is possible at all, the profile is excluded from analysis.
If, in sum, more than three vertical profiles are excluded from analysis or logarithmic profiles were chosen by the F-Test to be the best fit, analysis for transects located further downstream is aborted, as it has to be assumed that the wake tracking algorithm did not detect the end of the wake structure.
These checks guarantee a good quality for the wake fits and their physical consistency.

Chapter 8

Characterization of Turbine Wake in Complex Terrain

In this chapter results found with the wake-tracking algorithm described in the previous chapter, will be presented and compared to measurements from other field campaigns in state-of-the-art literature.

8.1 Wake Propagation

Figure 8.1 shows the wake center position, as the wake propagates downstream for each of the three measurement periods. In SBL conditions (blue triangles), wake structures can be detected up to several hundred meters behind the WEC. The longest wake case extends 760 m downstream, which corresponds to more than 9.2 D. It is interesting to see that most SBL wake cases descend into the valley. Only few maintain their position at hub height. In comparison, wake cases in the NBL and CBL are lifted above hub height. Their extension only reaches a little further than 300 m $\approx$ 3.7 D, with some of the neutral wake cases being slightly longer.
During night times, comparable wake lengths to the cases in the SBL were measured by Käsler et al. (2010), more than 9 D, and Smalikho et al. (2013) with a recorded wake case as long as 11.7 D. What is more, Smalikho et al. (2013) found that the mean wake propagation difference between night and day time scales with the factor two. In our case this equation holds for the maximum wake cases detected. The wake lengths in NBL and CBL conditions coincide with measurements from Smalikho et al. (2013) during day time (mean wake length of 340 m $\approx$ 3.4 D). The faster recovery of the wake in the CBL in comparison to a NBL was also observed

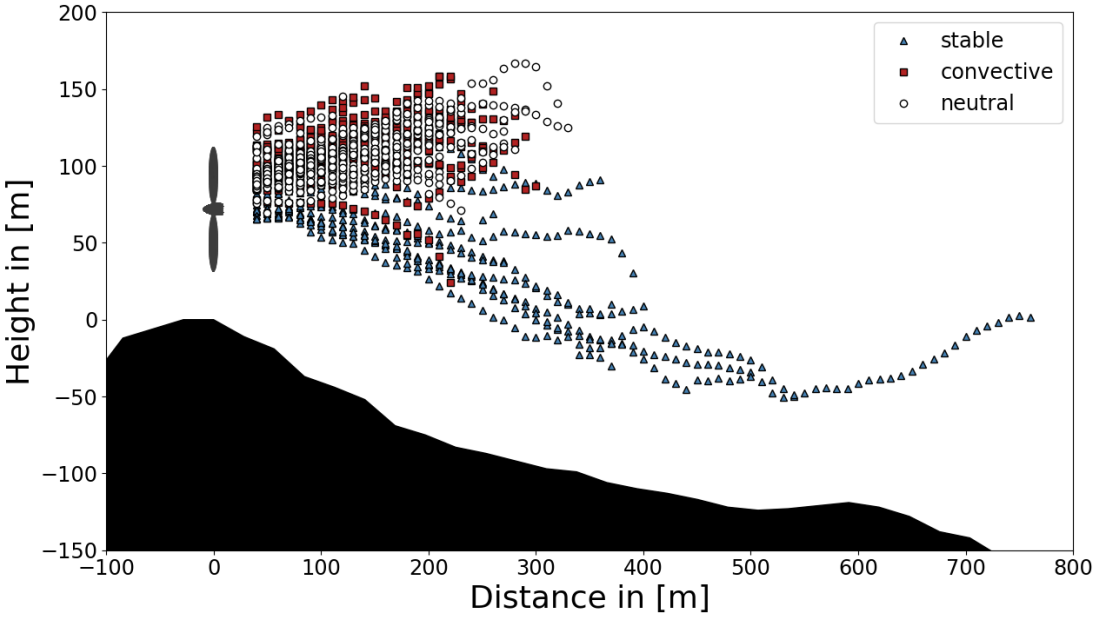

Figure 8.1 – *Wake centerlines for each analyzed wake case. The wake propagates into the valley for SBL conditions (blue triangles) and seems to be lifted for a CBL (red squares). In a neutral regime (white circles) the wake stays at hub height. Wake extension is the longest for stable conditions and shortest for a NBL.*

by Iungo and Porté-Agel (2014). In comparison to the studies mentioned above, where the wake is staying at the level of hub height, wake centers are lifted behind the WEC in the present study.

The deviation from hub height can be seen even more clearly, when looking at the mean propagation paths for each ABL regime. Figure 8.2 shows the mean wake center positions (solid lines) for all distances where at least three wake cases could be detected as well as their standard deviation (shaded region). The ascending wake center for the NBL and CBL regime can be associated to the positive vertical wind component of the free flow, as the mean wind has to cross the ridges. In addition, in the case of the CBL a wider scattering with distance of the wake center paths can be seen, which can be associated to the large turbulent structures that could be seen in Fig. 7.3. The scattering in the SBL case can be associated to the changes of the LLJ, as its height and intensity as well the wave length of its undulation changes throughout the measurement period.

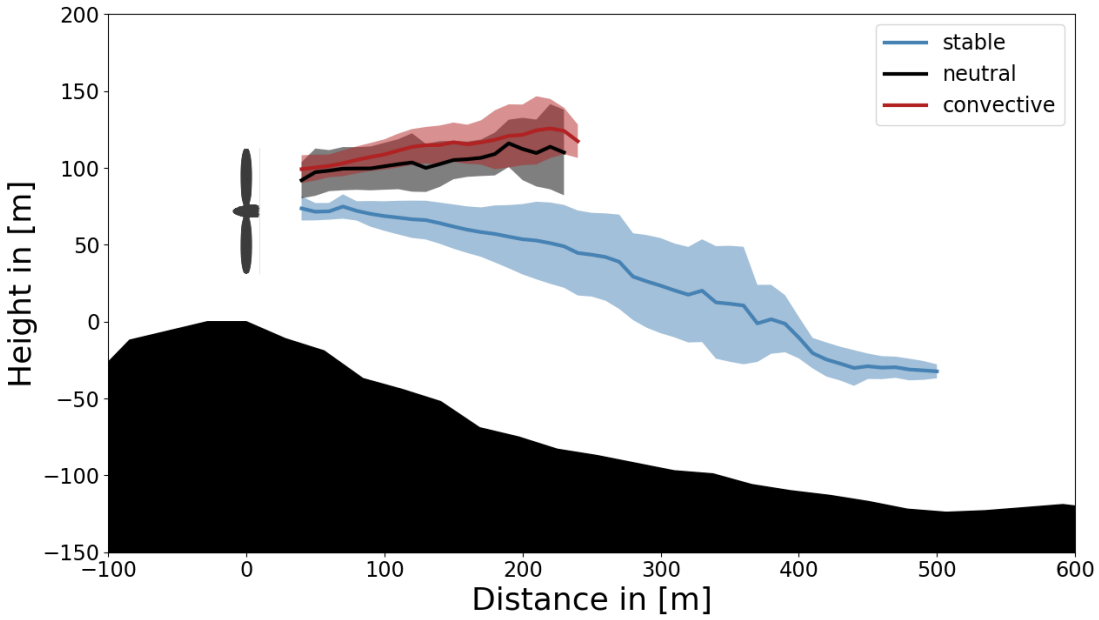

Figure 8.2 – *Mean wake center propagation paths (solid lines) for all distances where at least three wake cases could be detected together with their standard deviation (shaded region). The three ABL conditions are: stable (blue), convective (red), neutral (black).*

8.2 Velocity Deficit in Respect to Distance to the WEC

Figure 8.3 shows the VD for the three different ABL conditions and their standard deviation for all distances behind the WEC where at least three wake cases could be detected. The mean (yellow) is calculated from the wake cases of the three individual ABL conditions with at least two different regimes contributing. It can be seen that the mean VD decreases from 48 % at 60 m to 25 % at 250 m. It then again rises slightly, due to the influence of the SBL. In general it can be said that the VD for the SBL case decreases more slowly, from 47 % at 50 m to 23 % at 500 m and can be detected further away from the WEC than the VD of the two other ABL cases. Results coincide with the findings of Aitken et al. (2014), who measured a velocity deficit of 50 % at 1 D behind the WEC for wind speeds smaller than the ones necessary for the WEC to work at rated power. This coincides with the situation investigated in this study. Hirth and Schroeder (2013) found velocity deficits in the range of 40 % one rotor diameter behind the WEC, with wind speeds ranging from 8.5 ms^{-1} to 11.3 ms^{-1}. The measured mean VD of 46 % at 80 m $\approx$ 1 D behind the WEC therefore lies well within these boundaries.

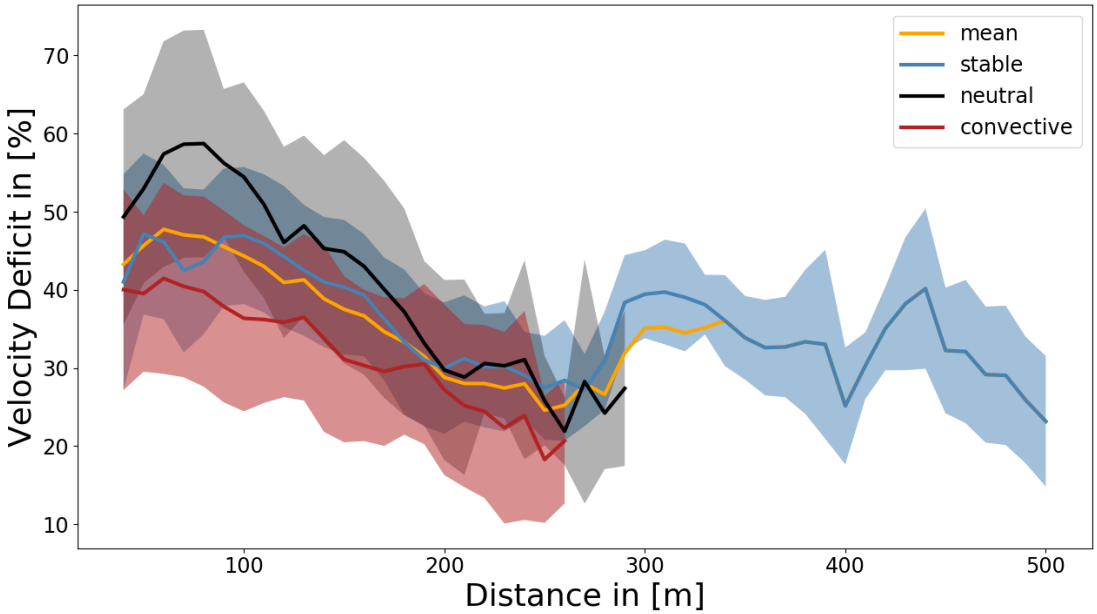

Figure 8.3 – VD *for all three ABL regimes and their standard deviation at distances where at least three wake cases were detected. The mean* VD *for all three ABL conditions (yellow) decreases with distances up to* 250 m *behind the WEC. The CBL (red) exhibits the lowest* VD*, whereas the NBL (black) possesses the highest* VD*. The* VD *for the SBL (blue) extends the longest.*

The qualitative evolution of the VD concur with the results found by Aitken et al. (2014) as well as Hirth and Schroeder (2013). However, the VD measured at 6 D in these studies is found to be about 30 % and therefore higher than the velocity deficit measured during the investigated periods in this study. Hirth and Schroeder (2013) measured a VD of 23.5 % at 7 D. On the other hand, Käsler et al. (2010) measured a VD of 20 % at 6 D during night times, and Barthelmie et al. (2003) measured a VD of 19 % at distances from 6.5 D to 7 D at an offshore location. These results better reflect the measured values of the study at hand, as ABL conditions are more likely to be similar.

The observations presented in Fig. 8.3 therefore are well within the scope of recent measurements of WEC velocity deficits despite the greater terrain complexity.

In the first 300 m a clear difference of the magnitude and the rate of decrease of the VD for the three different ABL conditions can be observed. The NBL possesses the greatest VD, with a maximum of 59 % at 80 m, and decreases the fastest. The VD for the SBL and finally the CBL, with a VD of 42 % at 60 m, follow. The same hierarchy of magnitude for the VD in the cases of the SBL and the CBL was found by Aitken et al. (2014), who distinguishes between a stable and an instable ABL.

In this context it is interesting to see that the VD for a NBL is the greatest, which would mean that in NBL conditions the greatest amount of energy can be extracted from the flow by the WEC, as the VD can be seen as a simple approximation for the efficiency of a WEC (compare Eq. 2.15).
The standard deviations of the VD for both, the NBL and the CBL regimes, are greater than for the SBL regime. A possible explanation would be the increased turbulence due to the convective motion of the free flow and the friction induced by the topography.
In a further step we will decompose the mean VD into velocity bins to be able to compare the wake models introduced in Chapt. 2.2.2 to the measurements.
Figure 8.4 shows the VD for the individual wake cases (triangles, circles and squares respectively for SBL, NBL and CBL conditions), as well as the mean of the measurements and the results for the Jensen-Park and the Frandsen model for an inflow velocity $u_\infty = 5\,\mathrm{ms}^{-1}$, plotted against the distance to the WEC.
It can clearly be seen that the velocity deficit diminishes with distance to the WEC from a maximum of 56 % at a distance of 90 m to 20 % at a distance of 500 m $\approx$ 6 D. Furthermore, it can be seen that the longer wake cases solely correspond to wake events in the SBL.
All models underestimate the VD over the whole distance systematically. Even though, for distances greater than 250 m $\approx$ 3 D, the qualitative decline seems to be represented well by all models, yet an offset of at least 10 % persists. For distances closer to the WEC, the Jensen-Park model better reproduces the trend of the VD. The Frandsen model with constant $\alpha = 0.7$ seems to gain accuracy for distances greater than 500 m in comparison to the Jensen-Park model and is more accurate than the Frandsen model considering α based on the terrain influence parameter. In regard to the terrain influence parameter k, it is necessary to specify the roughness length z_0 used for the calculations. For the study on hand, a roughness length of $z_0 = 3.5\,\mathrm{m}$ was chosen, as proposed by Hansen (1993) for forested ridges with a height of 150 m to 200 m.
To further investigate the VD and its dependence on the inflow velocity and the ABL regime, Fig. I.2 shows the VD for an inflow velocity $u_\infty = 6\,\mathrm{ms}^{-1}$. In general, wake cases are not as long as in Fig. 8.4, due to the fact that no wake cases in the SBL for $u_\infty = 6\,\mathrm{ms}^{-1}$ could be registered. The VD decreases from 58 % at 90 m to 20 % at 340 m behind the WEC. The wake recovery happens much faster than in the previously analyzed velocity interval. One could consider the increased inflow velocity as the driving force behind this change. However, the difference of $1\,\mathrm{ms}^{-1}$

is not very likely to have such grave implications. It is more reasonable to assign the effect to the predominant atmospheric conditions, as seen before (see Fig. 8.2). Furthermore, it is found that the two models, while conserving the inability to correctly reproduce the VD at distances smaller than 3 D, simulate the recovery in the far wake better for NBL and CBL conditions, than for SBL conditions, which was expected as the models were developed for NBL conditions. The Jensen-Park as well as the Frandsen model with $\alpha = 0.7$ once more outperform the Frandsen model based on the terrain influence parameter k. The differences between models and measurement mean shrinks to no more than 5 % for distances greater than 3 D.

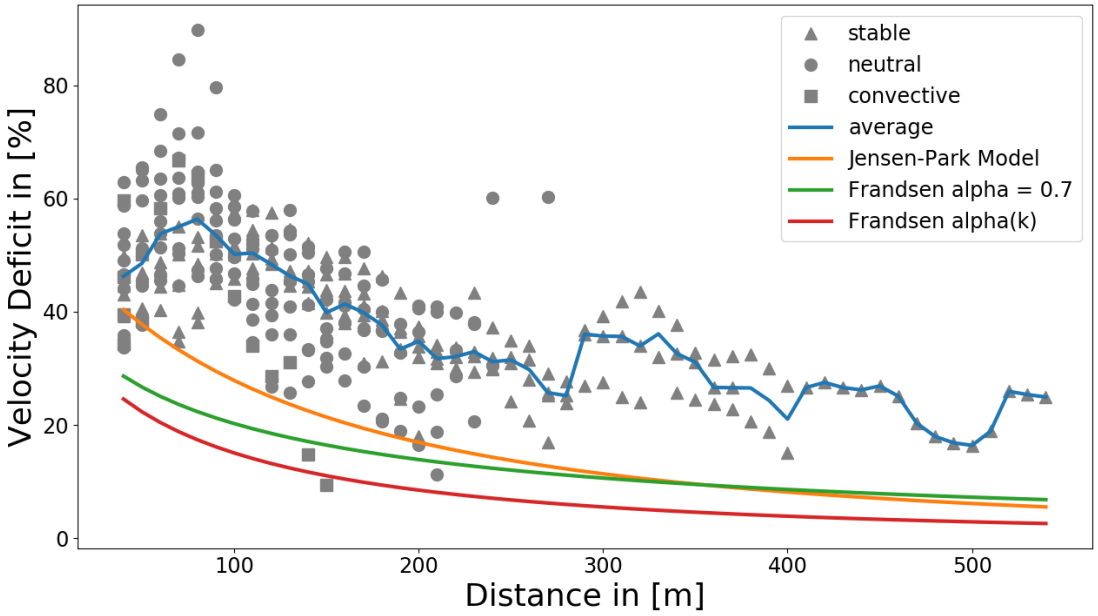

Figure 8.4 – VD *for wake cases at* $u_\infty = 5\,\mathrm{ms}^{-1}$ *plotted against the downstream distance to the WEC. The* VD *for each wake case (gray symbols) and the measured mean (blue) are compared to the Jensen-Park model (orange) and the Frandsen model with* $\alpha = 0.7$ *(green) and* α *based on the terrain influence parameter* k *(red).*

8.3 Velocity Deficit at 80 m

Figure 8.5 displays the VD at a distance of 80 m $\approx$ 1 D downstream the WEC plotted against the inflow wind speed u_∞. Individual measurements for each analysis period (triangles, circles and squares for SBL, NBL or CBL respectively) of the VD, as well as the $1\,\mathrm{ms}^{-1}$ binned measurement mean, are shown.
The measured mean VD varies between 30 % and 60 %, having a maximum at a

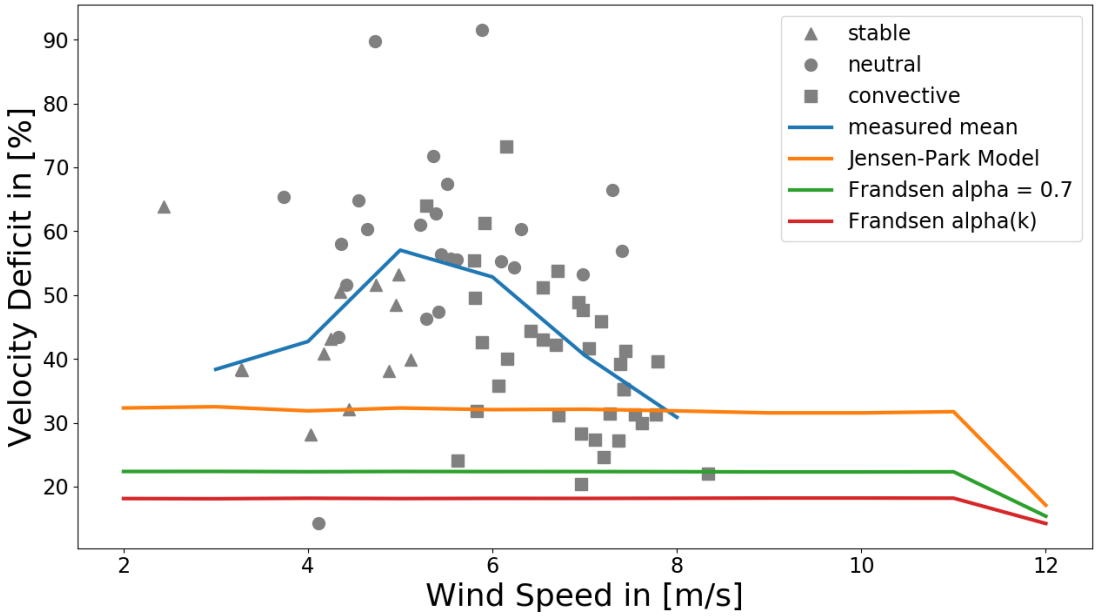

Figure 8.5 – *Velocity deficit* 80 m *behind the WEC plotted against the* $1\,\mathrm{ms}^{-1}$ *binned wind speed of the inflow* u_∞*. Grey symbols denote individual measurements for each wake case. The measurement mean (blue) is compared to the Jensen-Park model (blue) and the Frandsen model with* α *dependent on* k *(red) and* $\alpha = 0.7$ *(green).*

wind speed of $5\,\mathrm{ms}^{-1}$. Unfortunately, wind speeds did not exceed $8\,\mathrm{ms}^{-1}$ during the measurement periods, making it difficult to compare measurement results in a broader spectrum of velocities.

Results coincide with the findings of Aitken et al. (2014), who measured a velocity deficit of 50 % at 1 D behind the WEC for wind speeds smaller than the ones necessary for the WEC to work at rated power. Hirth and Schroeder (2013) found velocity deficits in the range of 40 % one rotor diameter behind the WEC, with wind speeds ranging from $8.5\,\mathrm{ms}^{-1}$ to $11.3\,\mathrm{ms}^{-1}$.

It is interesting to see, that the measured VD varies quite heavily in the range of wind speeds, where the rated power output of the WEC is not yet reached. As the models suggest, the wind speed deficit should be constant up to a wind speed of $12\,\mathrm{ms}^{-1}$, when rated power is produced. For higher velocities the VD will decrease, as the wind carries more energy than can be converted into electricity, meaning that the maximum efficiency to convert kinetic energy into rotational energy is not necessary.

The variation of the VD might have several causes. One cause might be a misalignment between the hub direction and the wind direction, meaning that more wind is passing through the rotor plane than one would expect. This would cause

a VD reduction as less kinetic energy would be extracted from the flow. Another possible explanation for the variations of the VD might be due to the problem to quantify u_∞ correctly. Since the atmosphere exhibits great variability, it is difficult to determine the right velocity for the ABL inflow. The approach to use the inflow velocity 2 D in front of the WEC might not always be the right choice, as eddies with higher or lower velocity might cause deviations from the mean velocity. As a further source of uncertainty, the orography strongly influences the flow 2 D in front of the WEC complicating the definition of an undisturbed inflow velocity even more.

The comparison of the measurements to the models shows that both models clearly tend to underestimate the VD at a distance of 80 m behind the WEC throughout all inflow velocities. The Frandsen model fails to reproduce a realistic VD, with both assumptions proposed for the constant α. Nevertheless, it can be seen that the experimentally determined $\alpha = 0.7$ yields better results than the theoretical estimate when considering the terrain influence parameter k of the Jensen-Park model.

Nevertheless, the Jensen-Park model underestimates the VD for lower wind speeds, only matching the experimental values at $u_\infty = 8\,\mathrm{ms}^{-1}$. The mismatch between models and measurements one rotor diameter behind the WEC is not surprising however, since models are only said to be valid more than 2 D behind the WEC. The distance of 1 D was nevertheless chosen for a first analysis due to the greater amount of wake cases.

But even for distances further downstream the WEC, the models keep underestimating the VD by about 15 percent to 20 % as can be seen in Fig. I.3 (2 D) and Fig. I.4 (3 D).

Chapter 9

Error Estimation for Coplanar Wake Measurements

In this chapter the possible sources for errors that need to be taken into account when measuring the wind field behind a MW WEC in complex terrain with multiple Lidar systems are addressed. There are basically three sources of error: the position of the measurement instruments and their calibration, the radial wind speed accuracy of the individual measurement instruments themselves and the scan geometry.

9.1 Position and Calibration Errors

The exact GPS position of each Lidar system was determined, as already mentioned in Chapt. 5.3, with a Leica MultiStation MS50, with an accuracy greater than 10 cm. Leveling and offset calibration was done using the CNR mapping function of the WindScanner software and verified with a manual level. The systems' pitch and roll angles where monitored throughout the campaign and found to change slightly over time. Deviation from horizontal alignment never exceeded 0.1° for either of the two angles.
The measurement systems' slight movements are caused by the interaction with humans when retrieving data or changes of the instruments' foundation, which is more likely to be the dominant factor. Two of the three systems were positioned directly or indirectly on soil, whereas the third system was positioned on a flat rock shelf. The soil stability is influenced by humidity and precipitation. This can lead to slight movements that can cause changes in the pitch and roll angles of the instruments.

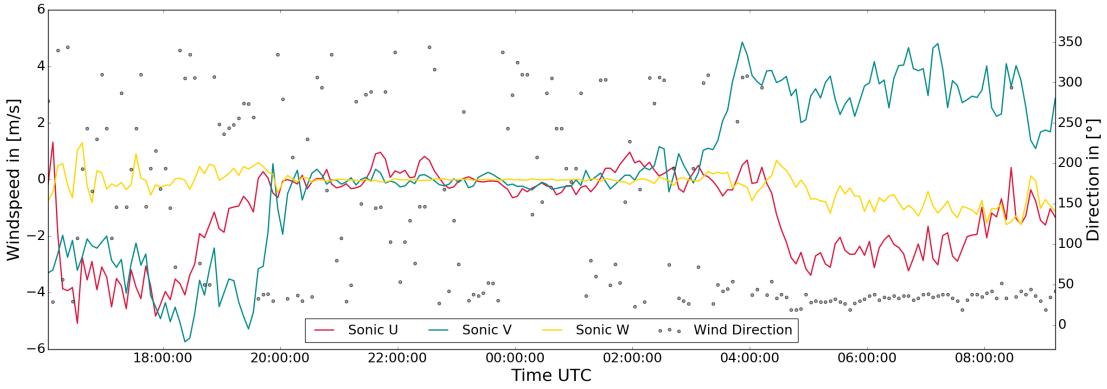

Figure 9.1 – *5 minutes average of wind speed and wind direction measured by Gill WM PRO sonic anemometer on top of the meteorological mast TW25. The three wind components u,v,w are measured in the instruments coordinate system. Wind direction is given in respect to true North.*

To estimate the maximum error caused by the misalignment, the measurement geometry needs to be considered. The deviation Δy of the range gate center in the rotor plane, perpendicular to the CS plane at hub height, can be calculated as $\Delta y = sin(0.1°) \cdot d_{\text{horizontal}} = 2.47\,\text{m}$. The same calculation holds for the deviation of the range gate center in z direction, $\Delta z = sin(0.1°) \cdot d_{\text{max}} = 2.48\,\text{m}$. Nevertheless, Δy and Δz are maximum errors that decrease the closer the measurement is taken to the instrument. In conclusion it can be said that the errors due to position and calibration errors are minor in comparison to the measurement volume of the system itself.

9.2 Instrument Uncertainties

The Windcube 200S is able to measure radial velocities v_{LOS} with an accuracy better than $0.5\,\text{ms}^{-1}$ according to its specifications. However, when calculating the two-dimensional wind vector from two v_{LOS}, the uncertainties for small intersection angles can become very large, even for small v_{LOS} uncertainties. In order to quantify the instrument uncertainties exactly, a comparison between a sonic anemometer of type Gill WM Pro and each Windcube 200S was performed from June, 15th 16:00 UTC to June, 16th 09:00 UTC.
In this period of 17 hours the three Lidar systems performed stare measurements with a range gate center position slightly aloft the highest sonic anemometer mounted on top of the 100 m mast called TW25, located in the valley (see Fig. 5.1). Lidar system settings were chosen so that the physical resolution was 50 m. The

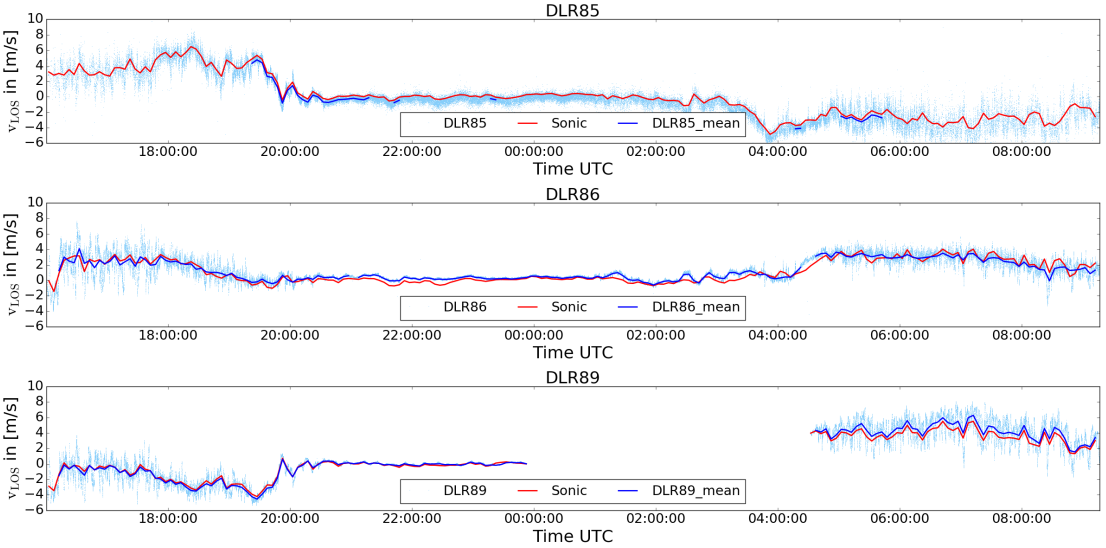

Figure 9.2 – *The graph shows the v_{LOS} measurements of the Lidar systems DLR85, DLR86 and DLR89 (light blue), the 5 minute averages (dark blue) and the wind velocity measured by the Gill WM Pro in LOS direction (red).*

accumulation time was set to 500 ms. The distance between the range gate center and the sonic anemometer for each system was calculated to $d_{\mathrm{DLR85}} = 4.75\,\mathrm{m}$, $d_{\mathrm{DLR86}} = 5.41\,\mathrm{m}$ and $d_{\mathrm{DLR89}} = 5.28\,\mathrm{m}$.

Figure 9.1 shows the five minutes average wind speed for each wind component in the instrument coordinate system, as well as the meteorological wind direction. It can be seen that during the last hours of the 15th of June, wind is blowing from a south-easterly direction, followed by a calm night with veering winds. During morning hours, the wind speed is increasing and shifting towards a north-easterly direction. To compare the sonic anemometer to the LOS velocity measurements of the Lidar system, the sonic coordinate system has to be rotated into LOS direction. This can be done by two consecutive rotations around different axes. The first rotation is around the z-axis, with the angle θ, and the second rotation is around the y-axis, with the angle φ. These rotations can be expressed by the rotational matrices

$$R_z = \begin{pmatrix} cos(\theta) & -sin(\theta) & 0 \\ sin(\theta) & cos(\theta) & 0 \\ 0 & 0 & 1 \end{pmatrix} \text{ and } R_y = \begin{pmatrix} cos(\varphi) & 0 & sin(\varphi) \\ 0 & 1 & 0 \\ -sin(\varphi) & 0 & cos(\varphi) \end{pmatrix}.$$

The LOS velocity v_{LOS} can then be calculated to

$$v_{\mathrm{LOS}} = (R_y R_z \mathbf{v}_{\mathrm{sonic}})\mathbf{n}_x, \tag{9.1}$$

where $\mathbf{v}_{\text{sonic}}$ denotes the three-dimensional sonic wind vector and $\mathbf{n}_x$ is the unit vector in x direction.
As the sonic data is only available in 5 minute averages, it is necessary to calculate the 5 minute averages for the available Windcube 200S data to be able to compare the two measurements. The CNR filter described in Chapt. 6.1 to filter bad data is applied. For further analysis, only five minute intervals with 98 % of good available data (CNR > -27 dB) are selected.
Figure 9.2 shows the Lidar systems measurements together with the 5 minute average as well as the wind velocity in LOS direction measured by the Gill WM Pro. It can be seen that DLR85 and DLR86 were measuring throughout the whole comparison period, whereas DLR89 missed the period between the 15th of June 23:52:36 UTC and the 16th of June at 04:31:45 UTC. This outage of data was caused by a software crash which interrupted the measurement.
Another quite obvious feature is the poor amount of five minute average values for DLR85. It can be seen that a lot of bad data is compromising the five minute means and therefore the 98 % threshold is not surpassed to be included into the analysis. The percentage of good data during the comparison period is only 75 % for DLR85. In comparison, DLR86 and DLR89 do have more than 99.9 % of good data. The bad performance of DLR85 can be traced back to the defect of the acquisition board already mentioned in Chapt. 6.1. This incident is very unfortunate but leaves no other choice than to concentrate on DLR86 and DLR89 for the uncertainty analysis.
DLR86 and DLR89 show good correlation to the measurements from the sonic anemometer throughout the whole measurement period. The mean uncertainties for DLR86 and DLR89 are $\epsilon_{\text{DLR86}} = 0.09\,\text{ms}^{-1}$ and $\epsilon_{\text{DLR89}} = 0.15\,\text{ms}^{-1}$, respectively. Both Lidar instruments measure slightly higher velocities than the sonic anemometer. Nevertheless, the uncertainties are a lot smaller than the $0.5\,\text{ms}^{-1}$ given in the Windcube 200s specifications.
It is assumed that DLR85 exhibits a similar behavior as the two other systems and that uncertainties can be taken to be constant throughout the measurement campaign. The uncertainty that arises due to the measurement geometry can now be estimated.

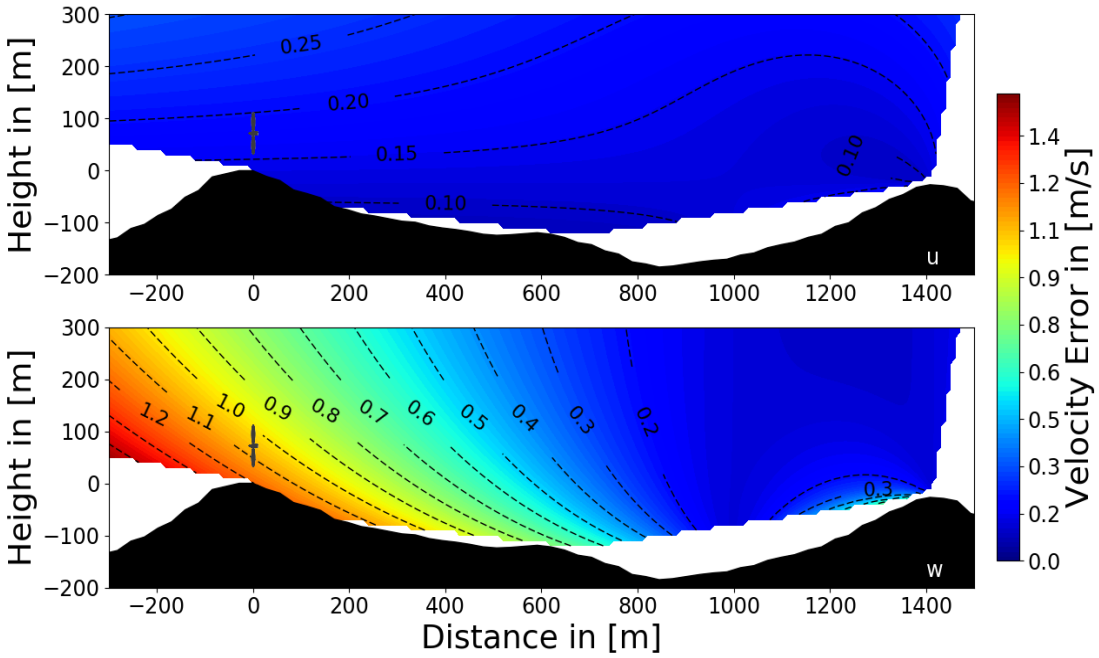

Figure 9.3 – *Uncertainty propagation when calculating the two-dimensional wind vector. The upper graph displays the error in the horizontal component, whereas the lower graph displays the error in the vertical wind component.*

9.3 Geometrical Uncertainty Propagation

To evaluate the influence of the individual measurement uncertainties $\epsilon_{\mathrm{DLR85}}$ and $\epsilon_{\mathrm{DLR86}}$ on the two-dimensional wind vector $\mathbf{u}$, the uncertainties are assumed to be uniform in radial distance and throughout the elevation range, as proposed by Hill et al. (2010).

Equation 9.2 references the general notation to evaluate the error for each velocity component considering uncertainty propagation. Equations 9.3 and 9.4 are the expanded versions of Eq. 9.2 for the two velocity components u and w.

$$\epsilon_{u_i} = [\sum_{j=1}^{N} (\frac{\partial u_i}{\partial r_j})^2 (\epsilon_{r_j})^2]; \tag{9.2}$$

$$\epsilon_u = \left[\left(\frac{sin(\varphi_{\mathrm{DLR85}})}{D} \right)^2 (\epsilon_{\mathrm{DLR86}})^2 + \left(\frac{-sin(\varphi_{\mathrm{DLR86}})}{D} \right)^2 (\epsilon_{\mathrm{DLR85}})^2 \right]^{1/2}; \tag{9.3}$$

$$\epsilon_w = \left[\left(\frac{-cos(\varphi_{\mathrm{DLR85}})}{D} \right)^2 (\epsilon_{\mathrm{DLR86}})^2 + \left(\frac{cos(\varphi_{\mathrm{DLR86}})}{D} \right)^2 (\epsilon_{\mathrm{DLR85}})^2 \right]^{1/2}; \tag{9.4}$$

with $D = cos(\varphi_{\mathrm{DLR85}})sin(\varphi_{\mathrm{DLR86}}) - cos(\varphi_{\mathrm{DLR86}})sin(\varphi_{\mathrm{DLR85}})$. Figure 9.3 displays

ϵ_u and ϵ_w in the CS plane. It can be seen that the uncertainty in the u-component is not greater than $0.25\,\mathrm{ms}^{-1}$. Uncertainties for the w-component strongly depend upon the distance from the Lidar systems. The great uncertainties in the inflow region in front of the WEC that can be as great as $1.2\,\mathrm{ms}^{-1}$, are owed to the small intersection angles between the two Lidar systems.

Chapter 10

Conclusion

The presented work comprises the preparation, description, execution and a first analysis of the Perdigão 2017 field experiment, which was taking place in Perdigão, Portugal in Mai and June 2017. The multinational measurement campaign offered the possibility to investigate the ABL flow in complex terrain over two parallel mountain ridges in conjunction with the interaction with a 2 MW WEC.
The wake structure, produced by the WEC was investigated with three long range pulsed Doppler wind Lidar systems of type Leosphere Windcube 200S. The goal to resolve the two-dimensional wind vector as well as the wake structure in a CS plane was achieved, not least because of the elaborate preparation to discover the influence of the most important scan parameters on the resolution of the wake structure. Sensitivity experiments on a LES turbulent wind field featuring a WEC with a virtual Lidar tool showed that the most sensitive scan parameter to resolve the wake structure is the angular resolution. The range gate separation was found to be of minor influence as long as chosen smaller than the physical resolution. Physical resolution only factored in to resolve velocity extrema, when angular resolution was selected sufficiently large. Scan parameters during the field campaign were chosen in accordance to the findings of the simulations. The angular resolution did not exceed 1° and physical resolution was chosen to be 25 m whenever atmospheric conditions permitted.
From the extensive dataset, three measurement periods with different ABL conditions were chosen for detailed analysis. In all three ABL types, NBL, CBL and SBL, wake structures could be detected for wind directions parallel to the CS plane. The complex, turbulent flow over the ridges imposed difficulties on the wake analysis and a wake tracking algorithm was developed to automatically determine wake parameters by fitting two distinct models to the vertical velocity profiles - a

Gaussian model and double Gaussian model. A complex series of statistic tests and eligibility criteria was elaborated to guarantee precise wake measurements.
It was found that the wake propagation and extension strongly depends upon ABL conditions. For a SBL, wakes could be detected up to 760 m behind the WEC, which corresponds to more than 9.2 D. Most of the wakes in the SBL descended into the valley following the ABL flow, which exhibited a LLJ that undulated over the terrain with a wavelength similar to the distance between the two mountain ridges. Wake structures in the CBL and NBL, on the other hand, were found to propagate smaller distances, only just up to little more than 3.7 D, and to be lifted above hub height.
The mean VD decreases from 48 % at 60 m to 25 % at 250 m and is well within the scope of VD measured in recent field campaigns reported in the state-of-the-art literature. The VD for the three different types of ABL conditions vary in magnitude and rate of decrease with distance from the WEC. The NBL exhibits the most pronounced VD, which decreases the fastest, followed by the VD for the SBL and CBL cases.
A decomposition of the VD for different inflow velocities show that velocity deficits detected one rotor diameter behind the WEC range between 30 % and 60 % and are decreasing in downstream direction. The Jensen-Park, as well as the Frandsen model, to plan wind park layouts, underestimate the velocity deficit along the propagation path for all ABL conditions, with better agreement to measurements for CBL and NBL conditions.
A thorough error analysis showed that errors due to positioning and offset misalignments are small in comparison to the physical resolution of the Leosphere 200S Lidar systems. Uncertainties for each component of the two-dimensional wind vector, caused by the measurement geometry, are small for the horizontal component but grow steadily with distance from the measurement instruments for the vertical wind component. Due to the small intersection angle at the distance of the WEC and in the inflow region, uncertainties for the vertical wind component are too big to draw definite conclusions. Nevertheless, the analysis of the horizontal component yields robust results.
The measurement geometry is one crucial factor that could be improved in future field campaigns in order to achieve intersection angles between two LOS measurements big enough so that the uncertainty for both horizontal and vertical wind components, in the region of interest, is small.
Unfortunate to this study was the fact that no SCADA data was available in order

to consider true turbine hub positions. Such data would be crucial for further investigation to assure correct positioning of the rotor plane in respect to the CS measurement plane.
Once this type of data will be available, the analysis strategy can be optimized by integrating the SCADA data into the process to select time periods where the wake center position is in line with the CS plane and ultimately further effects, like wake meandering, can be evaluated with the help of the third Lidar system, as DLR89 offers the possibility to analyze the lateral wake center deflection in downwind direction.
Also prone to future investigation is a turbulence analysis of the incoming as well as the outgoing ABL flow in order to gain further insight into the loads on WECs placed in complex terrain and a LES simulation of the three presented analysis periods as described by Englberger and Dörnbrack (2017).
It is then hopefully possible to validate the numerical model with the measurement results to finally improve site selection, resilience to mechanical loads and the life time of WECs at exposed locations.

Appendix I

Figures

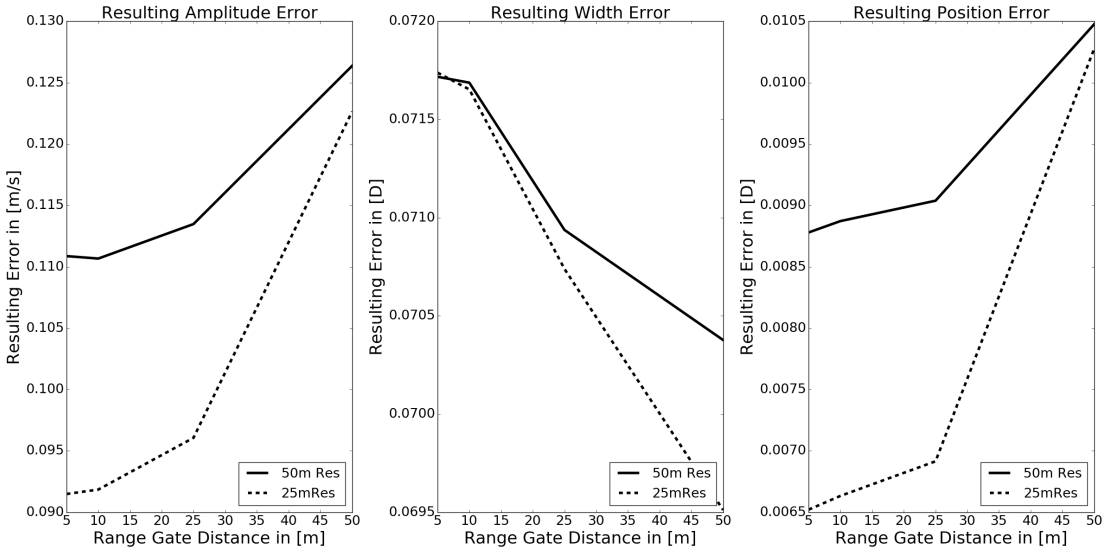

Figure I.1 – *Absolute error plots for the velocity deficit (left), the wake width (middle) and the wake center position (right) in dependence on the range gate spacing for the CS scenario.*

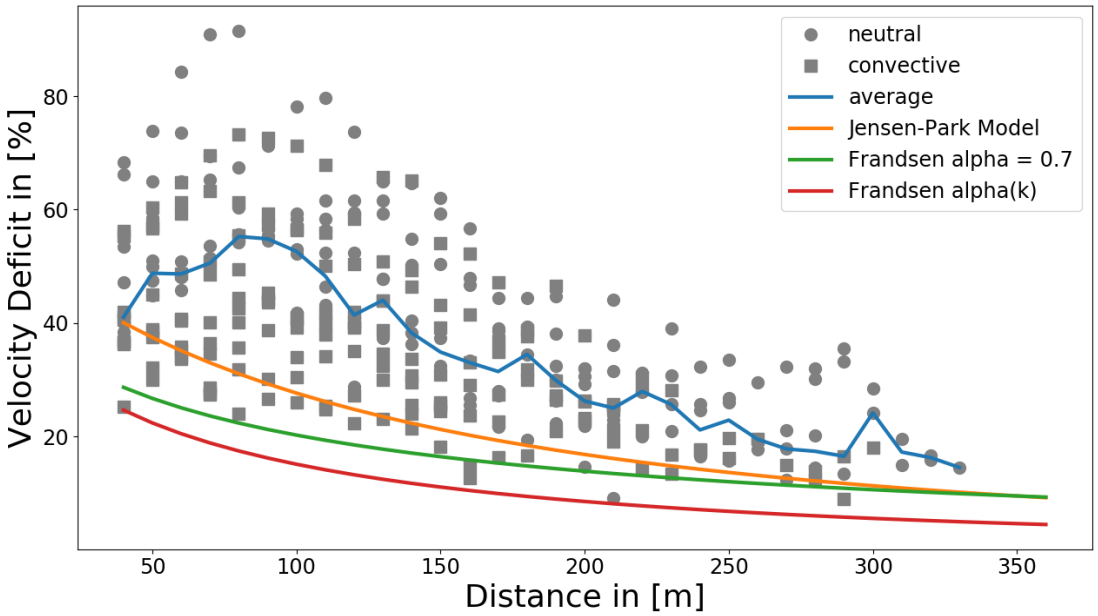

Figure I.2 – *See Fig. 8.4 with the difference that* $u_\infty = 6\,\mathrm{ms}^{-1}$.

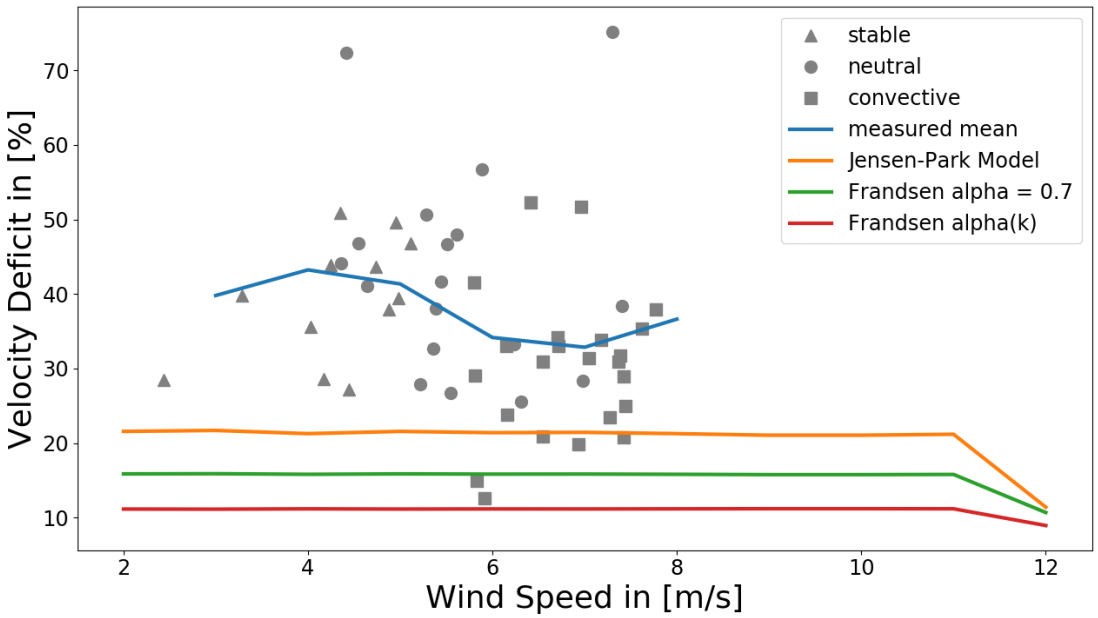

Figure I.3 – *See Fig. 8.5 with the difference that the distance behind the WEC is* 160 m.

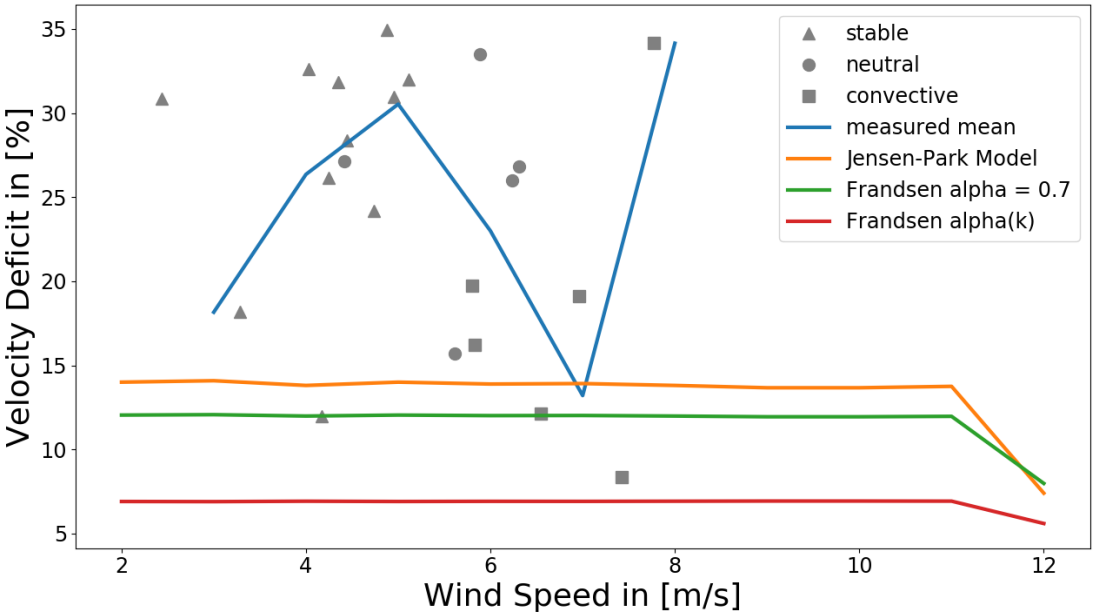

Figure I.4 – *See Fig. 8.5 only that the distance behind the WEC is* 250 m.

Appendix II

Tables

Instrument	Quantity
Met.Mast 10 m	11
Met.Mast 20 m	25
Met.Mast 30 m	9
Met.Mast 60 m	6
Met.Mast 100 m	3
Scanning Lidar	20
Profiling Lidar	7
Water Vapor DIAL	1
Tethersonde	2
SODAR-RASS	2
Radiosonde	2
Profiling Radar-RASS	1
Profiling Radar	1
NMT	4
MWR	3
AERI	1

Table II.1 – *Installed instrumentation at the Perdigão 2017 field experiment.*

Lidar	*Easting* in [m]	*Northing* in [m]	*Height* in [m]
DLR85	34467.772	5214.761	458.151
DLR86	34128.462	4982.504	323.130
DLR89	33127.273	4690.542	480.111
WEC	33285.16	4438.44	484.01

Table II.2 – *Lidar systems' and WEC GPS coordinates in ETRS89/Portugal TM06, EPSG:3763.*

Lidar	Azimuth [°]	STD_θ in [°]	Elevation in [°]	STD_φ in [°]
DLR85	11.2728	0.1607	-0.003	0.0868
DLR86	7.0878	0.1017	0.0784	0.0862
DLR89	-3.0348	0.0447	-0.7066	0.0824

Table II.3 – *Lidar systems' offsets and their standard deviation at the beginning of the Perdigão 2017 field experiment.*

Date	DLR85		DLR86		DLR89		Comment
	Azimuth	Elevation	Azimuth	Elevation	Azimuth	Elevation	
28.04.17	11.2728	-0.003	7.0878	0.0784	-3.0348	-0.7066	initial calibration
17.05.17	11	-0.003	6.89	0.0784	-3.0348	-0.7066	rescan for tower comparison
19.05.17	11	-0.003	7.0878	0.0784	-3.0348	-0.7066	rescan
25.05.17	11.6415	-0.127	7.188	0.05	-2.989	-0.7318	new GPS positions (DTU)
04.06.17	-2.68	-0.15	7.188	0.05	12.8765	-0.522	Lidar switch DLR85 and DLR89
08.06.17	-2.68	-0.15	7.188	0.05	12.967	-0.472	rescan

Table II.4 – *Lidar systems' offsets during the Perdigão 2017 field experiment.*

Bibliography

Ainslie, J. F. (1988). Calculating the flowfield in the wake of wind turbines. *Journal of Wind Engineering and Industrial Aerodynamics*, 27(1-3):213–224.

Aitken, M. L., Banta, R. M., Pichugina, Y. L., and Lundquist, J. K. (2014). Quantifying wind turbine wake characteristics from scanning remote sensor data. *Journal of Atmospheric and Oceanic Technology*, 31(4):765–787.

Arrhenius, S. (1896). Xxxi. on the influence of carbonic acid in the air upon the temperature of the ground. *The London, Edinburgh, and Dublin Philosophical Magazine and Journal of Science*, 41(251):237–276.

Banakh, V. and Smalikho, I. (2013). *Coherent Doppler wind lidars in a turbulent atmosphere*. Artech House.

Banta, R. M., Darby, L. S., Fast, J. D., Pinto, J. O., Whiteman, C. D., Shaw, W. J., and Orr, B. W. (2004). Nocturnal low-level jet in a mountain basin complex. part i: Evolution and effects on local flows. *Journal of Applied Meteorology*, 43(10):1348–1365.

Banta, R. M., Pichugina, Y. L., and Brewer, W. A. (2006). Turbulent velocity-variance profiles in the stable boundary layer generated by a nocturnal low-level jet. *Journal of the Atmospheric Sciences*, 63(11):2700–2719.

Banta, R. M., Pichugina, Y. L., and Newsom, R. K. (2003). Relationship between low-level jet properties and turbulence kinetic energy in the nocturnal stable boundary layer. *Journal of the Atmospheric Sciences*, 60(20):2549–2555.

Barthelmie, R., Folkerts, L., Ormel, F., Sanderhoff, P., Eecen, P., Stobbe, O., and Nielsen, N. (2003). Offshore wind turbine wakes measured by sodar. *Journal of Atmospheric and Oceanic Technology*, 20(4):466–477.

Bingöl, F., Mann, J., and Foussekis, D. (2008). Modeling conically scanning lidar error in complex terrain with wasp engineering. Technical report, Danmarks Tekniske Universitet, Risø Nationallaboratoriet for Bæredygtig Energi.

BMUB (2016). Klimaschutzplan 2050. Available online at https://www.bmub.bund.de (21st November 2017).

BMWi (2017). Erneuerbare energien in zahlen. Available online at http://www.erneuerbare-energien.de (21st November 2017).

Bofinger, S., Callies, D., Scheibe, M., Saint-Drenan, Y.-M., and Rohrig, K. (2011). Studie zum potenzial der windenergienutzung an land-kurzfassung. *Auftrag von Bundesverband Windenergie*.

Bruns, E. and Ohlhorst, D. (2011). Wind power generation in germany–a transdisciplinary view on the innovation biography. *Journal of Transdisciplinary Environmental Studies*, 10(1).

Burton, T., Jenkins, N., Sharpe, D., and Bossanyi, E. (2011). *Wind energy handbook*. John Wiley & Sons.

Chamorro, L. P. and Porté-Agel, F. (2010). Effects of thermal stability and incoming boundary-layer flow characteristics on wind-turbine wakes: a wind-tunnel study. *Boundary-Layer Meteorology*, 136(3):515–533.

Emeis, S. (2010). *Surface-based remote sensing of the atmospheric boundary layer*. Springer Science & Business Media.

Enercon (2017). Enercon e82-e2 specifications. Available online at https://www.enercon.de/en/products/ep-2/e-82/ (21st November 2017).

Englberger, A. and Dörnbrack, A. (2017). Impact of neutral boundary-layer turbulence on wind-turbine wakes: A numerical modelling study. *Boundary-Layer Meteorology*, 162(3):427–449.

Frandsen, S., Barthelmie, R., Pryor, S., Rathmann, O., Larsen, S., Højstrup, J., and Thøgersen, M. (2006). Analytical modelling of wind speed deficit in large offshore wind farms. *Wind Energy*, 9(1-2):39–53.

Frehlich, R., Hannon, S. M., and Henderson, S. W. (1998). Coherent doppler lidar measurements of wind field statistics. *Boundary-Layer Meteorology*, 86(2):233–256.

Guerrero-Lemus, R. and Martínez-Duart, J. M. (2012). *Renewable Energies and CO2: Cost Analysis, Environmental Impacts and Technological Trends-2012 Edition*. Springer Science & Business Media.

Hansen, F. V. (1993). Surface roughness lengths. Technical report, Army Research Laboratory, White Sands Missile Range, New Mexico.

Hill, M., Calhoun, R., Fernando, H., Wieser, A., Dörnbrack, A., Weissmann, M., Mayr, G., and Newsom, R. (2010). Coplanar doppler lidar retrieval of rotors from t-rex. *Journal of the Atmospheric Sciences*, 67(3):713–729.

Hirth, B. D. and Schroeder, J. L. (2013). Documenting wind speed and power deficits behind a utility-scale wind turbine. *Journal of Applied Meteorology and Climatology*, 52(1):39–46.

Hirth, B. D., Schroeder, J. L., Gunter, W. S., and Guynes, J. G. (2012). Measuring a utility-scale turbine wake using the ttuka mobile research radars. *Journal of Atmospheric and Oceanic Technology*, 29(6):765–771.

Högström, U. (1988). Non-dimensional wind and temperature profiles in the atmospheric surface layer: A re-evaluation. *Boundary-Layer Meteorology*, 42(1):55–78.

IEA (2017a). Key world energy statistics 2017. Available online at https://www.iea.org/publications/ (21st November 2017).

IEA (2017b). Renewables inforamtion: Overview 2017. Available online at https://www.iea.org/publications/ (21st November 2017).

IEA (2017c). Tracking clean energy progress 2017. Available online at https://www.iea.org/publications/ (21st November 2017).

Iungo, G. V. and Porté-Agel, F. (2014). Volumetric lidar scanning of wind turbine wakes under convective and neutral atmospheric stability regimes. *Journal of Atmospheric and Oceanic Technology*, 31(10):2035–2048.

Iungo, G. V., Viola, F., Camarri, S., Porté-Agel, F., and Gallaire, F. (2013a). Linear stability analysis of wind turbine wakes performed on wind tunnel measurements. *Journal of Fluid Mechanics*, 737:499–526.

Iungo, G. V., Wu, Y.-T., and Porté-Agel, F. (2013b). Field measurements of wind turbine wakes with lidars. *Journal of Atmospheric and Oceanic Technology*, 30(2):274–287.

Jensen, N. O. (1983). *A note on wind generator interaction.* Risø Library.

Käsler, Y. (2011). *Doppler-Windlidar-Messungen der Umströmung einer Windenergieanlage.* PhD thesis, Universität Oldenburg.

Käsler, Y., Rahm, S., Simmet, R., and Kühn, M. (2010). Wake measurements of a multi-mw wind turbine with coherent long-range pulsed doppler wind lidar. *Journal of Atmospheric and Oceanic Technology*, 27(9):1529–1532.

Kleinbaum, D., Kupper, L., Nizam, A., and Rosenberg, E. (2013). *Applied regression analysis and other multivariable methods.* Nelson Education.

Kumer, V.-M., Reuder, J., Svardal, B., Sætre, C., and Eecen, P. (2015). Characterisation of single wind turbine wakes with static and scanning wintwex-w lidar data. *Energy Procedia*, 80:245–254.

LockheedMartin (2017). Windtracer specifications. Available online at https://www.lockheedmartin.com/us/products/windtracer/windtracer–for-wind-energy.html (21st November 2017).

Lu, X., McElroy, M. B., and Kiviluoma, J. (2009). Global potential for wind-generated electricity. *Proceedings of the National Academy of Sciences*, 106(27):10933–10938.

Mann, J., Angelou, N., Arnqvist, J., Callies, D., Cantero, E., Arroyo, R. C., Courtney, M., Cuxart, J., Dellwik, E., Gottschall, J., et al. (2017). Complex terrain experiments in the new european wind atlas. *Phil. Trans. R. Soc. A*, 375(2091):20160101.

Mann, J., Palma, J., Matos, J., Angelou, N., Courtney, M., Lea, G., and Vasiljevic, N. (2016). Experimental investigation of flow over a double ridge with several doppler lidar systems. In *Experimental investigation of flow over a double ridge with several Doppler lidar systems*, http://ams.confex.com/ams/96Annual/webprogram/Paper284781.html. 96th American Meteorological Society Annual Meeting.

Molly, J.-P. (1978). *Windenergie in Theorie und Praxis: Grundlagen und Einsatz.* Müller.

NCAR/EOL (2017). *NCAR/EOL Preliminary 5 minute ISFS data, instrument coordinates, not tilt corrected. Version 0.1 [PRELIMINARY].* NCAR/EOL - Earth

Observing Laboratory, https://data.eol.ucar.edu/dataset/536.001 (November 21st 2017).

Pachauri, R. K., Allen, M. R., Barros, V. R., Broome, J., Cramer, W., Christ, R., Church, J. A., Clarke, L., Dahe, Q., Dasgupta, P., et al. (2014). *Climate change 2014: synthesis report. Contribution of Working Groups I, II and III to the fifth assessment report of the Intergovernmental Panel on Climate Change*. IPCC.

Päschke, E., Leinweber, R., and Lehmann, V. (2015). An assessment of the performance of a 1.5 μm doppler lidar for operational vertical wind profiling based on a 1-year trial. *Atmospheric Measurement Techniques*, 8(6):2251.

Paulson, C. A. (1970). The mathematical representation of wind speed and temperature profiles in the unstable atmospheric surface layer. *Journal of Applied Meteorology*, 9(6):857–861.

Politis, E. S., Prospathopoulos, J., Cabezon, D., Hansen, K. S., Chaviaropoulos, P., and Barthelmie, R. J. (2012). Modeling wake effects in large wind farms in complex terrain: the problem, the methods and the issues. *Wind Energy*, 15(1):161–182.

Renkema, D. J. (2007). Validation of wind turbine wake models. Master's thesis, Delft University of Technology.

Rhodes, M. E. and Lundquist, J. K. (2013). The effect of wind-turbine wakes on summertime us midwest atmospheric wind profiles as observed with ground-based doppler lidar. *Boundary-Layer Meteorology*, 149(1):85–103.

Rodrigues, C. V., Palma, J., Vasiljević, N., Courtney, M., and Mann, J. (2016). Coupled simulations and comparison with multi-lidar measurements of the wind flow over a double-ridge. In *Journal of Physics: Conference Series*, volume 753, page 032025. IOP Publishing.

Santos, F. D. (2011). *Humans on earth: from origins to possible futures*. Springer Science & Business Media.

Schröttle, J., Piotrowski, Z., Gerz, T., Englberger, A., and Dörnbrack, A. (2016). Wind turbine wakes in forest and neutral plane wall boundary layer large-eddy simulations. In *Journal of Physics: Conference Series*, volume 753, page 032058.

Smalikho, I., Banakh, V., Pichugina, Y., Brewer, W., Banta, R., Lundquist, J., and Kelley, N. (2013). Lidar investigation of atmosphere effect on a wind turbine wake. *Journal of Atmospheric and Oceanic Technology*, 30(11):2554–2570.

Stawiarski, C. (2014). *Optimizing dual-Doppler lidar measurements of surface layer coherent structures with large-eddy simulations*. KIT Scientific Publishing.

Stull, R. B. (2012). *An introduction to boundary layer meteorology*. Springer Science & Business Media.

Tampieri, F. (2017). *Turbulence and Dispersion in the Planetary Boundary Layer*. Springer.

Taylor, G. I. (1938). The spectrum of turbulence. *Proc. R. Soc.*, A164:476–490.

Troldborg, N., Sørensen, J. N., and Mikkelsen, R. (2007). Actuator line simulation of wake of wind turbine operating in turbulent inflow. In *Journal of physics: conference series*, volume 75, page 012063. IOP Publishing.

Trujillo, J.-J., Bingöl, F., Larsen, G. C., Mann, J., and Kühn, M. (2011). Light detection and ranging measurements of wake dynamics. part ii: two-dimensional scanning. *Wind Energy*, 14(1):61–75.

UNFCCC (2016). Paris agreement.

van Kuik, G., Peinke, J., Nijssen, R., Lekou, D., Mann, J., Sørensen, J. N., Ferreira, C., van Wingerden, J., Schlipf, D., Gebraad, P., et al. (2016). Long-term research challenges in wind energy–a research agenda by the european academy of wind energy. *Wind Energy Science*, 1:1–39.

Vasiljević, N., Lea, G., Courtney, M., Cariou, J.-P., Mann, J., and Mikkelsen, T. (2016). Long-range windscanner system. *Remote Sensing*, 8(11):896.

Vermeer, L., Sørensen, J. N., and Crespo, A. (2003). Wind turbine wake aerodynamics. *Progress in aerospace sciences*, 39(6):467–510.

Weitkamp, C. (2006). *Lidar: range-resolved optical remote sensing of the atmosphere*. Springer Science & Business.

Wu, Y.-T. and Porté-Agel, F. (2012). Atmospheric turbulence effects on wind-turbine wakes: An les study. *Energies*, 5(12):5340–5362.

Zhang, W., Markfort, C. D., and Porté-Agel, F. (2012). Near-wake flow structure downwind of a wind turbine in a turbulent boundary layer. *Experiments in fluids*, 52(5):1219–1235.

Erklärung:

Hiermit erkläre ich, die vorliegende Arbeit selbständig verfasst zu haben und keine anderen als die in der Arbeit angegebenen Quellen und Hilfsmittel benutzt zu haben.

München, 11.12.2017

Unterschrift